OUKA
The University of Osaka
Institutional Knowledge Archive

Title	Shocks and Particle Energization in Supermassive Black Hole Coronae
Author(s)	Ly Nhat, Minh
Citation	大阪大学, 2026, 博士論文
Version Type	VoR
URL	https://doi.org/10.18910/105642
rights	
Note	

The University of Osaka Institutional Knowledge Archive : OUKA

https://ir.library.osaka-u.ac.jp/

The University of Osaka

Shocks and Particle Energization in Supermassive Black Hole Coronae

Ly Nhat Minh

A dissertation submitted in partial fulfillment
of the requirements for the degree of Doctor of Philosophy

Department of Physics
Graduate school of Science
The University of Osaka

February 4, 2026

Abstract

The recent identification of the Seyfert galaxy NGC 1068 as a source of high-energy neutrinos by the IceCube Neutrino Observatory presents a major challenge to standard high-energy astrophysical models. The detected neutrino flux, unaccompanied by a comparable flux of TeV gamma-rays, points to a particle acceleration environment that is transparent to neutrinos but opaque to gamma-rays: likely the hot coronal region surrounding the supermassive black hole (BH). However, the dominant particle acceleration mechanism in such high-density, high-temperature environments remains unestablished. Diffusive Shock Acceleration (DSA) has emerged as a leading candidate, particularly given recent observations indicating weak coronal magnetic fields (high plasma β) where magnetic reconnection is likely inefficient.

This thesis investigates the microphysics of collisionless shocks and particle energization through a comprehensive suite of first-principles, one-dimensional Particle-in-Cell (PIC) simulations. The study is structured to bridge fundamental plasma kinetics with specific astrophysical applications.

First, we establish a unified framework for collisionless dissipation in the unmagnetized electrostatic limit or electrostatic shocks. By analyzing the collisionless Riemann problem, we map the dynamical transition from shocks formation regime in plasmas to the vacuum expansion regime. We identify that electrostatic double-Layer structures emerge as the critical intermediate regime connecting these two distinct behaviors. This analysis defines the baseline potential structures governing ion dynamics before the introduction of magnetic complexity.

Second, we extend this kinetic analysis to the magnetized regime relevant to BH coronae. We aim to resolve the critical uncertainty regarding the viability of DSA: specifically, whether shocks can accelerate protons to ~ 100 TeV with $\sim 10\%$ efficiency under realistic coronal conditions. To address the poorly understood regimes of low sonic Mach number (M_s) and non-equilibrium temperatures ($T_i \neq T_e$), we systematically survey the parameter space of M_s, Alfvénic Mach number (M_A), shock velocity, and the temperature ratio T_i/T_e.

We demonstrate that quasi-parallel collisionless shocks are robust proton accelerators. We find that DSA consistently converts approximately 10% of the shock wave's kinetic energy into non-thermal ions. This holds true even in the low-Mach-number regime ($M_s \approx 2$), which was traditionally considered inefficient. Furthermore, we verify that the

acceleration rates are sufficient to reach the requisite ~ 100 TeV energies, providing the necessary reservoir for hadronic neutrino production.

Additionally, we characterize the self-generated magnetic turbulence driven by non-resonant (Bell) and resonant streaming instabilities. Crucially, we link strong magnetic amplification to the suppression of primary electron acceleration. In regimes of high amplification, the shock front becomes locally superluminal, trapping thermal electrons and inhibiting their injection into the DSA cycle. We also observe that a lower initial electron temperature ($T_e \ll T_i$), typical of coronal plasmas, appears to result in lower electron acceleration efficiency. However, the electron dynamics have yet to achieve a true steady-state in such cases due to computational limitations. It remains unclear whether this suppression persists in the long-term steady state or represents a transient phase of shock evolution.

Finally, we discuss the multi-messenger implications of these micro-physical constraints, examining the potential for neutrino production in BH coronae and the consequences of shock acceleration for the radiative spectra of leptons.

Acknowledgements

This dissertation has not come easy. There were many moments when I thought I would not make it. For both myself and my research, I owe my gratitude to many people, more than I can fully express here. To everyone who supported me along this journey, thank you for your advice, love, and encouragement.

I have been fortunate to work with amazing professors and advisors. To Takayoshi Sano, for guiding me closely throughout my research and academic career, I do not have words strong enough to express how grateful I am. Thank you for shaping me into a "Doctor" and into the researcher I am today. Thank you for your patience, your steady support, and for always encouraging me to pursue research driven by my curiosity.

To Yasuhiko Sentoku, thank you for accepting me into the group and leading me into the wonderful world of plasma and computational physics. Thank you for encouraging me, for taking the time to go running with me, and for patiently listening to and advising my research, even when I chose a doctoral theme different from the main direction of the group.

To Yoshiyuki Inoue, my "astrophysics" advisor, if I had not attended your class that day, this thesis might never have materialized. Thank you for opening the path for me into the world of high-energy astrophysics and for guiding me through it with patience.

To the other members of my dissertation committee, Professor Shinsuke Fujioka and Professor Kenichi Asano, thank you for your thoughtful questions and valuable advice, which greatly helped improve this work.

I would not have had the courage to finish this thesis without my friends, too many to list by name. Thank you for helping me through difficult times, for listening to my thoughts, and for sharing both joy and sadness with me.

To my friends in Japan, thank you for making my time here truly come to life. Thank you for adding color to my daily routine and for exploring so many amazing places with me.

To my loved ones, thank you for everything you have done for me unconditionally. I love you all, and I owe you more than I can ever say.

And to myself, if things become difficult again, and they will, remember where you came from and how far you have already come.

Contents

Abstract i

Acknowledgements iii

List of Figures vi

List of Tables xiv

1 Introduction 1

1.1 Shocks in collisionless plasmas . . . 1

1.1.1 Overview of collisionless shocks . . . 1

1.1.2 Laser-driven collisionless shock in laboratory . . . 2

1.1.3 Collisionless shocks in astrophysical context . . . 3

1.1.4 Numerical method to study collisionless shocks . . . 5

1.2 Proton acceleration in the vicinity of supermassive black holes: high-energy neutrino signals . . . 5

1.2.1 Observational motivation . . . 5

1.2.2 Black hole coronae . . . 6

1.2.3 Acceleration mechanism of protons . . . 7

1.2.4 Why diffusive shock acceleration? . . . 8

1.3 Plan and structure of this thesis . . . 9

2 Fundamental Properties of Collisionless Shocks: On Collisionless Electrostatic Shock Formation 10

2.1 Introduction . . . 10

2.2 Particle-in-cell simulation . . . 12

2.2.1 Numerical methods . . . 12

2.2.2 Numerical setup . . . 14

2.2.3 The transition of shock structures . . . 15

2.3 Analytical model for steady-state of electrostatic shocks . . . 18

2.3.1 The conventional model for the critical Mach number . . . 18

2.3.2 The density ratios after the isothermal expansion . . . 19

2.3.3 Prediction of the transition from collisionless shock to double-layer structures . . . 22
2.3.4 Prediction of the Mach numbers . . . 23
2.4 Discussion . . . 25
2.5 Summary . . . 26

3 Shocks in Black Hole Coronae: Shock Structure and Proton Acceleration 28
3.1 Introduction . . . 28
3.2 Shock conditions in BH coronae . . . 30
3.3 Numerical setup . . . 32
3.4 Fiducial run: shock characteristics and particle acceleration . . . 34
3.4.1 Shock structure . . . 34
3.4.2 Particle spectrum and acceleration trajectory . . . 36
3.4.3 Streaming instabilities . . . 38
3.5 Proton acceleration rate . . . 40
3.5.1 Dependence on T_i/T_e and M_s . . . 41
3.5.2 Dependence on M_A and $v_{\rm pt}$ . . . 41
3.5.3 Scaling of acceleration rate . . . 43
3.6 Energy partition . . . 45

4 Magnetic field and Electron dynamics 47
4.1 Introduction . . . 47
4.2 Magnetic field amplification . . . 47
4.2.1 Resonant and Non-resonant modes . . . 47
4.2.2 Magnetic field profile . . . 50
4.2.2.1 Dependence on M_A and $v_{\rm pt}$ . . . 50
4.2.2.2 Dependence on M_s and T_i/T_e . . . 52
4.2.3 Magnetic field amplification . . . 54
4.3 Electron dynamics . . . 56
4.3.1 Electron acceleration suppression by strong magnetic field amplification . . . 56
4.3.1.1 Critical field assesment . . . 57
4.3.1.2 Consequences of suppression by strong magnetic field amplification . . . 58
4.3.2 Electron acceleration with different Ti/Te . . . 60
4.3.3 Partition into thermal electron . . . 62

5 Implications for neutrino emission from NGC 1068 **65**
5.1 Introduction 65
5.2 Timescales 65
5.3 Energy budget 69

6 Conclusion **71**
6.1 Summary of the Thesis 71
6.1.1 On collisionless electrostatic shocks 71
6.1.2 Proton acceleration 72
6.1.3 Multi-messenger implications for NGC 1068 73
6.2 Limitations and Future Work 73

List of Figures

1.1 Schematic view of the Earth's bow shock, the first confirmed collisionless shock detected in nature. The shock forms as the super-Alfvénic solar wind encounters the obstacle of Earth's magnetosphere. Depending on the angle θ_{Bn} between the shock normal and the upstream magnetic field, the shock is classified as quasi-perpendicular ($\theta_{Bn} > 45°$) or quasi-parallel ($\theta_{Bn} < 45°$), exhibiting distinct particle acceleration properties (Balogh & Treumann, 2013a). 2

1.2 Schematic of the setup (a) and phase space results (b) of laser-driven collisionless shock acceleration (CSA) scheme proposed by Fiuza Fiuza et al. (2012, 2013). The reflected ions, gaining twice the shock velocity, demonstrate the efficiency of this scheme for compact ion acceleration. 3

1.3 Ion acceleration efficiency ε (defined as a percentage of solar wind energy) plotted against the shock obliquity angle θ_{Bn}. The color scale indicates the Alfvén Mach number M_A. The vertical dashed line at 45° marks the transition between quasi-parallel and quasi-perpendicular geometries. Note the sharp suppression of ion acceleration in the quasi-perpendicular regime. Adapted from Johlander et al. (2021). 4

1.4 Multi-messenger motivation for a "hidden" neutrino source from NGC 1068. Neutrino spectrum (purple band) is an order of magnitude above the γ-ray from Fermi's data. Here, two proton acceleration mechanisms by diffusive shock acceleration (DSA) and stochastic acceleration (SA) were shown to compare with observational results. Adapt from IceCube Collaboration*† et al. (2022). 6

1.5 Schematic of possible coronal geometries in disk–corona system around an SMBH. Thethermaldiskemission(red)is up-scattered by hot electrons in the corona. The resulting high-energy photons (blue) reflect off the disk, which then emits "reprocessed" light(green). Adapt from Bambi et al. (2021). . 7

2.1 Summary of the PIC scheme for a self-consistent description of the evolution of the plasma system. 13

2.2 (a) The initial setup of PIC simulations is illustrated. Two slabs of plasma with the density ratio Γ and temperature ratio Θ are presented in different shades. (b) A typical ion density profile at the shock's steady-state indicates density reduction near the shock front due to the expansion of the high density slab. The electrostatic potential ϕ created by the interactions of two slabs at the front is depicted in the inset. The shock upstream region (low density) and the downstream region are denoted by (0) and (1), respectively. 14
2.3 Ion density profiles and phase space structures from simulations at $t = 3500$ ω_{pe}^{-1} with $\Theta = 1$ ($T_{eH} = 10$ keV), $\Gamma = 20$ for (a) and (b), $\Gamma = 100$ for (d) and (e). Ions from the high density slab are represented as purple in (b) and (e), while those from the low density slab are marked as green. (c) and (f) are p_x-x diagrams the same as (b) and (e), but only show particles originating from the higher density region. 15
2.4 Comparison between v_p (blue circles) and v_s (red circle) from the simulations (in laboratory frame) for varying $\Gamma = 4 - 100$ with $\Theta = 1$ (a) and $\Theta = 20$ (b). The data is illustrated in two scales. The left label is normalized by the sound speed of the upstream plasma c_{s0}, which varies with Γ. The right label is normalized by the speed of light c which are common scale for both panels. In (a), the blue solid line shows v_p from Eq. (2.8) Allen & Andrews (1970); Perego et al. (2013) and v_s (black solid line) is calculated from the semi-analytical model discussing in Eq. (2.12). It can be seen that the transition occurs around $\Gamma = 40$ in both cases. . . 17
2.5 Ion phase space in the moving shock frame for double-layer (a) and collisionless electrostatic shock (b) according to Ref. Hershkowitz (1981). In Sec. 2.3. D, the density of the accelerated ions n_α or ions moving outward from the front, and the accelerated fraction $\alpha = n_\alpha/n_L$ are explained in detail. For electrostatic shocks, n_α is primarily the density of reflected ions while for double-layer structures it also includes the transmitted fraction originating from the high density plasma. 20
2.6 The conventional critical Mach number (black dashed line) is obtained from solving Eq. (2.6) with varying Γ and $\Theta = 1$. The new critical Mach numbers (black solid line) are calculated using $\Gamma' = n_p/n_L$ calculated from Eqs. (2.7) and (2.8). Simulation results of the shock Mach number M_s with corresponding Γ ($\Theta = 1$) are shown by red dots. M_s from the simulations exceeds the conventional upper limit but is less than the new model's limit. 20

2.7 The density ratios at the expansion front Γ' (black solid line) with respect to the initial values calculated by Eqs. (2.7) and (2.8) in comparison with simulation results (red crosses). The bars represent the error evaluated from the density fluctuations in the simulations. 21
2.8 The transition condition predicted by Eq. (2.11) is $\Gamma \sim 40$, which indicated from the crossing point of $M_{\rm cr}$ (black solid line) and $M_s = \sqrt{\Gamma' - 2)/2}$ (blue solid line). $M_{\rm cr}$ is obtained from our new model, and Γ' relation with Γ is given by the black solid line in Fig. 2.7. 22
2.9 accelerated fraction $\alpha = n_a/n_L$ obtained from the simulations with respective Γ and $\Theta = 1$. We derive α from tracking the reflection rate for collisionless shock cases (blue crosses), while α for double-layer (blue dots) is obtained by the outflow density n_α [see Fig. 2.5(a)]. Black dot line is the extension of collisionless shocks' accelerated fraction which is used with Eq. (2.12) to derive v_s in Fig. 2.4(a). The reflection rate is denoted by the red dot line. 23
2.10 Shock Mach numbers (blue circles) and accelerated fraction α (red crosses) when adding initial velocity v_{init} for the case of $\Gamma = 8$, $\Theta = 1$ and $T_e = 10$ keV. The critical Mach number (black dashed line) is approximately 1.92 in this case. We can see that when M_s reach the critical value, $\alpha \approx 1$ as predicted from the critical condition $\varphi = M_{cr}^2/2$ and the definition of α. Shock structures start to saturate with $v_{init} > 2.5\ c_s$. At $v_{init} = 3.5\ c_s$, we have $\alpha \approx 6.3$ and it is no longer a collisionless shock structure. 25
2.11 Comparison of the shock velocity between collisionless shock (red crosses) and collisional shock Mach numbers (black solid line) calculated from Eq. (2.12) with $\alpha = 0$ (no reflection). As a reference, v_p is also shown by the blue solid line. It is clear that, unlike collisionless shocks, v_s is always greater than v_p for collisional shocks, implying that there is no transition to double-layer structures. 26

3.1 Schematic illustration of an accretion shock formed by the infalling flow in the hot BH corona. Protons are accelerated to high energies and produce high-energy neutrinos through hadronic pp and $p\gamma$ interactions. Neutrinos can escape from the system and be observed by IceCube, while the accompanying gamma-rays will be attenuated by X-ray photons. 30

3.2 Snapshot of shock structures in the fiducial model (run T10) at $t \approx 256\ \Omega_{\rm ci}^{-1}$. (a, b) The position-momentum ($x - p_x$) phase space distributions for ions and electrons. (c) Ion density profile, with the shock position ($x_{\rm sh}$) marked by the red dashed line. (d, e) The transverse magnetic field components (B_y, B_z) and the total transverse amplitude ($B_\perp$), showing significant amplification over the initial value [black dashed line in (e)]. . 35
3.3 Signatures of particle acceleration, with the color scale indicating time in units of $t\Omega_{\rm ci}$. (a) Evolution of the ion and electron energy spectra in the shock downstream. Both species exhibit two distinct components: a thermal bulk and a developing non-thermal power-law tail. (b, c) Trajectories of a typical accelerating electron and ion, illustrating the DSA process. . 37
3.4 Spatial Fourier analysis of the upstream streaming instability at $t \approx 130\ \Omega_{\rm ci}^{-1}$, showing that the dominant mode is the right-hand non-resonant instability. (a) Transverse magnetic field profile in the upstream region selected for the spectral analysis, indicated by the two vertical black dashed lines. (b) Fourier power spectrum of the magnetic field, decomposed into right-hand (RH) and left-hand (LH) polarized modes. The vertical black dashed line marks the wavenumber of the mode resonant with back-streaming ions of mean gyroradius $\bar{\rho}_i$, $k_{\rm res} \sim 1/\bar{\rho}_i$. 39
3.5 Time evolution of the mean Lorentz factor $\gamma(t)$ of the ten most energetic ions at each snapshot for different plasma conditions. The upper panels show the effect of varying the temperature ratio T_i/T_e at fixed M_s, while the lower panels show the effect of varying M_s at fixed T_i/T_e. Shaded regions represent one standard deviation. All other parameters are identical to the reference run (T10), unless otherwise noted. (a–b) Dependence on T_i/T_e for $M_s = 8$ and $M_s = 4$, respectively. (c) Dependence on M_s for $T_i/T_e = 1$. (d) Same as (c), but for both $T_i/T_e = 0.01$ (red lines) and $T_i/T_e = 10$ (blue lines). 40
3.6 Same format as Figure 3.5, but showing the dependence on the Alfvénic Mach number and the injected particle velocity. (a) Time evolution of the mean Lorentz factor of the ten most energetic ions for different M_A. (b) Normalized energy gain, $(\gamma - \gamma_{\rm sh})\beta_{\rm sh}^{-2}$, for different injected velocities $v_{\rm pt}/c$. Shaded regions indicate one standard deviation. All other parameters are identical to the reference run (T10), unless otherwise specified. 42
3.7 The normalized acceleration coefficient $d(\gamma/\beta_{\rm sh}^2)/d(t\Omega_{\rm ci})$ (i.e., the slope in Figures 3.5 and 3.6), as a function of key shock parameters, calculated from the linear slope of the energy gain at late times. (a) Dependence on T_i/T_e. (b) and (c) Dependence on M_s and M_A, respectively. (d) Dependence on $v_{\rm pt}/c$. 43

3.8 Fraction of non-thermal ion (solid lines) and electron (dashed lines) energy to total energy in the particle spectra across the parameter space. Non-thermal ions are efficiently accelerated, receiving $\sim 10\%$ of the total energy, while electrons remain much less efficient ($< 1\%$) or even suppressed in cases indicated by the $\star$ symbol. Left panels: the effect of T_i/T_e ratio with fixed $M_s = 2$ (red lines) and $M_s = 4$ (blue lines) in panel (a), and $M_s = 8$ in panel (d). Middle panels: the scaling with M_s when T_i/T_e is fixed at $T_i/T_e = 1$ in panel (b), and $T_i/T_e = 0.01$ (red) and $T_i/T_e = 10$ in panel (e). Right panels: variation with (c) M_A and (f) $v_{\rm pt}/c$. Unless explicitly stated otherwise, other parameters follow $T_i/T_e = 10$, $M_s = 8$, $M_A = 26$, and $v_{\rm pt}/c = 0.25$. 44

4.1 Time evolution of the spatial Fourier spectra for the NRI and RI regimes, represented by simulations T10 (left panels, $M_A = 26$) and A4 (right panels, $M_A = 8$). The spectra are calculated from the upstream magnetic field within the fixed range $500\ d_e \leq x - x_{\rm sh} \leq 10500\ d_e$. Power is decomposed into LH (orange) and RH (blue) modes to illustrate polarization. The vertical black dashed line indicates the wavenumber resonant with the mean gyroradius of back-streaming ions (Equation 4.3), while the vertical red dashed line marks the theoretical fastest-growing non-resonant mode (Equation 4.2). Panels (a1)–(a3) and (b1)–(b3) display snapshots at consecutive times for the T10 and A4 runs, respectively, showing the dominance of RH (Bell) modes in T10 and LH (Resonant) modes in A4. 48

4.2 Time-averaged spatial profiles of the transverse magnetic field $B_\perp = \sqrt{B_y^2 + B_z^2}$. The profiles are averaged over a duration of 100 $\Omega_{\rm ci}^{-1}$, and the horizontal black dashed line indicates the initial transverse field strength ($B_0 \sin 30^\circ$). Unless otherwise stated, shock parameters correspond to the reference run T10: $M_A = 26$, $M_s = 8$, $v_{\rm pt}/c = 0.25$ (yielding $v_{\rm sh}/c \approx 0.33$), and $T_i/T_e = 10$. (a1) Cases with varying Alfvénic Mach number M_A. (b1) Profiles for simulations with varying initial drift speed $v_{\rm pt}/c$. Panels (a2) and (b2) display zoomed-in views of the near-shock region for (a1) and (b1), respectively. 51

4.3 Time-averaged spatial profiles of the transverse magnetic field ($B_\perp = \sqrt{B_y^2 + B_z^2}$), formatted similarly to Figure 4.2. The profiles are averaged over a duration of $\Delta t = 100\ \Omega_{\rm ci}^{-1}$ (see text for details); the horizontal black dashed line indicates the initial transverse field strength ($B_0 \sin 30°$). Panels are organized to isolate thermodynamic effects: (a1)–(a3) show variations in T_i/T_e at fixed M_s, while (b1)–(b3) show variations in M_s at fixed T_i/T_e. Unless otherwise stated, shock parameters correspond to the reference run T10: $M_A = 26$, $M_s = 8$, $v_{\rm pt}/c = 0.25$, and $T_i/T_e = 10$. Insets display zoomed-in views of the shock transition. 53

4.4 Dependence of the saturation total magnetic field amplification $(B_{\rm sat}/B_0)^2$ on M_s, M_A, $v_{\rm pt}/c$, and T_i/T_e. The field values are averaged spatially over $x_{\rm sh} < x < 3M_A d_i$ (corresponding to three typical ion gyroradii) and temporally over $\Delta t = 50\ \Omega_{\rm ci}^{-1}$. Circles connected by dashed lines represent simulation data. Solid lines of the corresponding color indicate best fits in Equation 4.5, with shaded regions denoting the uncertainty of the fitted parameters. (a) Dependence on T_i/T_e; each line represents a fixed sonic Mach number $M_s = 2, 4$, or 8. (b) Dependence on M_s for various temperature ratios T_i/T_e ranging from 1 to 50. Panels (c) and (d) display the scaling with $v_{\rm pt}/c$ and M_A, respectively. Unless otherwise stated, shock parameters correspond to the reference run T10: $M_A = 26$, $M_s = 8$, $v_{\rm pt}/c = 0.25$, and $T_i/T_e = 10$. 55

4.5 Time evolution of the mean Lorentz factor $\gamma_e(t)$ of the ten most energetic electrons for runs S4T1 ($M_s = 4$) and S20T1 ($M_s = 20$). Common parameters are $M_A = 26$, $T_i/T_e = 1$, and $v_{\rm pt}/c = 0.25$. Shaded regions indicate the standard deviation. In the $M_s = 4$ case, the electron energy increases steadily over time, indicative of the DSA process. In contrast, for the $M_s = 20$ case, although electrons quickly reach $\gamma_e \sim 100$ via preacceleration, their acceleration subsequently stalls. This corresponds to the much stronger magnetic field amplification observed in the $M_s = 20$ case [see Figure 4.3(b2)]. 57

4.6 Dependence of electron acceleration metrics on the magnetic field amplification level, specifically the ratio of the saturation field to the critical superluminal field ($B_{\rm sat}/B_{\rm crit}$). The vertical dashed line at $B_{\rm sat}/B_{\rm crit} = 1$ marks the transition threshold: configurations with $B_{\rm sat} < B_{\rm crit}$ (blue circles) remain locally subluminal, while those with $B_{\rm sat} > B_{\rm crit}$ (red stars) become locally superluminal. (a) Normalized rate of increase of the maximum electron energy, $\dot{E}_{\rm max,e} \equiv dE_{\rm max,e}/dt$, in units of $m_i v_{\rm sh}^2 \Omega_{ci}$ (note the $\times 10^{-2}$ scale). (b) Non-thermal electron acceleration efficiency, $E_e^{\rm nt}/E_{\rm tot}$ (defined in Chapter 3; $\times 10^{-2}$ scale). Both quantities decrease sharply for $B_{\rm sat}/B_{\rm crit} \gtrsim 1$, demonstrating the suppression of electron injection in the locally superluminal regime. 59

4.7 Downstream electron and ion spectra, $(\gamma-1)f(\gamma)$, and their time evolution [similar to Figure 3.3(a)], for simulations with fixed $M_s = 4$ (left panels) and $M_s = 2$ (right panels), and varying T_i/T_e. We focus on the evolution of the electron spectra to illustrate the reduced electron acceleration efficiency in cases with high T_i/T_e, compared to the $T_i/T_e = 1$ case. For high T_i/T_e runs [panels (a2), (a3), and (b2)], thermal electrons with $K_e < (\gamma_{\rm br,e} - 1)m_e c^2$ (i.e., bulk electron population on the left side of the red dashed-dotted lines) increase steadily over the duration of the simulations, whereas the $T_i/T_e = 1$ cases [panels (a1) and (b1)] show no significant electron heating. Other parameters are identical for all cases: $M_A = 26$ and $v_{\rm pt}/c = 0.25$. 61

4.8 Full version of the energy fractions, similar to Figure 3.6, but including the post-shock (downstream) thermal energy fractions of ions and electrons relative to the total energy. Here we focus on the thermal electron energy fraction $E_e^{\rm th}$ (orange line). Shocks consistently inject a significant fraction of energy into electron heating, resulting in a post-shock thermal electron energy fraction of $E_e^{\rm th}/E_{\rm tot} \sim 0.3$. The $\star$ symbols again indicate cases with $B_{\rm sat}/B_{\rm crit} > 1$. Left panels: effect of the T_i/T_e ratio at fixed $M_s = 4$ in panel (a) and $M_s = 8$ in panel (d). Middle panels: scaling with M_s at fixed $T_i/T_e = 0.01$ in panel (b), and $T_i/T_e = 1$ in panel (e). Right panels: variation with (c) M_A and (f) $v_{\rm pt}/c$. Unless explicitly stated otherwise, parameters are $T_i/T_e = 10$, $M_s = 8$, $M_A = 26$, and $v_{\rm pt}/c = 0.25$. 63

5.1 Various timescales in the BH corona of NGC 1068 as a function of proton energy. The typical acceleration timescale $t_{\rm acc}$ (solid black line) is calculated using Equation (5.6) with $B_0 = 100$ G and $\beta_{\rm sh} = 0.32$. The free-fall timescale $t_{\rm fall}$ (dotted black line) is calculated using Equation (5.1). The simulation results taken from run T10 give the normalization of $t_{\rm acc}$. The gray shaded region indicates the range of $t_{\rm acc}$ when varying $B_0 = 10$–1000 G and $\beta_{\rm sh} = 0.1$–0.5. The cooling timescales for pp interactions t_{pp} (blue line), $p\gamma$ interactions $t_{p\gamma}$ (orange dashed line), and Bethe–Heitler pair production $t_{\rm BH}$ (green dash-dotted line) are calculated following the methods in Inoue et al. (2019). The total cooling timescale $t_{\rm cool}$ (red line) is obtained by combining all cooling processes. The vertical green dashed line marks $E_p = 100$ TeV, representative of the proton energy required to produce TeV neutrinos. 66

List of Tables

3.1 Simulation Parameter Survey 33

Chapter 1

Introduction

A matter is called plasma when it has sufficient energy to break apart atoms to form a cloud of separated ions and electrons. It is the most common state of matter that make up the majority of visible matter in the universe. As a result, the study of plasma physics is entangled with various phenomena in astrophysics and space physics including collisionless shocks. These shocks are formed in the absence of particle-particle collisions and can be studied to understand the dynamics of plasmas and the processes that drive the acceleration of charged particles in the universe.

1.1 Shocks in collisionless plasmas

1.1.1 Overview of collisionless shocks

Fundamentally, a shock wave is a hydrodynamic discontinuity characterized by a sudden, irreversible change in fluid properties—pressure, density, and temperature—propagating faster than the speed of sound in the medium. Historically, this phenomenon was first described in gas dynamics by Ernst Mach, who demonstrated that a shock forms when an object moves through a fluid with a relative velocity V exceeding the local sound speed c_s (Mach & Salcher, 1887). This ratio defines the Mach number, $M = V/c_s$, which remains the primary dimensionless parameter governing shock strength. In neutral fluids, the abrupt deceleration and heating of the flow across the shock front are mediated by binary particle collisions, which convert the directed kinetic energy of the flow into thermal energy over a length scale comparable to the collisional mean free path (Landau & Lifshitz, 1959; Zel'dovich & Raizer, 2002).

In astrophysical plasmas, however, the physical picture is fundamentally different. Most astrophysical environments, including the solar wind and the hot coronae of active galactic nuclei, are so dilute and hot that the Coulomb mean free path exceeds the characteristic system size by orders of magnitude. Under these conditions, binary collisions are too infrequent to mediate shock formation. Instead, the dissipation required to sustain the shock transition is provided by collective electromagnetic interactions. Charged particles respond to self-generated and background electric and magnetic fields, effectively replacing collisions as the agent of randomization. These structures are known as

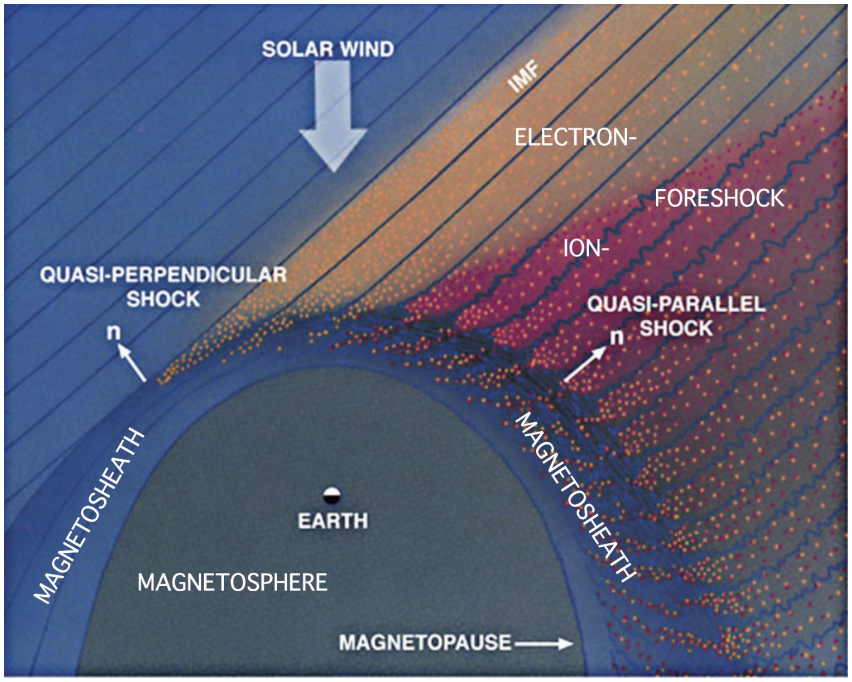

Figure 1.1: Schematic view of the Earth's bow shock, the first confirmed collisionless shock detected in nature. The shock forms as the super-Alfvénic solar wind encounters the obstacle of Earth's magnetosphere. Depending on the angle θ_{Bn} between the shock normal and the upstream magnetic field, the shock is classified as quasi-perpendicular ($\theta_{Bn} > 45°$) or quasi-parallel ($\theta_{Bn} < 45°$), exhibiting distinct particle acceleration properties (Balogh & Treumann, 2013a).

collisionless shocks.

The theoretical existence of collisionless shocks was initially a subject of intense debate, challenging the classical assumption that collisionality was a prerequisite for shock formation (De Hoffmann & Teller, 1950; Marshall, 1955). This controversy was resolved by in-situ spacecraft observations in the 1960s, which provided definitive detection of the Earth's bow shock—a standing shock wave formed by the interaction of the supersonic solar wind with the Earth's magnetosphere (Sonett & Abrams, 1963; Ness et al., 1964).

1.1.2 Laser-driven collisionless shock in laboratory

In general, collisionless shocks are characterized by the mechanism for shock formation and plasma parameters of the shock-containing environment. They can roughly split into two categories: magnetized shock (as the Earth bow shocks) and electrostatic shock. For electrostatic shocks, these structures are formed and sustained by electrostatic potentials in the absence of a background magnetic field (Sagdeev, 1966). Due to the lack of magnetic complexity, they often form stable structures provided there is a sufficient mass and temperature difference between ions and electrons (Forslund & Shonk, 1970). Consequently, they have served as a useful theoretical framework for understanding fundamental kinetic processes in collisionless plasmas.

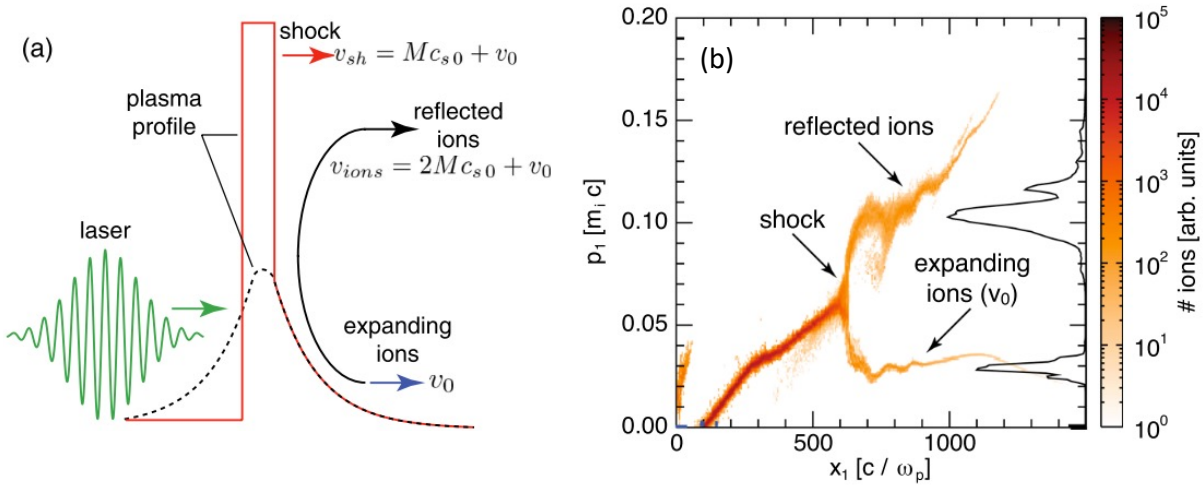

Figure 1.2: Schematic of the setup (a) and phase space results (b) of laser-driven collisionless shock acceleration (CSA) scheme proposed by Fiuza Fiuza et al. (2012, 2013). The reflected ions, gaining twice the shock velocity, demonstrate the efficiency of this scheme for compact ion acceleration.

Notably, it has been demonstrated that electrostatic shocks can be generated in laboratory experiments, which can be used for an alternative proton acceleration method. Such experiments are possible due to the advent of ultra-intense lasers ($I > 10^{18}$ W/cm^2). Schemes such as Collisionless Shock Acceleration (CSA) utilize the strong electrostatic potential at the shock front to reflect and accelerate ions, generating monoenergetic ion beams that are highly desirable for medical and industrial applications (Haberberger et al., 2012; Fiuza et al., 2012). The efficiency of this acceleration depends critically on the stability of the shock structure. In our previous work, we investigated the fundamental properties of these shocks, specifically identifying the conditions for the structural transition between collisionless electrostatic shocks and double-layers (Ly et al., 2023).

Understanding these fundamental limits of electrostatic shock formation provides important context for the more complex, magnetized acceleration mechanisms discussed in the remainder of this thesis. We presented the study of these fundamental shock properties in the Appendix 2.

1.1.3 Collisionless shocks in astrophysical context

As magnetic fields permeate the universe, they couple inevitably with the intrinsic mechanisms of collisionless shock formation. While microphysical instabilities—such as the Weibel instability (Spitkovsky, 2008) and Bell's non-resonant instability (Caprioli & Spitkovsky, 2014a)—mediate the shock transition and turbulence generation, the large-scale magnetic field structure fundamentally dictates the acceleration physics. Consequently, the vast majority of shocks in astrophysical environments, from the Earth's bow shock to supernova remnant (SNR) shocks, are classified as magnetized shocks.

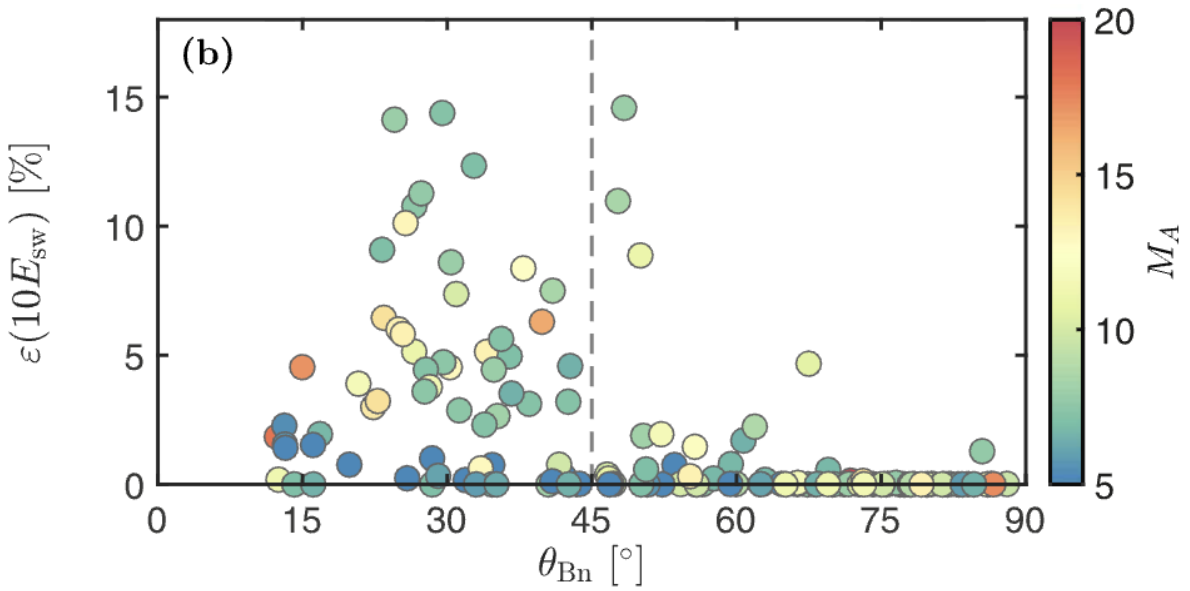

Figure 1.3: Ion acceleration efficiency ε (defined as a percentage of solar wind energy) plotted against the shock obliquity angle $\theta_{\rm Bn}$. The color scale indicates the Alfvén Mach number M_A. The vertical dashed line at 45° marks the transition between quasi-parallel and quasi-perpendicular geometries. Note the sharp suppression of ion acceleration in the quasi-perpendicular regime. Adapted from Johlander et al. (2021).

In these collisionless environments, the magnetic field replaces binary particle collisions as the primary means of compressing matter and mediating shock formation. A critical parameter governing the dynamics of these shocks is the shock obliquity, defined as the angle between the shock normal and the upstream magnetic field vector ($\theta_{\rm Bn}$). This geometric distinction necessitates the classification of shocks into two broad regimes: *quasi-parallel* ($\theta_{\rm Bn} \lesssim 45°$) and *quasi-perpendicular* ($\theta_{\rm Bn} \gtrsim 45°$).

This geometric dichotomy strongly influences particle injection and acceleration efficiencies. Quasi-parallel shocks are renowned as efficient ion accelerators; in this configuration, ions can easily backstream into the upstream region, triggering instabilities that amplify turbulence and facilitate Diffusive Shock Acceleration (DSA). Conversely, quasi-perpendicular shocks are generally inefficient at injecting thermal ions into the DSA mechanism but are often associated with efficient electron acceleration due to different injection physics (e.g., shock drift acceleration).

The stark contrast in ion acceleration efficiency is illustrated in Figure 1.3. Derived from observations and simulations of the Earth's bow shock (Johlander et al., 2021), this plot demonstrates that significant ion acceleration efficiency (ε) is predominantly confined to the quasi-parallel regime ($\theta_{\rm Bn} < 45°$), largely independent of the Alfvén Mach number (M_A). In the quasi-perpendicular regime ($\theta_{\rm Bn} > 45°$), ion energization is heavily suppressed, highlighting the critical role of shock geometry in regulating cosmic ray production.

1.1.4 Numerical method to study collisionless shocks

To investigate the mechanisms of particle acceleration and the formation of non-thermal power-law tails, a description relying solely on macroscopic fluid variables (such as in magnetohydrodynamics) is insufficient. Fluid methods typically assume thermal equilibrium, effectively smoothing over the kinetic processes that are essential for energizing particles. Consequently, a kinetic approach is required to resolve the evolution of the distribution function in phase space.

However, directly solving the Vlasov equation in high-dimensional phase space is computationally prohibitive. The Particle-in-Cell (PIC) method offers an alternative approach to indirectly solve the Vlasov equation by discretizing the distribution function using macroparticles while solving electromagnetic fields on a grid. This method provides a first-principles, self-consistent description of the plasma, capturing the non-linear coupling between electromagnetic microinstabilities and particle trajectories.

Due to its ability to capture these microscopic details, the PIC method is currently the optimal tool for studying collisionless shocks and the genesis of high-energy particles. We will introduce the detailed method including the equations and algorithm in Section 2.2.1.

1.2 Proton acceleration in the vicinity of supermassive black holes: high-energy neutrino signals

The discussion so far has motivated collisionless shocks as natural sites of particle acceleration in plasmas. In this thesis, we apply this kinetic viewpoint to the vicinity of supermassive black holes (SMBHs), motivated by recent high-energy neutrino observations suggesting compact, gamma-ray opaque acceleration sites in active galactic nuclei (AGNs).

1.2.1 Observational motivation

High-energy astrophysical neutrinos are produced in hadronuclear (pp) or photopion ($p\gamma$) interactions of high-energy cosmic rays (CRs). In standard hadronic scenarios, these neutrinos are accompanied by a comparable gamma-ray flux emerging from π^0 decay and subsequent electromagnetic cascades (e.g., Kelner et al., 2006; Kelner & Aharonian, 2008). Therefore, neutrino emitters are often expected to be gamma-ray emitters as well, unless the production region is *opaque* to high-energy photons.

This expectation is challenged by IceCube observations of nearby, radio-quiet AGNs, most notably the Seyfert galaxy NGC 1068, where a neutrino excess has been reported without a corresponding TeV gamma-ray counterpart (see Figure 1.4). The emerging picture is that the neutrino production site is embedded in an environment with large

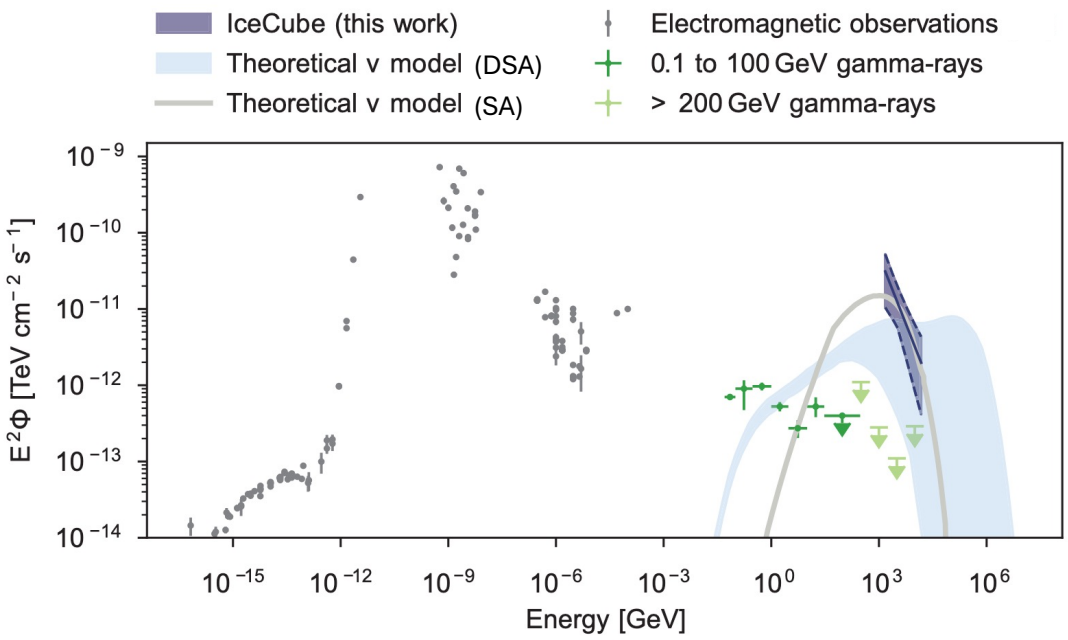

Figure 1.4: Multi-messenger motivation for a "hidden" neutrino source from NGC 1068. Neutrino spectrum (purple band) is an order of magnitude above the γ-ray from Fermi's data. Here, two proton acceleration mechanisms by diffusive shock acceleration (DSA) and stochastic acceleration (SA) were shown to compare with observational results. Adapt from IceCube Collaboration*† et al. (2022).

$\gamma\gamma$ opacity, suppressing escaping GeV–TeV photons while leaving neutrinos unaffected. Although alternative explanations remain under discussion (e.g., multi-zone emission, external cascades, or non-standard hadronic channels), the gamma-ray deficit provides a strong hint that the relevant physics occurs close to the SMBH, where the radiation density is highest.

A practical energetic requirement follows immediately: to produce TeV neutrinos, the parent protons must reach at least $E_p \gtrsim 10^2$ TeV, since a single neutrino typically carries a few percent of the parent proton energy, $E_\nu \sim 0.05\, E_p$. Any viable coronal scenario must therefore provide (i) a compact accelerator capable of reaching $\sim$ 100 TeV–PeV protons, and (ii) sufficient target density (matter and/or photons) for efficient pp and/or $p\gamma$ interactions, while simultaneously (iii) suppressing escaping high-energy gamma rays through internal absorption.

1.2.2 Black hole coronae

A natural candidate for a gamma-ray opaque neutrino production site is a hot corona surrounding the central SMBH, as widely invoked in disk–corona models of AGN X-ray emission. Schematic features of disk–corona are illustrated in Figure 1.5. The corona is a compact, hot plasma responsible for the hard X-ray continuum via Comptonization of softer disk photons. Observationally and phenomenologically, it is characterized by

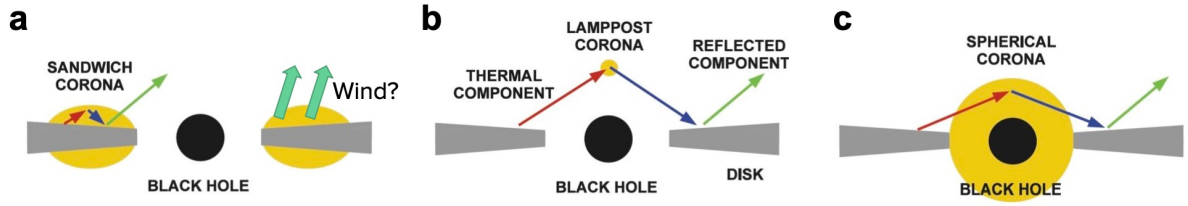

Figure 1.5: Schematic of possible coronal geometries in disk–corona system around an SMBH. Thethermaldiskemission(red)is up-scattered by hot electrons in the corona. The resulting high-energy photons (blue) reflect off the disk, which then emits "reprocessed" light(green). Adapt from Bambi et al. (2021).

electron temperatures $T_e \sim 10^9\,\mathrm{K}$ (tens to hundreds of keV) and a characteristic size of order ~ 10–$10^2\,R_g$, where $R_g \equiv GM/c^2$ is the gravitational radius. The geometry is still debated (e.g., patchy/extended versus lamppost-like), but multiple lines of evidence suggest that the X-ray emitting region is compact and located within the innermost disk environment.

From a plasma-physics perspective, the coronal environment is inherently collisionless: Coulomb coupling is inefficient on dynamical timescales, so electrons and ions need not share a common temperature. This naturally motivates two-temperature coronal plasmas with $T_i \neq T_e$, and in particular $T_i \gg T_e$ in weakly collisional regimes. In addition, recent mm observations of nearby Seyferts suggest magnetic field strengths of order $B \sim 10$–$100\,\mathrm{G}$ in the coronal region, implying Alfvénic speeds $v_A/c \ll 1$ under typical coronal densities. These constraints are important because they bound the magnetization and thus the efficiency of candidate acceleration mechanisms.

The coronal radiation field also provides the essential ingredient for gamma-ray opacity. Comptonized X-ray photons yield large $\gamma\gamma$ pair-production optical depths for GeV–TeV gamma rays produced in situ, naturally suppressing the gamma-ray counterpart of hadronic neutrino production. At the same time, neutrinos produced via pp or $p\gamma$ interactions escape freely, allowing the corona to operate as a "hidden" neutrino source.

1.2.3 Acceleration mechanism of protons

The dominant mechanism that accelerates protons in SMBH coronae remains uncertain. A range of scenarios have been proposed, including diffusive shock acceleration (DSA; Inoue et al., 2019, 2020, 2024a), stochastic (second-order Fermi) acceleration (SA; Murase et al., 2020; Kheirandish et al., 2021; Mbarek et al., 2023; Fiorillo et al., 2024a), magnetic reconnection (Fiorillo et al., 2024b; Karavola et al., 2025), and hybrid cases where multiple processes act in sequence or in parallel.

Each mechanism faces distinct constraints in a realistic coronal environment. SA requires sustained strong turbulence and typically becomes slow when the Alfvén speed is small, as indicated by the weak magnetization inferred for nearby Seyferts. Reconnection

can be powerful if the corona is strongly magnetized and forms large-scale current sheets, but its efficiency, particle spectra, and the accompanying pair creation depend sensitively on the magnetic topology and radiative compactness. By contrast, DSA offers a conceptually direct route to producing non-thermal ions provided collisionless shocks exist and can inject ions efficiently into repeated shock crossings (see Section 1.1.3).

An additional complication is that coronal shocks are likely *low* sonic Mach number, with M_s of order a few. In conventional astrophysical lore, low-M_s shocks are often regarded as "weak" and therefore inefficient accelerators. However, this expectation is largely based on fluid-level reasoning or parameter regimes distinct from BH coronae. The coronal case is intrinsically kinetic: it involves trans-relativistic flows, two-temperature plasmas ($T_i/T_e \gg 1$ is plausible), and magnetized oblique shocks where the ion injection physics is not captured by macroscopic treatments. This motivates a first-principles approach.

1.2.4 Why diffusive shock acceleration?

In this thesis we focus on DSA as a leading candidate for proton acceleration in SMBH coronae, guided by three considerations.

First, DSA directly connects to the shock physics introduced earlier in this chapter: quasi-parallel magnetized shocks are naturally efficient ion accelerators (Section 1.1.3), since backstreaming ions can drive turbulence upstream and sustain repeated crossings. If coronal dissipation produces shocks with extended quasi-parallel patches (e.g., in turbulent accretion flows or magnetically structured coronae), ion acceleration at the $> 5\%$ level is plausible in principle (Inoue et al., 2019, 2020).

Second, compared to other mechanisms, recent observational results favor DSA. In particular, millimeter observations of nearby Seyferts point to coronal magnetic field strengths of roughly 10 to 100 G (Inoue & Doi 2018; Inoue et al. 2020; Michiyama et al. 2023; Shablovinskaya et al. 2024; Michiyama et al. 2024; del Palacio et al. 2025; Jana et al. 2025; Mutie et al. 2025, but see also Hankla et al. 2025) corresponding to the Alfven speed of $v_A/c \sim 10^{-2} - 10^{-3}$. Such weak field conditions are generally unfavorable for efficient SA or magnetic reconnection. Nonetheless, the viability of each mechanism under realistic coronal conditions remains a subject of active debate, partly due to the limited first-principles constraints tailored to SMBH coronae.

Third, and most importantly, the main uncertainty for DSA in coronae is quantitative constraints of the acceleration rate and efficiency in the relevant kinetic regime. This is precisely where first-principles particle-in-cell (PIC) simulations become essential. Fluid approaches cannot capture the microphysical injection of ions, the self-generated turbulence, or the non-thermal tail formation that ultimately determine whether ~ 100 TeV protons can be produced.

Motivated by these considerations, we adopt PIC simulations tuned to BH coronal parameters and perform a controlled survey of quasi-parallel shocks across the ranges of sonic Mach number, Alfvénic Mach number, shock velocity, and ion-to-electron temperature ratio motivated by Seyfert observations. This provides direct, kinetic constraints on (i) the proton acceleration rate, and (ii) the energy partition into non-thermal ions and electrons, which can be fed into neutrino-production models for sources such as NGC 1068.

1.3 Plan and structure of this thesis

This thesis is organized as follows.

In Chapter 2, we first introduce the fundamental properties of collisionless shocks, with particular emphasis on the formation limits of shocks in the absence of a magnetic field and on electrostatic shocks. This chapter provides the kinetic foundation and complementary context for the acceleration mechanisms in magnetized shocks discussed in the later chapters.

In Chapter 3, we present the core results of this study. We analyze the shock structure and develop a unified picture of particle acceleration in representative coronal shocks. This is followed by a parameter survey that maps the proton acceleration efficiency and acceleration rate across the relevant parameter regime.

In Chapter 4, we investigate the magnetic-field evolution and electron dynamics in collisionless shocks. We link strong magnetic-field amplification to the suppression of electron acceleration and discuss the reduced acceleration efficiency associated with the high T_i/T_e regime.

In Chapter 5, we explore the implications of our results for neutrino production in Seyfert galaxies, focusing on the well-studied case of NGC 1068.

Finally, Chapter 6 summarizes the main conclusions and outlines open problems and directions for future work.

Chapter 2

Fundamental Properties of Collisionless Shocks: On Collisionless Electrostatic Shock Formation

---

Prologue

This chapter studies the fundamental properties of collisionless shocks, focusing on shock formation and reflection as a dissipation mechanism. We examine the limit of this mechanism (full reflection), beyond which the system undergoes a structural transition from a shock to an electrostatic double-layer. This work was published in Ly et al. 2023.

Collisionless shock acceleration, which transfers localized particle energies to non-thermal energetic particles via electromagnetic potential, is ubiquitous in space plasma. We investigate dynamics of collisionless electrostatic shocks that appear at interface of two plasma slabs with different pressures using one-dimensional particle-in-cell (PIC) simulations and find that the shock structure transforms to a double-layer structure at the high density gradient. The threshold condition of the structure transformation is identified as density ratio of the two plasma slabs $\Gamma \sim 40$ regardless of the temperature ratio between them. We then update the collisionless shock model that takes into account density expansion effects caused by a rarefaction wave to improve the prediction of the critical Mach numbers. The new critical Mach numbers are benchmarked by PIC simulations for a wide range of Γ. Furthermore, we introduce a semi-analytical approach to forecast the shock velocity just from the initial conditions based on a new concept of the accelerated fraction α.

2.1 Introduction

The realization of collisionless shock fundamentally changed the field of shock and plasma physics. The collective excitation of plasmas based on wave-particle interactions forms

shock structures as a mediating mechanism that replaces collisions and has important implications for the kinetic theory of plasmas Marcowith et al. (2016); Huntington et al. (2015). On the application side, most astrophysical shocks, from bow shocks at Earth's magnetosphere to supernova remnant shocks Perri et al. (2022); Oka et al. (2017); Koyama et al. (1995), are collisionless and thought to be closely related to the origin of cosmic rays Blandford & Eichler (1987a); Blasi (2013). Recent advances in ultra-intense lasers have brought electrostatic shock, a type of collisionless shock, to the laboratory, enabling the generation of high-energy ion beams with a narrow energy band for medical applications Fiuza et al. (2012, 2013); Haberberger et al. (2012). Because of these attractive applications and the importance of exploring fundamental physics, collisionless shocks have become a topic of increasing interest in recent years Russell et al. (2021); Fiuza et al. (2012); Malkov et al. (2016); Sakawa et al. (2021).

Studies of shock formation often use particle-in-cell (PIC) simulations to investigate the associated kinetic processes in detail Sorasio et al. (2006); Sarri et al. (2011a); Fiuza et al. (2012); Dieckmann et al. (2013a); Russell et al. (2021). The shocks can be triggered at interface of two plasma slabs with different pressures in various configurations such as initial density ratios and initial temperature differences. The subsequent nonlinear evolution generates a steady-state shock structure characterized by an accompanying electrostatic potential. Although conditions of the formation of collisionless shocks have been studied extensively, yet an important detail had been overlooked: the emergence of a shock-like structure known as a double-layer instead of a conventional shock structure Dieckmann et al. (2013b).

In the context of space and astrophysical plasmas, double-layer structures were observed in shock-forming areas such as the Earth's magnetosphere Ergun et al. (2009); Sun et al. (2022) and solar flares Li et al. (2012) highlighting the need to differentiate these two phenomena. In general, a collisionless shock or shock structure assumes that particles will move from a lower pressure region (upstream) to a higher pressure region (downstream) in the rest frame of the shock interface. In contrast, the opposite flow direction appears in the double-layer structures as ions move from the higher pressure side to the lower pressure side Hershkowitz (1981). By tracking the origin of particles moving from the transition region to the upstream, we can identify the two structures and reconsider the theoretical framework for double-layer structure formation.

The theoretical analysis of electrostatic shocks is usually discussed within Sagdeev's analogy of a particle moving inside a pseudo-potential Sagdeev (1966). Following the framework, we can derive the critical Mach number as the largest possible value for how fast shocks can move. Over the years, it has been generalized by Sorasio et al. Sorasio et al. (2006) for non-relativistic temperatures and relativistic temperatures Fiuza et al. (2012, 2013); Stockem et al. (2013). However, the relationship between the critical Mach number and the Mach number obtained in the simulation has an inconsistency. The shock

speed in simulations exceeds the critical Mach number theoretically predicted in some cases. To overcome this inconsistency, we propose a new collisionless shock model that incorporates the previously reported density drop due to plasma expansion Sarri et al. (2011a,b); Russell et al. (2021). This aspect has yet to be analytically included in the current shock model. In addition, we also present modifications to the mass conservation equation with accelerated fraction as a new parameter to match the ion reflections and the double-layer framework.

The outline of this paper is as follows. In Sec. 2.2, we present PIC simulations including the setup and how we use the results to identify the double-layer structure. The transition from a collisionless shock to a double-layer structure is found to occur when increasing the initial density ratio. The critical value of the density ratio for the transition is also derived. In Sec. 2.3, we introduce the current analytical model and propose the necessary changes to get a more consistent and accurate model. First, we consider the density drop due to rarefaction expansion and propose a new model for the critical Mach number. Then, we obtain predictions of Mach numbers by modifying the mass conservation law to take ion reflection into account. Finally, in Sec. 2.4, we discuss the relationship between the critical Mach numbers and numerical results and the possible interpretation of why the density ratio Γ determines collisionless shock or double-layer structure.

2.2 Particle-in-cell simulation

In this section, we first describe the PIC method used throughout this thesis. We then present the simulation setup adopted to study the formation of collisionless electrostatic shocks.

2.2.1 Numerical methods

There are generally two categories of numerical simulations in plasma physics: kinetic methods, which portray the evolution of the distribution function $f(\boldsymbol{x}, \boldsymbol{v}, t)$ in 6D phase space $(\boldsymbol{x}, \boldsymbol{v})$, and fluid methods, which approximate the system using macroscopic spatial distributions $f(\boldsymbol{x}, t)$ (typically assuming a Boltzmann distribution in the strong collisional limit). Kinetic methods for collisionless plasmas are modeled by the Vlasov equation:

$$\frac{\partial f}{\partial t} + \boldsymbol{v} \cdot \frac{\partial f}{\partial \boldsymbol{x}} + \frac{q}{m}\left(\boldsymbol{E} + \frac{\boldsymbol{v} \times \boldsymbol{B}}{c}\right) \cdot \frac{\partial f}{\partial \boldsymbol{v}} = 0 \,. \tag{2.1}$$

However, solving Eq. (2.1) directly is challenging due to the constraints of computational resources in high-dimensional phase space. The PIC method offers an alternative approach to indirectly solve the Vlasov equation by using particle approximation to dis-

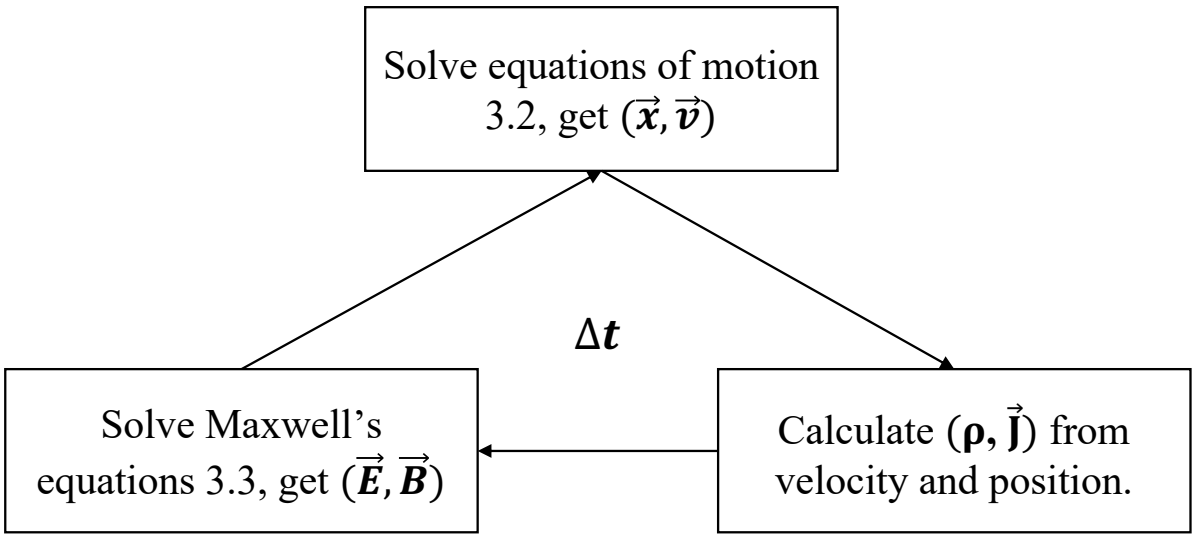

Figure 2.1: Summary of the PIC scheme for a self-consistent description of the evolution of the plasma system.

cretize $f(\boldsymbol{x}, \boldsymbol{v}, t)$ (Sentoku & Kemp, 2008). We model the system using N macroparticles, where the trajectory of the j-th particle is governed by the equations of motion:

$$\frac{d\boldsymbol{v}_j}{dt} = \frac{q_j}{m_j}\left(\boldsymbol{E} + \frac{\boldsymbol{v}_j \times \boldsymbol{B}}{c}\right) , \tag{2.2a}$$

$$\frac{d\boldsymbol{x}_j}{dt} = \boldsymbol{v}_j , \tag{2.2b}$$

where j is the particle index. The electromagnetic field information in Eqs. (2.2) is derived self-consistently from Maxwell's equations:

$$\nabla \cdot \boldsymbol{E} = 4\pi\rho , \tag{2.3a}$$

$$\nabla \cdot \boldsymbol{B} = 0 , \tag{2.3b}$$

$$\nabla \times \boldsymbol{E} = -\frac{1}{c}\frac{\partial \boldsymbol{B}}{\partial t} , \tag{2.3c}$$

$$\nabla \times \boldsymbol{B} = \frac{4\pi \boldsymbol{J}}{c} + \frac{\partial \boldsymbol{E}}{\partial t} , \tag{2.3d}$$

where $\rho(\boldsymbol{x}) = \sum_j q_j S(\boldsymbol{x} - \boldsymbol{x}_j)$ is the charge density, and $\boldsymbol{J}(\boldsymbol{x}) = \sum_j q_j \boldsymbol{v}_j S(\boldsymbol{x} - \boldsymbol{x}_j)$ is the current density, with $S(\boldsymbol{x})$ denoting the particle shape function.

This set of equations expresses the evolution of plasmas in a self-consistent manner. The detailed procedure is summarized in Fig. 2.1. First, macroparticle trajectories are updated using electromagnetic field information interpolated to the particle positions. Second, the positions and velocities obtained from this step are used to deposit charge and current densities onto the simulation grid. Finally, we solve Maxwell's equations on the grid to update the electromagnetic fields for the next time step.

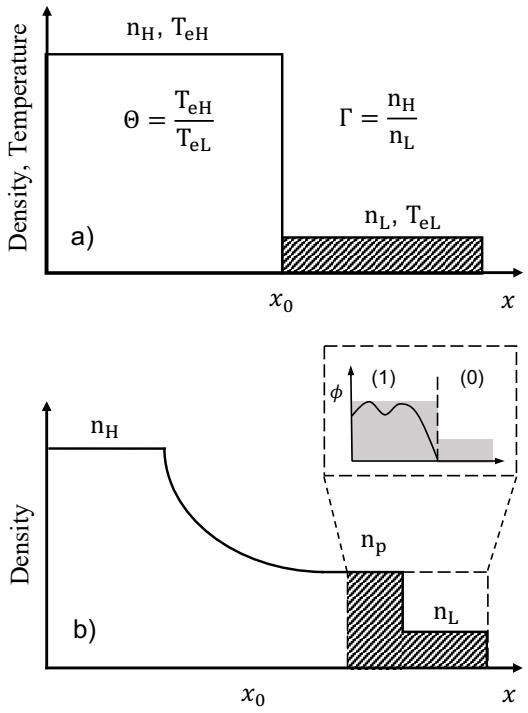

Figure 2.2: (a) The initial setup of PIC simulations is illustrated. Two slabs of plasma with the density ratio Γ and temperature ratio Θ are presented in different shades. (b) A typical ion density profile at the shock's steady-state indicates density reduction near the shock front due to the expansion of the high density slab. The electrostatic potential ϕ created by the interactions of two slabs at the front is depicted in the inset. The shock upstream region (low density) and the downstream region are denoted by (0) and (1), respectively.

2.2.2 Numerical setup

We study shock formation from the interactions of two semi-infinite plasmas by 1D PIC simulations. The two slabs of plasmas are initiated with different densities and temperatures indicated by the density ratios $\Gamma = n_H/n_L$, and temperature ratios $\Theta = T_{eH}/T_{eL}$. The schematic figure of our simulation setup is illustrated in Fig. 2.2(a). Figure 2.2(b) depicts a typical structure in steady-state showing the expansion front, and shock transition region (downstream and upstream regions in shaded area). Simulations were performed using a 1D PIC code, PICLS Sentoku & Kemp (2008), with a realistic proton-to-electron mass ratio 1836. The length of the simulation box is 4000 c/ω_{pe} with 80000 grid cells and 35-100 particles per cell for each electron and proton. The simulations ran for a total time of 5000 ω_{pe}^{-1} with a temporal resolution of $dt = 0.05\ \omega_{pe}^{-1}$. The length of the simulation box and running time ensure that electrons from the interface do not yet reach the boundaries during entire calculation. The reflective boundary condition for particles is applied for simplicity. In the simulations, the left plasma slab is used as the reference, with its temperature and density remaining constant. While the right slab's density and temperature are varied to change the initial ratios. The left plasma was initialized with a

non-relativistic temperature of $T_{eH} = 10$ keV. We start with cold hydrogen ions ($T_i = 0$) for both plasmas. Two slabs are divided evenly in the computation domain so that the initial interface is located at $x_0 = 2000\, c/\omega_{pe}$. In addition, to observe the structural transition of the shocks, we placed particular indexes on particles to label their origin and tracked them in simulations.

As shown in Fig. 2.2(b), the expansion of plasma causes density reduction from the initial density n_H to n_p in the plateau region near the shock front Sarri et al. (2011b); Moreno et al. (2020). Particles in the right slab with density n_L interact with the expanding left slab and form the downstream shock region (1). Strictly speaking, the plateau density indicates the density of particles from the left plasma while the downstream region is filled with the right slab's particles. Because the two densities have equal values as indicated later in our study [Fig. 2.3(a) and 2.3(d)], we will use the notation n_p for the downstream density in the following discussions.

2.2.3 The transition of shock structures

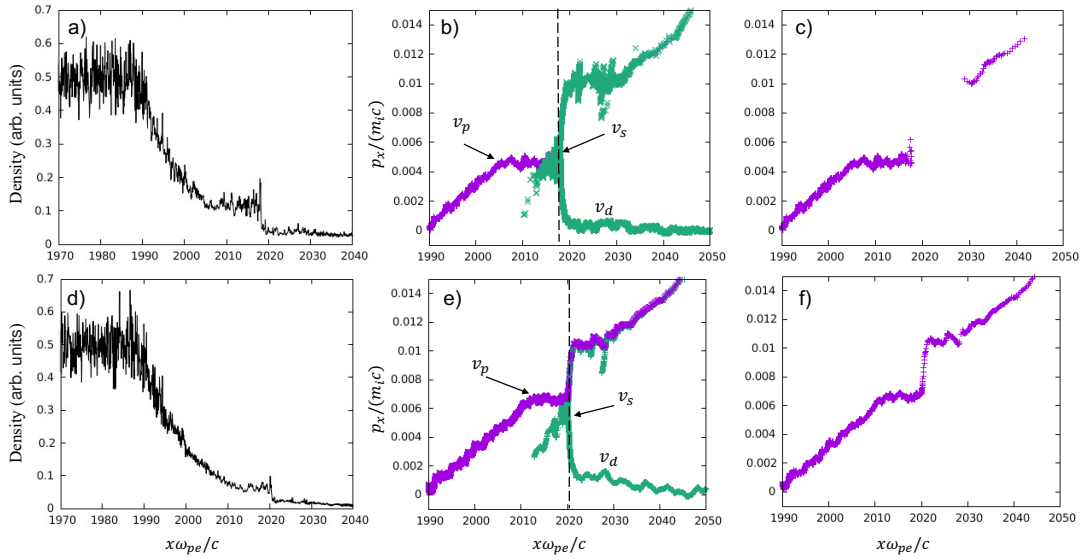

Figure 2.3: Ion density profiles and phase space structures from simulations at $t = 3500\ \omega_{pe}^{-1}$ with $\Theta = 1$ ($T_{eH} = 10$ keV), $\Gamma = 20$ for (a) and (b), $\Gamma = 100$ for (d) and (e). Ions from the high density slab are represented as purple in (b) and (e), while those from the low density slab are marked as green. (c) and (f) are p_x-x diagrams the same as (b) and (e), but only show particles originating from the higher density region.

From the initial setup, the two plasma slabs are released to freely evolve. The higher density slab on the left expands to the lower density side and a collisionless shock is formed in the transition region [see Fig. 2.3(a) and 2.3(b)]. The shock is electrostatic in nature due to the sufficient temperature and mass ratio between ions and electrons used in our simulations Stockem Novo et al. (2016). The shock Mach number, which is the ratio of shock propagating velocity to upstream (lower density region) ion sound

speed $M_s = v_s/c_{s0}$, characterizes shock-particle interactions. In the shock rest frame, ions from the upstream region move toward the shock with the shock velocity and they are decelerated by the electrostatic potential before going to the downstream region. At the electrostatic shock front, a fraction of ions is reflected back to the upstream region with twice the shock velocity.

Figure 2.3 shows the ion density profile and the phase space structures of two simulations (at $t = 3500\ \omega_{pe}^{-1}$) with two different density ratios $\Gamma = 20$ (the upper panels) and $\Gamma = 100$ (the lower panels). A uniform temperature $\Theta = 1$ is assumed for both cases. The shock velocities v_s are derived from tracking the front position over time. The shock Mach numbers are 1.60 and 1.75 for $\Gamma = 20$ and 100, respectively. They are consistent with non-relativistic results reported previously Fiuza et al. (2013). However, when taking the origin of ions into account, these two results exhibit quite different characteristics. For the case of $\Gamma = 20$, a large fraction of ions from the right slab passes through the shock front and form the shock downstream in the region of $x \sim 2015\ c/\omega_{pe}$ as seen in Fig. 2(b). The particles from the left slab are not able to reach the shock front just like the fluid shock cases, except for some ions moving before the shock formation [Fig. 2.3(c)], since the expansion plateau velocity v_p is a bit slower than the shock velocity v_s. On the other hand, when $\Gamma = 100$, the particle flow is opposite to the standard shock picture. Almost all the particles from the right are reflected at the front after the formation of the steady structure. Instead, as shown in Figs. 2.3(e) and (f), particles from the left overtake the shock front and jump in momentum space, driven by the electrostatic potential. Similar to the case of the plateau density n_p, the plateau velocity v_p is also used to indicate the downstream velocity of the shock. Ions in the upstream region ahead of the shock gain net drifting velocity v_d because of the stream of reflected ions [see Fig. 2.3(e)].

The opposite flow observed in the case of $\Gamma = 100$ occurs because the expanding velocity of the left slab v_p becomes faster than the shock velocity v_s. As a result, ions from the high density side overtake the shock front and enter the low density region. To find the critical value Γ for such transition, we conducted a series of simulations with varying Γ from 4 to 100 for two temperature ratios $\Theta = 1$ and $\Theta = 20$. The values of v_s (v_p) observed in the simulations are plotted by red (blue) circles in Fig. 2.4(a) for $\Theta = 1$ and Fig. 2.4(b) for $\Theta = 20$. The blue solid line and the black solid line in Fig. 2.4(a) indicate the model for v_p and v_s which will be explored in depth in Sec. 2.3 B and D, respectively. It is evident from Fig. 2.4(a) that the plateau velocity v_p exceeds the shock velocity v_s with Γ greater than about 40, which is the critical Γ initiating the transition from the well-known collisionless shock structure to the other one. Simulations with different initial temperature ($\Theta = 20$) [Fig. 2.4(b)] yielded no significant impact on the transition and its critical Γ which remains around 40 similar to the case with $\Theta = 1$. Notice that the shock Mach number becomes larger for larger temperature ratios (for $\Theta = 20$ compared to $\Theta = 1$), but the shock velocity has little change.

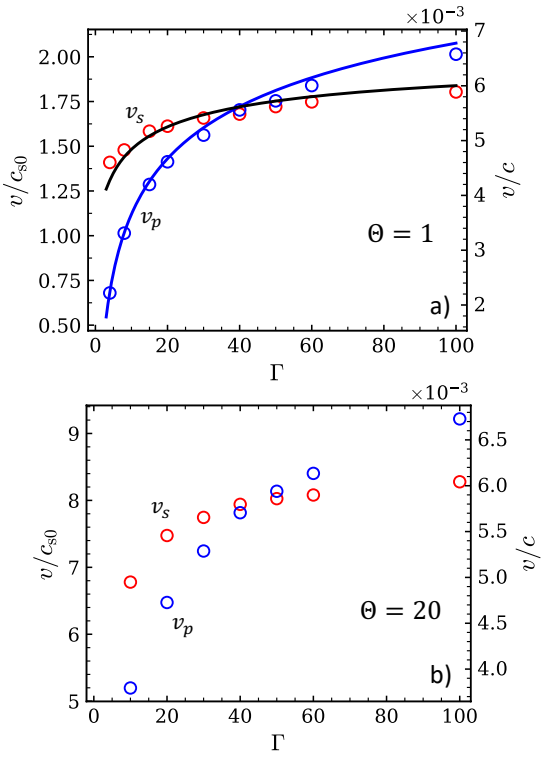

Figure 2.4: Comparison between v_p (blue circles) and v_s (red circle) from the simulations (in laboratory frame) for varying $\Gamma = 4-100$ with $\Theta = 1$ (a) and $\Theta = 20$ (b). The data is illustrated in two scales. The left label is normalized by the sound speed of the upstream plasma c_{s0}, which varies with Γ. The right label is normalized by the speed of light c which are common scale for both panels. In (a), the blue solid line shows v_p from Eq. (2.8) Allen & Andrews (1970); Perego et al. (2013) and v_s (black solid line) is calculated from the semi-analytical model discussing in Eq. (2.12). It can be seen that the transition occurs around $\Gamma = 40$ in both cases.

Studies of the Earth's auroras and early laboratory experiments identified the structures with the opposite flow as double-layer structures Goertz (1979); Hershkowitz et al. (1981). The conditions to differentiate double-layer and electrostatic shock are given by Hershkowitz (1981) with the main difference being the direction of ion flowing through the electric potential called the free ion flow. Figures 2.5 indicate the schematic phase space structures of double-layer (a) and electrostatic shock (b), in turn, consistent with our simulations with $\Gamma > 40$ and $\Gamma < 40$. The electric potential exists in the transition region in both cases but plays different roles in the free ions flow. In the rest frame of the potential, a double-layer structure is characterized by free ion flow from the higher potential side while the flow from the lower potential side corresponds to the collisionless electrostatic shock.

In the next section, we will discuss how we can modify the conventional theory of collisionless shock to accommodate the structural transition.

2.3 Analytical model for steady-state of electrostatic shocks

For collisionless electrostatic shocks, analytical models had been developed based on Sagdeev's paradigm Sagdeev (1966). Later studies had explored the role of initial conditions, such as density ratio Γ and temperature ratio Θ, on the shock formation Sorasio et al. (2006); Stockem et al. (2013). We here focus on non-relativistic shocks and follow closely the approach laid out in Sorasio et al. Sorasio et al. (2006) which was later adopted in Fiuza et al. (2012, 2013).

2.3.1 The conventional model for the critical Mach number

The electric potential of the shocks [the inset from Fig. 2.2(b)] can be expressed by the one-dimension Poisson equation,

$$\epsilon \frac{d^2\phi}{dx^2} = e(n_e - n_i) \, . \tag{2.4}$$

where $\phi(x)$ is the electrostatic potential of the shock, ϵ is the permittivity of plasma, and n_i (n_e) are the ion (electron) density. To obtain the Sagdeev's characteristic equation, we integrate Eq. (2.4) with respect to ϕ in a condition of $\phi(0) = 0$. The result is the following equation:

$$\frac{1}{2}\left(\frac{d\varphi}{d\chi}\right)^2 + \Psi(\varphi) = 0 \, , \tag{2.5}$$

where we use the normalized units for the potential $\varphi = e\phi/T_{e0}$ with T_{e0} is the upstream electron temperature, and space $\chi = x/\lambda_D$ with the Debye length $\lambda_D = \sqrt{\epsilon T_{e0}/e^2 n_L}$.

$\Psi(\varphi)$ is the non-linear Sagdeev's potential given by $\Psi(\varphi) = P_i(\varphi) - P_e(\varphi)$ as the difference of ion pressure $P_i(\varphi)$ and electron pressure $P_e(\varphi)$.

Only when $\Psi(\varphi) < 0$ a shock is developed, and its characteristics, such as its Mach number M_s, can then be resolved Tidman & Krall (1971). In addition, the shock formation requires the conditions; the potential energy should not exceed the kinetic energy of the shock, $\varphi < M_s^2/2$, otherwise all ions would be reflected. With these two conditions the upper limit of the shock Mach number often called the critical Mach number, $M_{\rm cr}$, can be derived. The numerical solutions can be obtained by solving $\Psi(\varphi_{\rm max} = M_{\rm cr}^2/2) = 0$ or if we write in full detail Fiuza et al. (2013)

$$M_{\rm cr}^2 = \frac{1}{1+\Gamma}\left\{\frac{\sqrt{2}\,M_{\rm cr}}{\sqrt{\pi}} + e^{\frac{M_{\rm cr}^2}{2}}\,{\rm erfc}\left(\frac{M_{\rm cr}}{\sqrt{2}}\right) - 1 \right. \\ \left. + \Gamma\Theta\left[\frac{\sqrt{2}\,M_{\rm cr}}{\sqrt{\pi\Theta}} + e^{\frac{M_{\rm cr}^2}{2\Theta}}\,{\rm erfc}\left(\frac{M_{\rm cr}}{\sqrt{2\Theta}}\right) + \frac{4M_{\rm cr}^3}{3\sqrt{2\pi\Theta^3}} - 1\right]\right\}. \tag{2.6}$$

where erfc is the complementary error function.

To accurately derive the shock Mach number M_s from simulation results in the laboratory frame, it is necessary to account for the upstream drift v_d. This is because the shock Mach number is defined in the upstream rest frame where the upstream ions are stationary. To accomplish this, we calculate the shock Mach number as $M_s = (v_s - v_d)/c_{s0}$, where v_s is the shock velocity, and v_d is the upstream drift velocity both measured in the laboratory frame. Throughout the rest of the paper, when we mentioned the Mach number M_s without specifying the frame, we have already excluded the drift velocity v_d from the results. The results of critical Mach numbers calculated from Eq. (2.6) are shown with a black dashed line in Fig. 2.6 in comparison with our simulation results.

The Mach numbers observed in the simulations (red dots) exceed the critical Mach number given by Eq. (2.6) for the cases of $\Gamma > 15$. This fact indicates that the theoretical model needs to be improved. For example, in the previous work, all ions are assumed to pass downstream without reflection. Then the partial reflection is not considered in the model. The density expansion effect is also ignored. Including these effects is the primary focus of our investigation and will be addressed in detail in the following discussion.

2.3.2 The density ratios after the isothermal expansion

In this section, we will present a new shock model that can address a change in the density at the expanding front from the initial value. As the structural transition from collisionless shocks does not depend significantly on the initial temperature ratio Θ as showing above, we focus the subsequent discussion solely on the case of $\Theta = 1$ for simplicity. This implies that the initial sound speed c_s remains constant throughout the region ($c_s = c_{s0} = c_{s1}$). Nevertheless, a general analysis can be easily performed simply by changing the sound

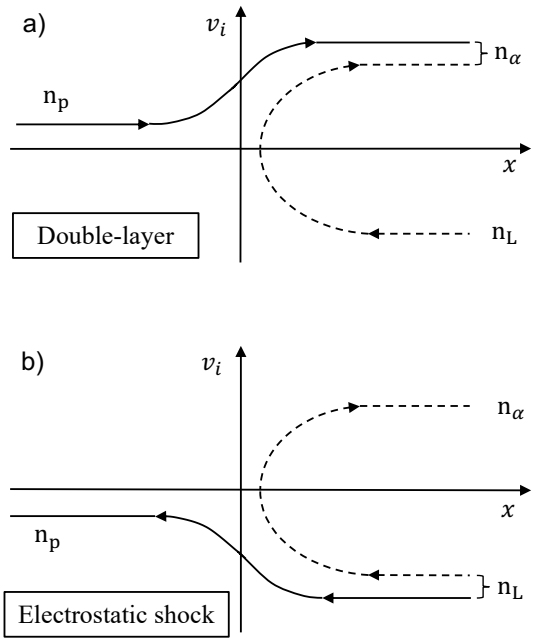

Figure 2.5: Ion phase space in the moving shock frame for double-layer (a) and collisionless electrostatic shock (b) according to Ref. Hershkowitz (1981). In Sec. 2.3. D, the density of the accelerated ions n_α or ions moving outward from the front, and the accelerated fraction $\alpha = n_\alpha/n_L$ are explained in detail. For electrostatic shocks, n_α is primarily the density of reflected ions while for double-layer structures it also includes the transmitted fraction originating from the high density plasma.

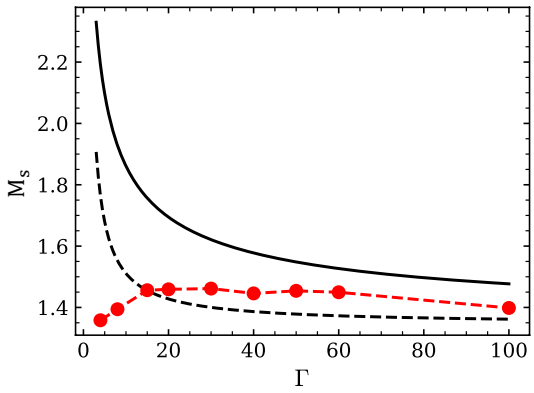

Figure 2.6: The conventional critical Mach number (black dashed line) is obtained from solving Eq. (2.6) with varying Γ and $\Theta = 1$. The new critical Mach numbers (black solid line) are calculated using $\Gamma' = n_p/n_L$ calculated from Eqs. (2.7) and (2.8). Simulation results of the shock Mach number M_s with corresponding Γ ($\Theta = 1$) are shown by red dots. M_s from the simulations exceeds the conventional upper limit but is less than the new model's limit.

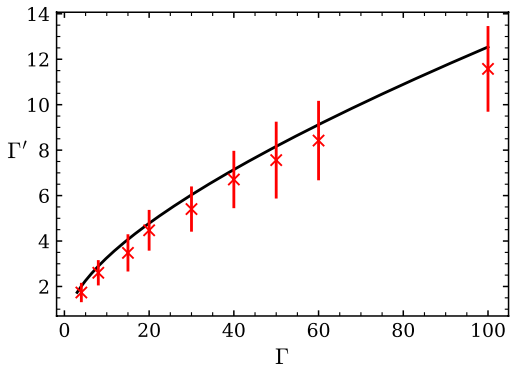

Figure 2.7: The density ratios at the expansion front Γ' (black solid line) with respect to the initial values calculated by Eqs. (2.7) and (2.8) in comparison with simulation results (red crosses). The bars represent the error evaluated from the density fluctuations in the simulations.

speed when $\Theta \neq 1$. The previous model assumes that the density ratios at steady-state shock fronts are the same as the initial values. While this assumption is valid when the initial density ratio is small, for the higher Γ, we observed the density ratios drop substantially from the initial values as seen in Fig. 2.3(a) and 2.3(d).

A model for planar isothermal rarefaction waves (see Ref. Drake (2018)) is applicable to obtain the density ratios in the expansion front, $\Gamma' = n_p/n_L$. The justification for using the isothermal model is based on the fact that a semi-infinite slab of plasma is sufficiently large to supply heat continuously during the expansion. The self-similar solution of the model gives the following relation,

$$\Gamma' = \Gamma \exp\left(-\frac{v_p}{c_s}\right) \ , \tag{2.7}$$

where v_p plays the role of the piston velocity of the expansion.

The validity of the previous model remains for the steady-state expanding front. This, in turn, allows us to derive more accurate critical Mach numbers by incorporating the conventional model with the front density ratios Γ' as given by Eq. (2.7). In addition, if we can resolve v_p from initial conditions, we will have an initial value problem $M_{cr}(\Gamma, \Theta)$ similar to the previous model.

From the well-known quasi-neutral model of gas dynamic (see Ref. Allen & Andrews (1970) and Ref. Perego et al. (2013)), v_p is given by

$$\left[1 - \frac{1}{\Gamma}\exp(v_p/c_s)\right]\left[\left(\frac{v_p}{c_s}\right)^2 - \frac{2v_p}{c_s} - 2\log\left(\frac{1}{\Gamma}\right)\right] - 2\left(\frac{v_p}{c_s}\right)^2 = 0 \ . \tag{2.8}$$

The plateau velocity v_p obtained from Eq. (2.8) is plotted in Fig. 2.4(a) (blue solid line)

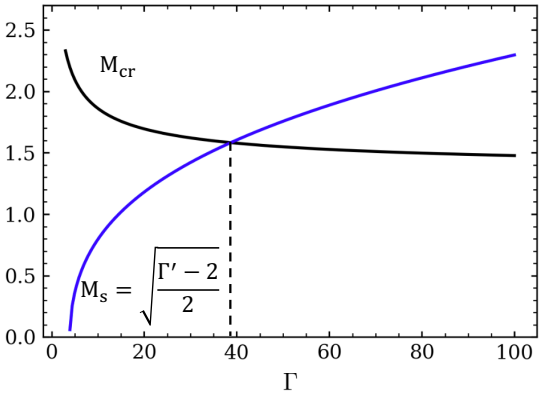

Figure 2.8: The transition condition predicted by Eq. (2.11) is $\Gamma \sim 40$, which indicated from the crossing point of $M_{\rm cr}$ (black solid line) and $M_s = \sqrt{\Gamma' - 2)/2}$ (blue solid line). $M_{\rm cr}$ is obtained from our new model, and Γ' relation with Γ is given by the black solid line in Fig. 2.7.

showing a great agreement with the PIC simulation results. Using v_p and Eq. (2.7), we can calculate the expanding density ratio Γ' which is shown in Fig. 2.7 with a black solid line in comparison with simulations. With v_p and Γ' derived from hydrodynamic models showing consistency with the simulation results, we can conclude that the plasma far downstream exhibits fluid-like behavior instead of kinetic dynamics as the transition region. The new critical Mach numbers are obtained by solving Eq. (2.6) using Γ' instead of Γ. The calculated results are illustrated in Fig. 2.6 with a black solid line. The critical Mach numbers predicted by the new model are higher than the shock Mach numbers M_s obtained from simulations, satisfactorily serving as the upper limit for allowed shock velocities.

2.3.3 Prediction of the transition from collisionless shock to double-layer structures

The new model of $M_{\rm cr}$ shown in Fig. 2.6 allows us to predict the transition from the collisionless shock to the double-layer structure. Here, to evaluate the critical value of Γ for the transition, we will derive another condition that needs to be satisfied at the transition. First, consider the momentum conservation for ions across the shock structure starting from the fluid equation of motion in the steady state,

$$\frac{\partial}{\partial x}\left(\rho_i v_i^2 + \mathcal{P}_i\right) = -e n_i \nabla\phi \,, \tag{2.9}$$

where $\mathcal{P}_i$ is ion thermal pressure and $\rho_i = m_i n_i$. As we assume cold ions, the contribution of ion thermal pressure here is negligible. The potential term in Eq. (2.9) can be expressed using Boltzmann's relation $n_e = n_L \exp(e\phi/T_e)$ with a constant T_e. Then, the momentum

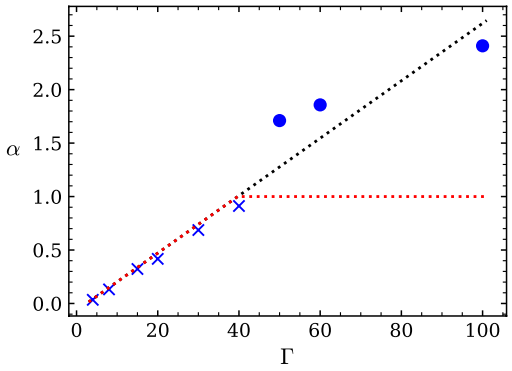

Figure 2.9: accelerated fraction $\alpha = n_a/n_L$ obtained from the simulations with respective Γ and $\Theta = 1$. We derive α from tracking the reflection rate for collisionless shock cases (blue crosses), while α for double-layer (blue dots) is obtained by the outflow density n_α [see Fig. 2.5(a)]. Black dot line is the extension of collisionless shocks' accelerated fraction which is used with Eq. (2.12) to derive v_s in Fig. 2.4(a). The reflection rate is denoted by the red dot line.

conservation can be expressed approximately as

$$\frac{\partial}{\partial x}\left(\rho_i v_i^2 + n_i T_e\right) \approx 0 \,. \tag{2.10}$$

At the transition, we can assume $v_p = v_s$ which means all ions are reflected without going to the downstream region. The reflected ions will have the velocity v_s in the shock frame and the same density as the incoming ions, n_L. Then the jump condition for the transition case with the above conditions gives us the following relation

$$M_s = \sqrt{\frac{\Gamma' - 2}{2}} \,. \tag{2.11}$$

With the help of Eqs. (2.7) and (2.8), the right-hand side of Eq. (8) is given as a function of Γ, which is shown in Fig. 2.6. The crossing point of the critical Mach number $M_{\rm cr}$ and M_s indicates the maximum value of Γ for existing collisionless shock. This critical value of $\Gamma \approx 40$ is consistent with our PIC simulation result depicted in Fig. 2.4.

2.3.4 Prediction of the Mach numbers

In hydrodynamic shocks, if the downstream velocity and the density jump have already known, the shock Mach numbers can be obtained by the mass conservation law of the jumps conditions. However, it is not that straightforward for collisionless shocks and double-layer structures. In order to derive the conservation, factors such as reflected ions in the strong shocks and the reversed flow in double-layer structures need to be taken into account.

Let's define $\alpha \equiv n_a/n_L$ as the accelerated fraction, where n_a is the density of particles accelerated by the electric field at the expansion front (either collisionless shock or double-layer) to twice the front velocity (Figs. 2.5). In the case of collisionless electrostatic shocks, n_α represents the density of reflected ions [dashed line in Fig. 2.5(b)], and α can be regarded as the reflection rate of incoming ions. Mass conservation applies to the fraction of ions passing to the shock downstream without being reflected $(1-\alpha)n_L$ (solid line in the Fig. 2.5(b)), hence, can be written as

$$n_p(v_s - v_p) = (1-\alpha)n_L v_s \ . \tag{2.12}$$

In the double-layer regime, n_α is a sum of two components: the reflected ions [dashed line in Fig. 2.5(a)] and the transmitted ion moving to the low density slab [Fig. 2.5(b)]. Since almost all upstream ions are reflected, we have $\alpha = (1 + n_T/n_L)$ with n_T as the transmitted ion density. As the transmitted flow connects two plasma regions, mass conservation should be derived based on this component. Thus, we get the relation $n_p(v_p - v_s) = n_T v_s$. Using the definition $n_T = (\alpha - 1)n_L$, we retrieve the same expression as Eq. (2.12).

Ions reflected from the shock with twice its velocity $2v_s$ are the reason we can have the same relation for both collisionless shocks and double-layer structures. The validity of Eq. (2.12) for double-layers strongly depends on the stability of the upstream structure. For instance, in large Γ cases, the velocity of the reflected and reversed flow fraction increase to exceed $2v_s$ [Fig. 2.3(e) and (f) for $\Gamma = 100$] so we expect to see discrepancies between prediction values and simulation results.

We can predict the shock Mach numbers from Eq. (2.12) from the initial condition (the density ratio Γ) if we knew the accelerated fraction α. However, there is no analytical model allowing us to obtain the accelerated fraction α at this moment. For a semi-analytical prediction of shock Mach numbers, we can use the results of α from PIC simulations which are indicated in Fig. 2.9. The values of α for the collisionless shock regime ($\alpha \leq 1$) are obtained from tracking the reflection ratio and indicated by the blue crosses in Fig. 2.9. For the double-layer regime ($\alpha \geq 1$), the values are illustrated in the blue dots by comparing the transmitted fraction n_T and n_L. Although we can have a unified definition of α, we can recognize the results in the two regimes are loosely related and we can see each of them scaled somewhat differently from Fig. 2.9. Additionally, it is easy to see that α increases linearly with respect to Γ. In this work, we applied the linear fitting of α but only for $\alpha < 1$ or the shock regime (black solid line in Fig. 2.9) for later prediction of shock Mach numbers. The justification is that for $\alpha > 1$ or the double-layer regime, the validity of Eq. (2.12) is marginal because of the increase in velocity of accelerated fraction as discussed above. The predicted shock Mach number shown as the black solid line Fig. 2.4(a) is consistent with PIC simulations (red circles) proving that

our approximation for α is indeed a reasonable choice.

2.4 Discussion

The condition to obtain the critical Mach numbers, $\varphi = M_{cr}^2/2$, implies that the downstream velocity in the shock frame $v_p = v_s$ which also means $\alpha = 1$ or a perfect reflection [Eq. (2.12)]. We observed that α increases as v_p increases but v_p obtained from two static slabs (without any initial relative velocity between them) is limited by the initial density jump Γ. However, previous works showed that for a given Γ, we can increase v_p and the reflection rate by adding initial colliding drift $v_{\rm init}$ between two plasma slabs Sorasio et al. (2006); Fiuza et al. (2013). Fiuza et al. Fiuza et al. (2013) also define M_{cr} as Mach numbers when ion reflection is observed as a consequence of increasing $v_{\rm init}$. However, a more consistent model should not only see ion reflection at M_{cr} but a perfect reflection $\alpha \approx 1$ due to the implication of M_{cr} mentioned above. An example of the argument is indicated in Fig. 2.10 for $\Gamma = 8$. It is clear that increasing the initial velocity $v_{\rm init}$ leads to a larger shock Mach number and accelerated fraction α (also reflection fraction in this context). The trend continues until shock Mach numbers approach the critical value and $\alpha \approx 1$ ($v_{init} = 2.5\ c_s$). For $v_{init} > 2.5\ c_s$, the flow becomes too fast for the shock formation and the shock structure saturated into weakly perturbed flows. We can still numerically derive α by its definition which becomes greater than 1. For instance, $\alpha \approx 6.3$ with $v_{init} = 3.5\ c_s$ and the structure is no longer collisionless shock in this case.

Further research is needed to shed insights into the transition from collisionless shock to double-layer. For now, let us briefly mention one possible interpretation of the transition based on the macro-view of shocks as a means of dissipating energy for material

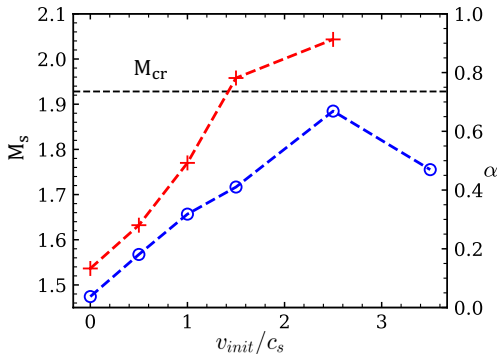

Figure 2.10: Shock Mach numbers (blue circles) and accelerated fraction α (red crosses) when adding initial velocity v_{init} for the case of $\Gamma = 8$, $\Theta = 1$ and $T_e = 10$ keV. The critical Mach number (black dashed line) is approximately 1.92 in this case. We can see that when M_s reach the critical value, $\alpha \approx 1$ as predicted from the critical condition $\varphi = M_{cr}^2/2$ and the definition of α. Shock structures start to saturate with $v_{init} > 2.5\ c_s$. At $v_{init} = 3.5\ c_s$, we have $\alpha \approx 6.3$ and it is no longer a collisionless shock structure.

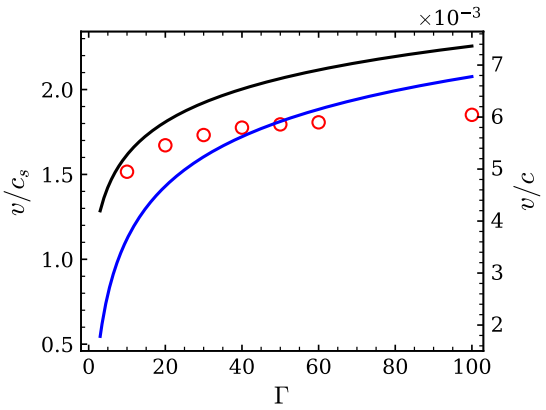

Figure 2.11: Comparison of the shock velocity between collisionless shock (red crosses) and collisional shock Mach numbers (black solid line) calculated from Eq. (2.12) with $\alpha = 0$ (no reflection). As a reference, v_p is also shown by the blue solid line. It is clear that, unlike collisionless shocks, v_s is always greater than v_p for collisional shocks, implying that there is no transition to double-layer structures.

crossing the shocks. From this perspective, the reversed flow could be seen as a mechanism for the shocks to release excessive energy created from the input power (initial density ratios Γ). In fact, this argument can be seen from our simulations with increasing Γ. For small input power, the shocks only dissipate their energy by accelerating upstream particles to downstream velocity (in laboratory frame). When the density ratios increase ($\Gamma \sim 10 - 40$) and exceed the limit provided by the previous method, the shock simply rejects the injections of energy by reflecting ions back to the upstream region Balogh & Treumann (2013b). Finally, when all the upstream ions are reflected ($\Gamma \gtrsim 40$), the ions from the high density plasma have to emit their own energy, hence the reversed flow appears.

The reflection of upstream particles is the special feature that distinguishes collisional and collisionless shocks. Given that the collision rate is always sufficient to dissipate energy for the shock, we can see that increasing the input power simply increases the shock velocity, with no reflections. To prove this point, we can calculate the collisional shock velocity by using Eq. (2.12) with $\alpha = 0$ as there is no reflection (v_p is similar to the values of collisionless shock). As shown in Fig. 2.11, the collisional shock velocity is always larger than v_p, implying no transition to double-layer structures.

2.5 Summary

In summary, we have studied the transition of the well-established collisionless shock to the double-layer structure. By using 1D PIC simulations, we prove that double-layer structures can emerge under the same two-slab plasma configurations which often use to study electrostatic shock formations. We found the transition occurs around $\Gamma = 40$

and is independent of the initial temperature ratio Θ. We then discussed the differences between the two structures and the ideas of how such a transition can happen.

In the second part, we proposed a new model for the critical Mach number based on previous works Sorasio et al. (2006); Fiuza et al. (2013). The main feature of our model is the incorporation of the density expansion that reduces the actual density ratios at the front. In particular, we use of the realistic density ratio at the front Γ' instead of the initial density ratio Γ for a more consistent description of the shock structure. The new model offers a promising result as it addresses previous discrepancies between the critical Mach number and the Mach number observed in simulations. In addition, our model can predict the critical value of Γ for the transition from collisionless shock to double-layer consistently with the numerical results.

Finally, we introduce a new concept of α with the motivation to include the ion reflection into the shock jump condition. The concept can also provide a consistent description of the front velocity from collisionless shock to double-layer cases.

Chapter 3

Shocks in Black Hole Coronae: Shock Structure and Proton Acceleration

---

3.1 Introduction

The central goal of this chapter is to determine, from first principles, whether collisionless shocks in supermassive black hole (SMBH) coronae can accelerate ions rapidly and efficiently enough to account for the hadronic component implied by recent multi-messenger observations of nearby radio-quiet AGNs. In particular, the neutrino luminosity inferred for sources such as NGC 1068 motivates scenarios in which the production region is compact and gamma-ray opaque, so that TeV–PeV neutrinos escape while the accompanying GeV–TeV gamma rays are attenuated by intense X-ray radiation fields. A hot, magnetized corona—the same plasma responsible for Comptonized X-ray emission—is therefore a natural candidate environment. The major uncertainty, however, is not whether the corona contains energetic particles, but whether it can *produce* them: the dominant acceleration mechanism under realistic coronal conditions remains unsettled, and the efficiency of diffusive shock acceleration (DSA) in the relevant regime has not been established with first-principles constraints.

From the plasma-physics perspective, SMBH coronae occupy a parameter space that is both astrophysically motivated and kinetically nontrivial. The corona is collisionless, trans-relativistic, and plausibly two-temperature ($T_i \neq T_e$), with electrons constrained by X-ray spectral cutoffs while ions may be substantially hotter due to weak Coulomb coupling. Shocks expected from infalling material, failed winds, or cloud fallback are likely quasi-parallel and magnetized, yet they may have *low* sonic Mach numbers (M_s of order a few) even when the Alfvénic Mach number is moderate. This combination is precisely where extrapolations from classical, high-M_s astrophysical shocks become unreliable. Low-M_s shocks are often assumed to be inefficient particle accelerators, but that assumption is based on limited kinetic coverage of the trans-relativistic, two-temperature regime relevant to coronae, and on an incomplete understanding of how self-generated

turbulence develops in response to shock-reflected ions.

The questions addressed in this chapter are therefore intentionally concrete: (i) what shock structure develops in coronal-like plasmas once ion reflection, upstream streaming instabilities, and magnetic amplification are treated self-consistently; (ii) whether ions undergo sustained DSA, and if so, what acceleration rate is realized in units that can be extrapolated to coronal scales; and (iii) how robust the ion acceleration efficiency and ion–electron energy partition are when the upstream conditions vary across the plausible coronal range in M_s, M_A, $v_{\rm sh}$, and T_i/T_e. Answering these questions requires a kinetic approach. While fluid or hybrid models can capture some aspects of the dynamics, the injection process, the development of microphysical turbulence, and the diffusion properties that control the DSA rate are inherently collisionless and species dependent. We therefore employ particle-in-cell (PIC) simulations to resolve ion and electron dynamics simultaneously.

This chapter is organized to connect coronal conditions to measurable acceleration outcomes. In Section 3.2, we translate observationally motivated corona models into the shock control parameters used in kinetic theory, emphasizing the expected ranges of M_s, M_A, trans-relativistic shock speeds, and the ion–electron temperature imbalance. In Section 3.3, we describe the simulation setup. We use large-scale 1D3V PIC simulations tailored to quasi-parallel geometry, preserving the dimensionless parameters that control shock microphysics while adopting a reduced mass ratio for computational feasibility. We also define the diagnostics used throughout the chapter: how the shock position is identified, how downstream spectra are measured, how thermal and non-thermal components are separated, and how we quantify both the maximum-energy growth and the energy partition between ions and electrons.

We then present a fiducial run that serves as a reference point for the remainder of the study. Section 3.4.1 characterizes the quasi-steady shock structure, highlighting the role of shock-reflected ions in driving upstream turbulence and magnetic amplification. Section 3.4.2 connects these fields to particle spectra and representative acceleration histories, providing a unified picture of injection and DSA cycles for ions and electrons in the coronal regime. Section 3.4.3 identifies the dominant upstream streaming mode and clarifies when resonant versus non-resonant behavior is expected across our parameter space.

With this foundation, Section 3.5 quantifies the proton acceleration rate and its scaling. We measure the late-time, approximately linear energy growth characteristic of DSA and extract a normalized acceleration coefficient that can be compared across simulations and mapped to physical units via $\Omega_{\rm ci}$ and $\beta_{\rm sh}$. This section focuses on how the acceleration timescale responds to changes in T_i/T_e, M_s, M_A, and $v_{\rm sh}$, isolating which parameters matter most for reaching the parent energies required for neutrino production.

Finally, Section 3.6 addresses the energy budget: how much of the shock-dissipated en-

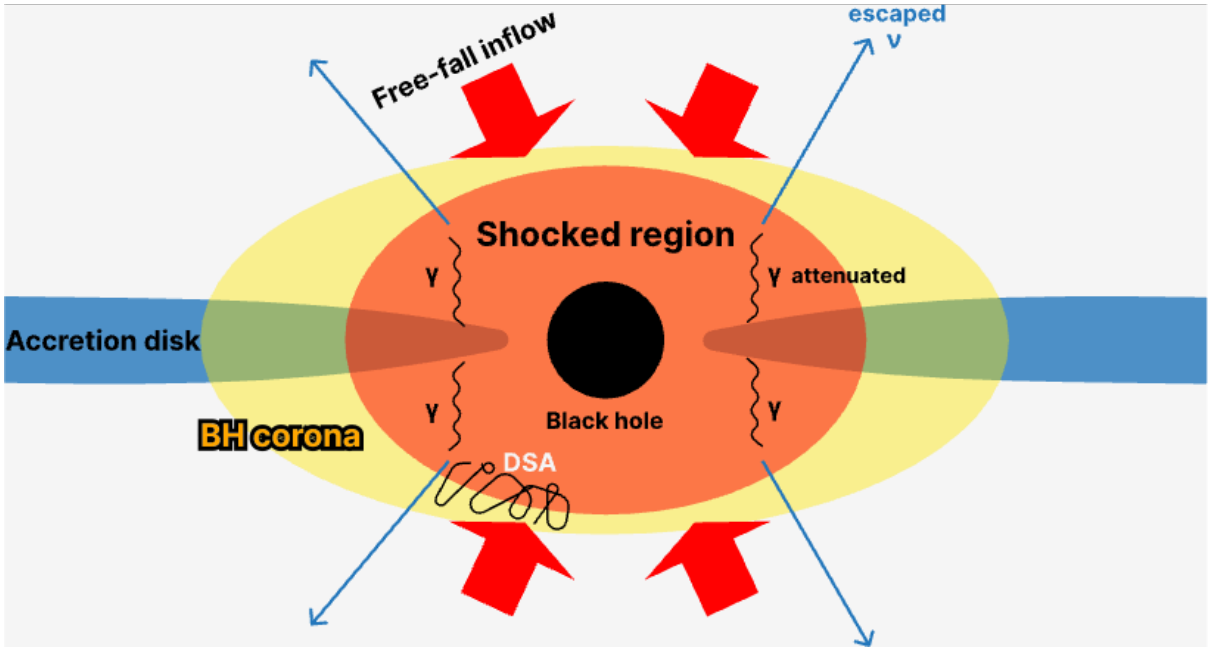

Figure 3.1: Schematic illustration of an accretion shock formed by the infalling flow in the hot BH corona. Protons are accelerated to high energies and produce high-energy neutrinos through hadronic pp and $p\gamma$ interactions. Neutrinos can escape from the system and be observed by IceCube, while the accompanying gamma-rays will be attenuated by X-ray photons.

ergy is transferred into non-thermal ions versus electrons, and how this partition changes with upstream conditions. This is essential for interpreting coronae as multi-messenger sources, because efficient ion acceleration supports hadronic neutrino production while suppressed electron acceleration limits competing leptonic emission. We emphasize the regimes most relevant to BH coronae—in particular, high T_i/T_e and trans-relativistic speeds—and highlight the trends that will be used in later chapters when assessing the implications for neutrino production in radio-quiet AGNs.

3.2 Shock conditions in BH coronae

We consider the corona of a supermassive black hole of mass $M_{\rm BH}$ as a hot, collisionless plasma region extending to $R_c \lesssim 100\,R_g$, where $R_g = GM_{\rm BH}/c^2$ is the gravitational radius. We adopt a scenario in which shocks form within the BH corona (see Figure 3.1). Such shocks can naturally arise from infalling material associated with the accretion flow or from failed winds (Inoue et al., 2019, 2020, 2024a). Shocks may also be triggered by material falling in from larger radii, for example from broad-line region clouds (Müller & Romero, 2020; Müller et al., 2022; Sotomayor & Romero, 2022). In the latter case, the fallback flow is likely much colder than the BH corona; we refer to this as the cold inflow scenario.

Kinetic studies of shock-accelerated particles in collisionless plasmas have identified the shock sonic and Alfvénic Mach numbers, M_s and M_A, as the primary parameters determining particle acceleration characteristics. In this section, we derive these parameters based on conditions typical of BH coronae. Our goal is to establish a fiducial range for the shock parameters consistent with multi-messenger observations, providing a physical basis for modeling shock-driven proton acceleration and subsequent neutrino production. We treat ions as protons, which constitute the majority of baryonic matter. For the first part of this thesis in Chapter 3 and 4, we assume the plasma is primarily an ion-electron mixture where the positron fraction is negligible.

For our fiducial model, we assume the shock velocity, $v_{\rm sh}$, is on the order of the free-fall velocity of infalling material, $v_{\rm ff} = \sqrt{2GM_{\rm BH}/R_c}$. This yields the following scaling for shock speed:

$$\frac{v_{\rm sh}}{c} \simeq 0.14 \left(\frac{r_c}{100}\right)^{-1/2} , \tag{3.1}$$

where $r_c = R_c/R_g$ is the coronal radius in units of the gravitational radius.

The sonic Mach number $M_s = v_{\rm sh}/c_s$ depends on the plasma sound speed, $c_s = \sqrt{\gamma_{\rm ad}(T_i + T_e)/m_i}$, where T_i and T_e denote the ion (proton) and electron temperatures, respectively, and $m_i = m_p$ is the proton rest mass. We adopt an adiabatic index of $\gamma_{\rm ad} = 5/3$. While the electron temperature is constrained by the cutoff energy of the X-ray spectrum to $T_e \sim 100$ keV (e.g., Fabian et al., 2015; Laha et al., 2025), the ion temperature is poorly constrained by observations. In hot BH coronae, inefficient Coulomb coupling allows ions to become significantly hotter than electrons ($T_i \gg T_e$). A common assumption of $T_i \sim 10\,T_e \sim 1$ MeV leads to

$$M_s = \frac{v_{\rm sh}}{c_s} \simeq 3.4 \left(\frac{r_c}{100}\right)^{-1/2} \left(\frac{T_i}{1\,{\rm MeV}}\right)^{-1/2} . \tag{3.2}$$

Alternatively, a more physically motivated estimate for T_i comes from ADAF models, which predict $T_i \simeq GM_{\rm BH}m_i/(6R_c) \sim 1.6(r_c/100)^{-1}$ MeV (Yuan & Narayan, 2014; Inoue et al., 2024b). This temperature profile yields a slightly lower Mach number of $M_s \simeq 2.7$, independent of other parameters. Based on these estimates, shocks in the BH corona are likely to possess low sonic Mach numbers, although higher values (up to a few tens) could be realized in the cold inflow picture.

The Alfvénic Mach number, $M_A = v_{\rm sh}/v_A$, depends on the Alfvén speed, $v_A = B_0/\sqrt{4\pi n_0 m_i}$, which requires estimates for the upstream plasma density n_0 and magnetic field B_0. We estimate the electron density $n_e = n_0$ from the Thomson optical depth, $\tau_T = n_e\sigma_T R_c \sim 1$ (Inoue et al., 2019; Padovani et al., 2024). The coronal magnetic field B_0 remains a significant source of uncertainty. Millimeter emission from electron synchrotron radiation has been suggested as a method to estimate B_0, constraining it to $B_0 \sim O(10 - 100$ G) (Inoue & Doi, 2018; del Palacio et al., 2025). For example, the

value estimated for NGC 1068 is $B_0 \simeq 150$ G (Mutie et al., 2025; del Palacio et al., 2025). Hence, we adopt $B_0 = 100$ G as the fiducial value for this study. The Alfvén speed and the Alfvénic Mach number are then given by

$$\frac{v_A}{c} \simeq 7.2 \times 10^{-3} \left(\frac{r_c}{100}\right)^{1/2} \left(\frac{M_{\rm BH}/M_\odot}{10^7}\right)^{1/2} \left(\frac{B_0}{100\,{\rm G}}\right) , \tag{3.3}$$

$$M_A = \frac{v_{\rm sh}}{v_A} \simeq 20 \left(\frac{r_c}{100}\right)^{-1} \left(\frac{M_{\rm BH}/M_\odot}{10^7}\right)^{-1/2} \left(\frac{B_0}{100\,{\rm G}}\right)^{-1} . \tag{3.4}$$

It is worth noting that the estimate of magnetic field strength is still under debate. Other acceleration models, such as SA or reconnection models, require stronger fields ($B \gg 10^3$ G, see e.g., Murase, 2022; Das et al., 2024; Fiorillo et al., 2024b).

In summary, our theoretical estimates suggest that shocks in the coronae of RQ AGNs are likely to be trans-relativistic ($v_{\rm sh}/c \sim 0.3$), with low sonic Mach numbers ($M_s \sim 2-10$) and moderate Alfvén Mach numbers ($M_A \sim 30$). These values are subject to considerable uncertainty; hence, we aim to systematically survey shocks across a wide range of parameters (see details in Table 3.1). We focus on effects less explored in previous collisionless shock studies, such as the trans-relativistic shock regime ($v_{\rm sh}/c \sim 0.3$) and the initial ion-to-electron temperature imbalance (T_i/T_e).

3.3 Numerical setup

To provide a first-principles, self-consistent description of particle acceleration under the physical conditions of BH coronae, we employ the PIC method. A series of large-scale 1D3V PIC simulations is performed using the code SMILEI (Derouillat et al., 2018) to survey the parameter space.

We initialize a uniform plasma with density $n_i = n_e$ occupying the region $x > 0$. The plasma is initialized with a velocity $-v_{\rm pt}$ drifting toward a reflective boundary at $x = 0$, where the incoming and reflected plasmas interact to launch a shock in the $+x$ direction. In this setup, the simulation frame coincides with the downstream rest frame of the shock, similar to previous studies (Park et al., 2015; Shalaby, 2024). Introducing the shock compression ratio $\mathcal{R}$, the shock velocity in the upstream rest frame is given by $v_{\rm sh} = v_{\rm pt}\mathcal{R}/(\mathcal{R}-1)$. For a strong shock with $\mathcal{R} \approx 4$, this expression reduces to $v_{\rm sh} \simeq 4v_{\rm pt}/3$.

The magnetic field is initialized in the $x-y$ plane as $\boldsymbol{B} = B_x\hat{\boldsymbol{x}} + B_y\hat{\boldsymbol{y}}$, where $B_x = B_0\cos\theta_B$, $B_y = B_0\sin\theta_B$, and B_0 denotes the field strength. In this study, we focus on quasi-parallel shocks with a fixed magnetic obliquity $\theta_B = 30°$.

Simulation parameters are summarized in Table 3.1. Electrons and protons are initialized with the relativistic Maxwell-Jüttner distribution of T_e and T_i, respectively. We

Table 3.1: Simulation Parameter Survey

Run ID	$v_{\rm sh}/c$	M_s	M_A	T_i/T_e	$T_e/(m_i c^2)$	$T_i/(m_i c^2)$	**Purpose**
T10 (Ref)	0.33	8	26	10	9.281×10^{-5}	9.281×10^{-4}	Reference Case
T1	0.33	8	26	1	5.105×10^{-4}	5.105×10^{-4}	Different temperature ratios (T_i/T_e)
T50	0.33	8	26	50	2.002×10^{-5}	1.001×10^{-3}	
T0.01	0.33	8	26	0.01	1.011×10^{-3}	1.011×10^{-5}	
S4T1	0.33	4	26	1	2.042×10^{-3}	2.042×10^{-3}	Different temperature ratios with $M_s = 4$
S4T10	0.33	4	26	10	3.713×10^{-4}	3.713×10^{-3}	
S4T50	0.33	4	26	50	8.007×10^{-5}	4.004×10^{-3}	
S2T1	0.33	2	26	1	8.168×10^{-3}	8.168×10^{-3}	Different temperature ratios with $M_s = 2$
S2T10	0.33	2	26	10	1.485×10^{-3}	1.485×10^{-2}	
S20T1	0.33	20	26	1	8.168×10^{-5}	8.168×10^{-5}	Higher M_s with $T_i = T_e$
S30T0.01	0.33	30	26	0.01	7.188×10^{-5}	7.188×10^{-7}	Higher M_s with hotter electrons
A4	0.33	8	4	10	9.281×10^{-5}	9.281×10^{-4}	Different Alfvén Mach numbers (M_A)
A8	0.33	8	8	10	9.281×10^{-5}	9.281×10^{-4}	
A46	0.33	8	46	10	9.281×10^{-5}	9.281×10^{-4}	
V0.125	0.167	8	26	10	2.377×10^{-5}	2.377×10^{-4}	Different shock velocities ($v_{\rm sh}$)
V0.5	0.66	8	26	10	3.713×10^{-4}	3.713×10^{-3}	

use a reduced ion-to-electron mass ratio of $m_R = m_i/m_e = 100$ to make the simulations computationally feasible, while remaining large enough to maintain standard scale separation between ions and electrons. Accordingly, the physical parameters (T_i, T_e, B_0) are scaled to preserve the key dimensionless parameters $(M_s, M_A, T_i/T_e)$ and retain the characteristics of shock plasma physics. Note that even if the Mach number is held constant, T_i and T_e can vary significantly depending on the temperature ratio T_i/T_e (see Table 3.1).

We resolve most simulations with a spatial resolution of $\Delta x = 0.1\ d_e$ and temporal resolution $\Delta t = 0.04\ \omega_{\rm pe}^{-1}$, where $\omega_{\rm pe} = \sqrt{4\pi n_0 e^2/m_e}$ and $d_e = c/\omega_{\rm pe}$ are the upstream plasma frequency and electron inertial length, respectively. The only exception is run A4, where we adopt $\Delta x = 0.025\ d_e$ and $\Delta t = 0.02\ \omega_{\rm pe}^{-1}$ to resolve the electron Larmor radius $\rho_e = m_e v_{\rm pt} c/(eB_0) \simeq 0.3\ d_e$ and ensure energy conservation. In the simulations, we use 150 particles per cell per species. For the analysis of shock structure and ion acceleration, it is convenient to express time in units of the ion gyrofrequency, $\Omega_{\rm ci} = eB_0/(m_i c)$ (Sections 3.4.1 and 3.5). We therefore convert all times to this normalization using:

$$\Omega_{\rm ci} = \omega_{\rm pe} \frac{v_{\rm sh}/c}{M_A \sqrt{m_R}}\,. \tag{3.5}$$

All simulations are evolved for at least $t_{\rm end} \gtrsim 400\,\Omega_{\rm ci}^{-1}$, ensuring that the relevant electromagnetic instabilities reach saturation and that a well-developed non-thermal power-law tail emerges in the particle distribution. We use a sufficiently large simulation box size L_x so that reflected particles and those undergoing acceleration remain within the receding plasma for the entire duration up to $t_{\rm end}$. The domain size is $L_x = 180224\ d_e$ for our typical case, with the largest case (run V0.5) reaching $L_x = 294912\ d_e$.

3.4 Fiducial run: shock characteristics and particle acceleration

First, we examine the results of our reference simulation (run T10), in which the plasma parameters are chosen as $M_s = 8$, $M_A = 26$, $v_{\rm pt}/c = 0.25$, and $T_i/T_e = 10$.

3.4.1 Shock structure

Figure 3.2 displays a snapshot from the reference simulation (run T10) in a quasi-steady evolution stage at $t \approx 256\ \Omega_{\rm ci}^{-1}$ ($t = 2 \times 10^5\ \omega_{\rm pe}^{-1}$). The shock front is located at $x_{\rm sh} \approx 16000\ d_e$ [vertical red dashed line in Figure 3.2(c)], marking the boundary between the upstream (unshocked) and downstream (shocked) regions. The ion density shows a strong compression across the shock, reaching more than four times the upstream density on average ($\mathcal{R} \gtrsim 4$), which signals the formation of a strong shock based on the Rankine-Hugoniot jump conditions. We define $x_{\rm sh}$ throughout this study as the position of the

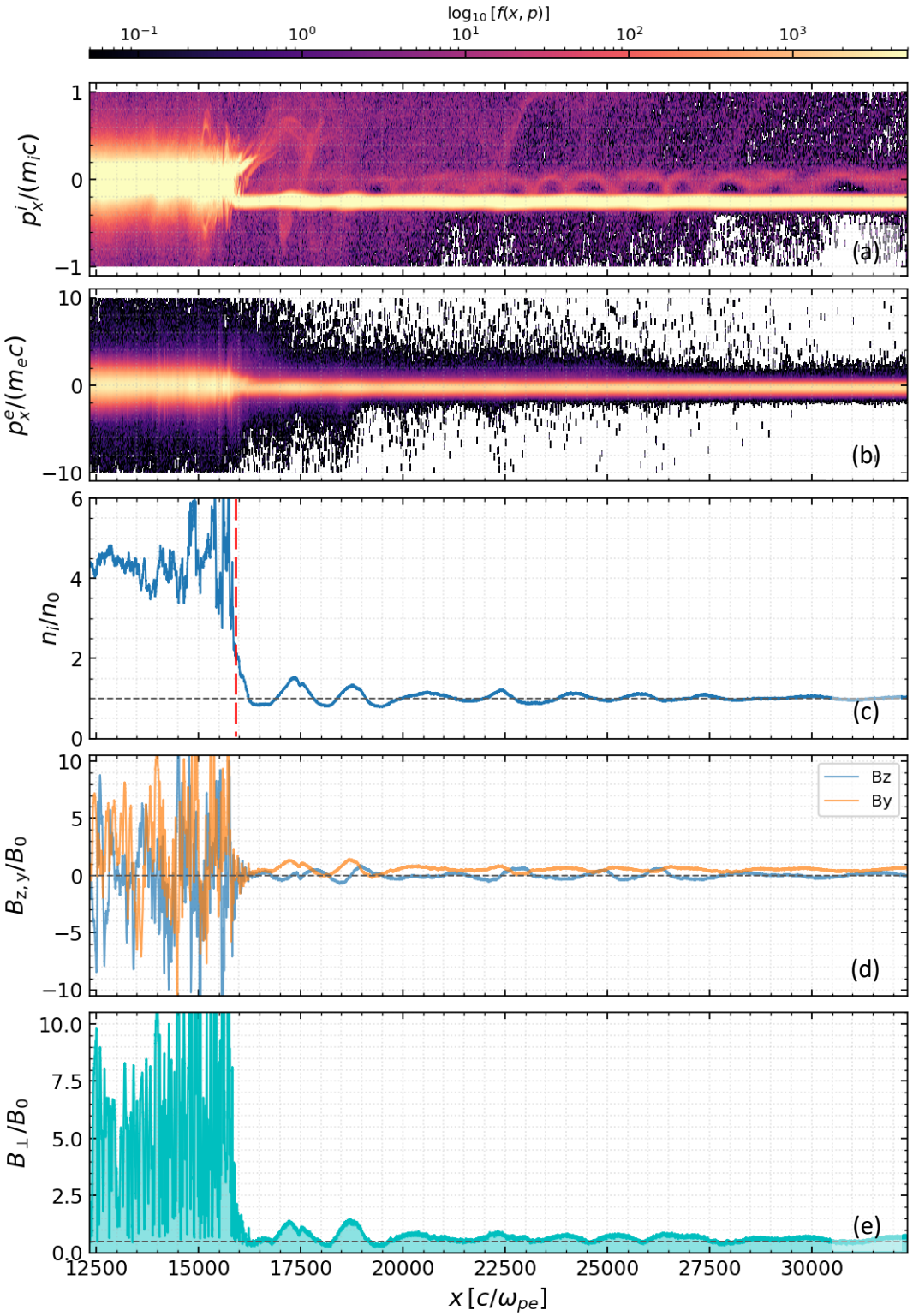

Figure 3.2: Snapshot of shock structures in the fiducial model (run T10) at $t \approx 256\ \Omega_{\rm ci}^{-1}$. (a, b) The position-momentum ($x - p_x$) phase space distributions for ions and electrons. (c) Ion density profile, with the shock position ($x_{\rm sh}$) marked by the red dashed line. (d, e) The transverse magnetic field components (B_y, B_z) and the total transverse amplitude ($B_\perp$), showing significant amplification over the initial value [black dashed line in (e)].

sharp ion density ramp; $x \leq x_{\rm sh}$ refers to the downstream and $x \geq x_{\rm sh}$ to the upstream region.

Figures 3.2(a) and (b) show the $x - p_x$ phase space distribution of ions and electrons, respectively. The ion phase space [Figure 3.2(a)] provides direct evidence for ion acceleration, showing an energetic back-streaming population of ions comprising both shock-reflected and accelerated populations, moving away from the shock into the upstream region. This streaming ion population excites magnetic fluctuation modes in the upstream [see Figure 3.2(e)], providing the necessary scattering environment for electrons and ions to complete the multiple shock-crossing cycles characteristic of the DSA process. In addition, the back-streaming ions generate a net current, which induces a compensating return current in the background electrons. As shown in the electron phase space [Figure 3.2(b)], this interaction leads to significant electron preheating in the upstream region near the shock front ($x_{\rm sh} < x \lesssim 2.5 \times 10^4\, d_e$). This preheating process has recently been shown to play a crucial role in subsequent electron acceleration in quasi-parallel collisionless shocks (Gupta et al., 2024a, 2025).

The transverse magnetic field components, B_y and B_z, are shown in Figure 3.2(d), while their combined magnitude, $B_\perp = \sqrt{B_y^2 + B_z^2}$, is presented in Figure 3.2(e). The transverse magnetic amplitude $B_\perp$ is amplified by a factor of ~ 2 relative to its initial upstream value. As discussed above, this amplification and the associated fluctuations originate from the interaction between the back-streaming ions and the upstream plasma.

3.4.2 Particle spectrum and acceleration trajectory

To illustrate how energy is partitioned between species, each spectrum is plotted as $(\gamma - 1)f(\gamma)$ against the kinetic energy $K = (\gamma - 1)\mu$, where $\mu = m_{i,e}/m_i$ denotes the normalized particle mass. The upper panel (a) of Figure 3.3 shows the temporal evolution of the ion and electron energy spectra in the downstream region of the shock, spanning $x_{\rm sh} - 6500\ d_e < x < x_{\rm sh} - 1500\ d_e$. Unless stated otherwise, this spatial range is adopted for all analyses of the downstream particle spectra. The color gradient represents the simulation time in units of $t\Omega_{\rm ci}$, shared across all panels in Figure 3.3.

Both species exhibit clear power-law tails extending from their thermal populations, which can be fitted using a relativistic Maxwellian distribution,

$$f_{\rm MB}(\gamma) = \frac{\gamma\sqrt{\gamma^2 - 1}}{\Theta K_2(1/\Theta)} \exp\left(-\frac{\gamma}{\Theta}\right), \tag{3.6}$$

where $\Theta = T/(mc^2)$ is the dimensionless temperature and K_2 is the modified Bessel function of the second kind. The peak of the ion spectrum coincides with the kinetic energy of the incoming flow, $E_{\rm sh} = \frac{1}{2} m_i v_{\rm pt}^2$ [vertical black dash–dotted line in Figure 3.3(a)], indicating that the bulk of the injected energy is deposited into the thermal ions.

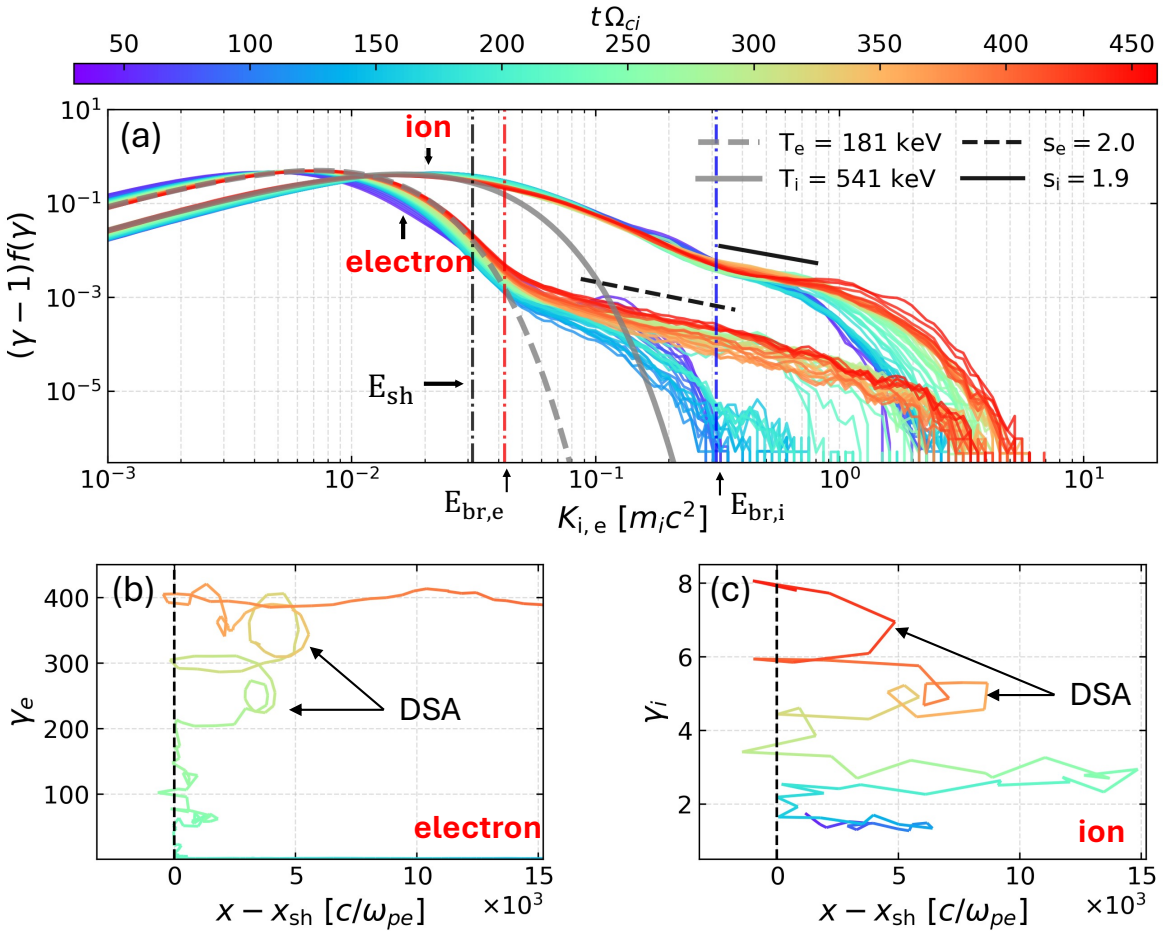

Figure 3.3: Signatures of particle acceleration, with the color scale indicating time in units of $t\Omega_{ci}$. (a) Evolution of the ion and electron energy spectra in the shock downstream. Both species exhibit two distinct components: a thermal bulk and a developing non-thermal power-law tail. (b, c) Trajectories of a typical accelerating electron and ion, illustrating the DSA process.

The break Lorentz factors γ_{br}, marking the separation point between thermal and non-thermal populations, are shown by red and blue dash–dotted lines for electrons and ions, respectively. While the electron spectra are well fitted by the Maxwellian distribution, the ion spectra exhibit a noticeable supra-thermal shoulder that resembles a shifted Maxwellian, likely arising from pre-acceleration processes at the shock front (Caprioli & Spitkovsky, 2014b; Park et al., 2012). Accordingly, based on the transition in particle spectra, we will universally use $\gamma_{br,e} = 10\,T_e^d/(m_ic^2)$ and $\gamma_{br,i} = 10\,E_{sh}/(m_ic^2)$ for all cases, where T_e^d denotes the electron downstream temperature. The non-thermal tails follow a power-law distribution, $f(K) \propto K^{-s}$, with spectral indices $s_i \approx s_e \simeq 2$, consistent with predictions from DSA theory for strong shocks. In general, ion spectra produced by DSA are hard, with $s_i \lesssim 2$ in most cases and reaching values as low as ~ 1.5. A power-law index $s = 1.5$ is expected in the non-relativistic energy regime, gradually steepening toward $s \sim 2$ in the relativistic limit (Haggerty & Caprioli, 2019). In contrast, the electron spec-

tral index varies significantly with shock parameters, becoming noticeably softer ($s \gtrsim 3$) for weaker shocks with $M_s \lesssim 8$ (e.g., runs S4T1, S4T10, and S4T50).

To illustrate the acceleration mechanism, we tracked representative electron and ion trajectories in x–γ space, as shown in panels (b) and (c) of Figure 3.3. Here, we normalized the particle positions relative to the shock front, whereas γ is computed in the simulation frame. The color of each trajectory corresponds to the simulation time and shares the same scale as the upper panel. The ion trajectory shows that the particle resides predominantly in the upstream region and undergoes repeated scattering between the upstream and downstream regions. The ion Lorentz factor γ increases each time the particle returns to the shock front after scattering off upstream fluctuations. This apparent "energy gain" occurs in the downstream frame; if transformed to the shock frame, the particle gains energy upon each shock crossing, as commonly described in DSA theory (see Figure 8 of Kato 2015).

The electron acceleration reveals a more complex, two-stage process. The accelerated electron first undergoes a rapid pre-acceleration phase close to the shock front, where its trajectory resembles a hybrid SDA, similar to that described in previous work (Park et al., 2015). Once it attains sufficient energy from this initial stage, it is injected into the main DSA cycle for further energization in a manner similar to ions. The significant mass difference between electrons and ions directly impacts their acceleration efficiency. Due to their much smaller gyroradii, electrons require more DSA cycles to achieve the same energy as ions. This lower efficiency results in a smaller non-thermal energy fraction for electrons compared to ions, as observed in the energy spectra shown in Figure 3.3(a).

3.4.3 Streaming instabilities

The nature of the instabilities driven by streaming ions depends primarily on the ion current density (Marcowith et al., 2021; Haggerty & Caprioli, 2019). In weak current regimes, the system is dominated by the resonant instability (RI), which is excited through a gyroresonant interaction between the streaming ions and Alfvénic fluctuations (Skilling, 1971). In contrast, at sufficiently high current densities, a strong neutralizing return current is carried by background electrons, exciting modes at shorter wavelengths. This leads to the non-resonant instability (NRI), also known as Bell's instability (Bell, 2004). Kinetic plasma studies provide a practical method for distinguishing between them based on wave polarization: the fastest growing NRI modes are predominantly right-handed (RH), whereas for RI, the left-handed (LH) component is expected to be of greater magnitude (Haggerty & Caprioli, 2019; Gupta et al., 2024b).

To study the source of the upstream magnetic turbulence in run T10, we performed a spatial Fourier analysis of the transverse magnetic field in the upstream region at $t \approx 130\ \Omega_{\rm ci}^{-1}$, as indicated by the two vertical black dashed lines in Figure 3.4(a). The

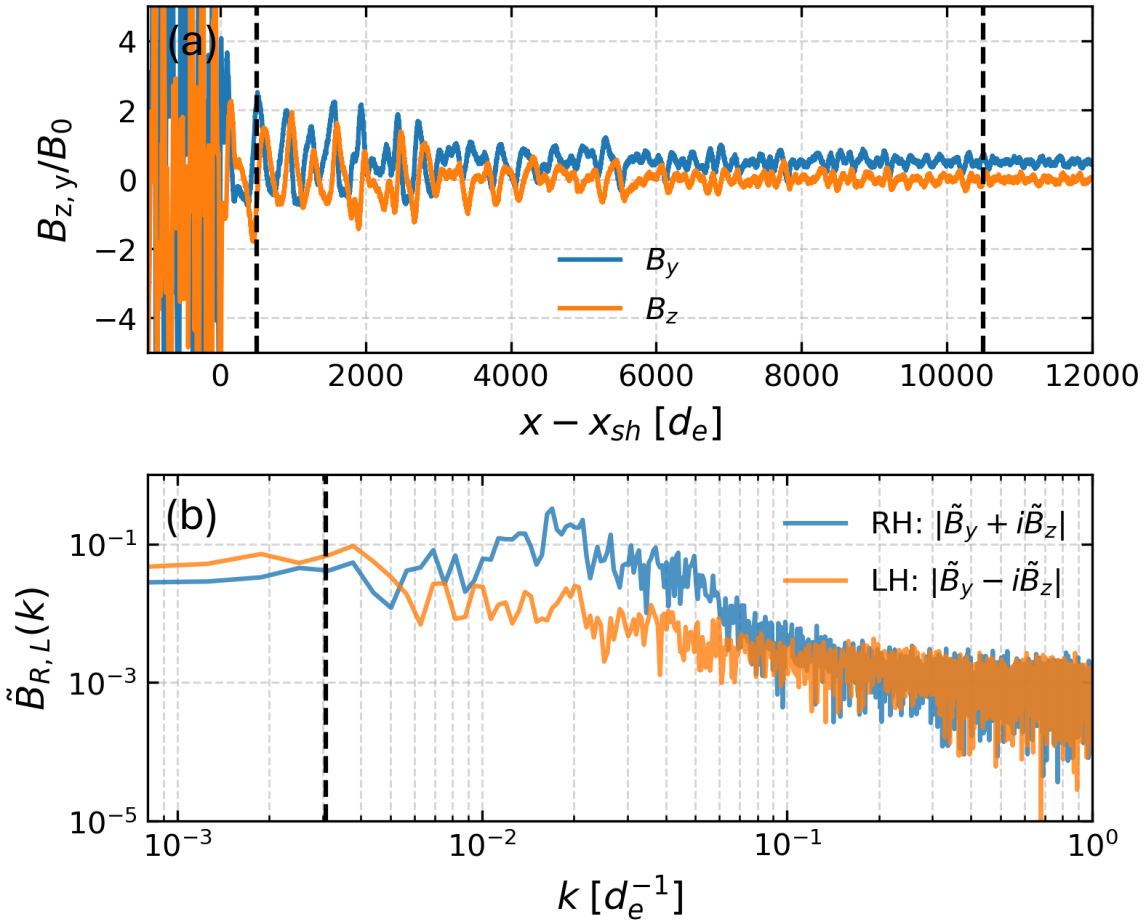

Figure 3.4: Spatial Fourier analysis of the upstream streaming instability at $t \approx 130\ \Omega_{\rm ci}^{-1}$, showing that the dominant mode is the right-hand non-resonant instability. (a) Transverse magnetic field profile in the upstream region selected for the spectral analysis, indicated by the two vertical black dashed lines. (b) Fourier power spectrum of the magnetic field, decomposed into right-hand (RH) and left-hand (LH) polarized modes. The vertical black dashed line marks the wavenumber of the mode resonant with back-streaming ions of mean gyroradius $\bar{\rho}_i$, $k_{\rm res} \sim 1/\bar{\rho}_i$.

corresponding magnetic amplitude spectra of the RH and LH polarized modes, defined respectively as $\tilde{B}_R = |\tilde{B}_y(k) + i\tilde{B}_z(k)|$ and $\tilde{B}_L = |\tilde{B}_y(k) - i\tilde{B}_z(k)|$, are shown in panel (b). Here $\tilde{B}_{y,z}$ are the spatial Fourier amplitudes in the transverse directions. The RH mode clearly dominates over the LH mode, exhibiting a significantly larger peak amplitude. The spectrum peaks at a wavenumber $k_{\rm max}$ larger than the wavenumber of the mode resonant with back-streaming ions, $k_{\rm res} \sim 1/\bar{\rho}_i$, indicated by the vertical black dashed line in Figure 3.4(b). Here, $\bar{\rho}_i$ is the mean gyroradius of the back-streaming ions, estimated using $v \approx 5v_{\rm sh}/4$, corresponding to the velocity of reflected particles in the downstream frame of a strong shock. This behavior is consistent with the expected characteristics of the NRI mode.

We performed a similar analysis for all simulation cases in the present study and found that almost all cases exhibit the NRI as the dominant mode. A few exceptions occur in

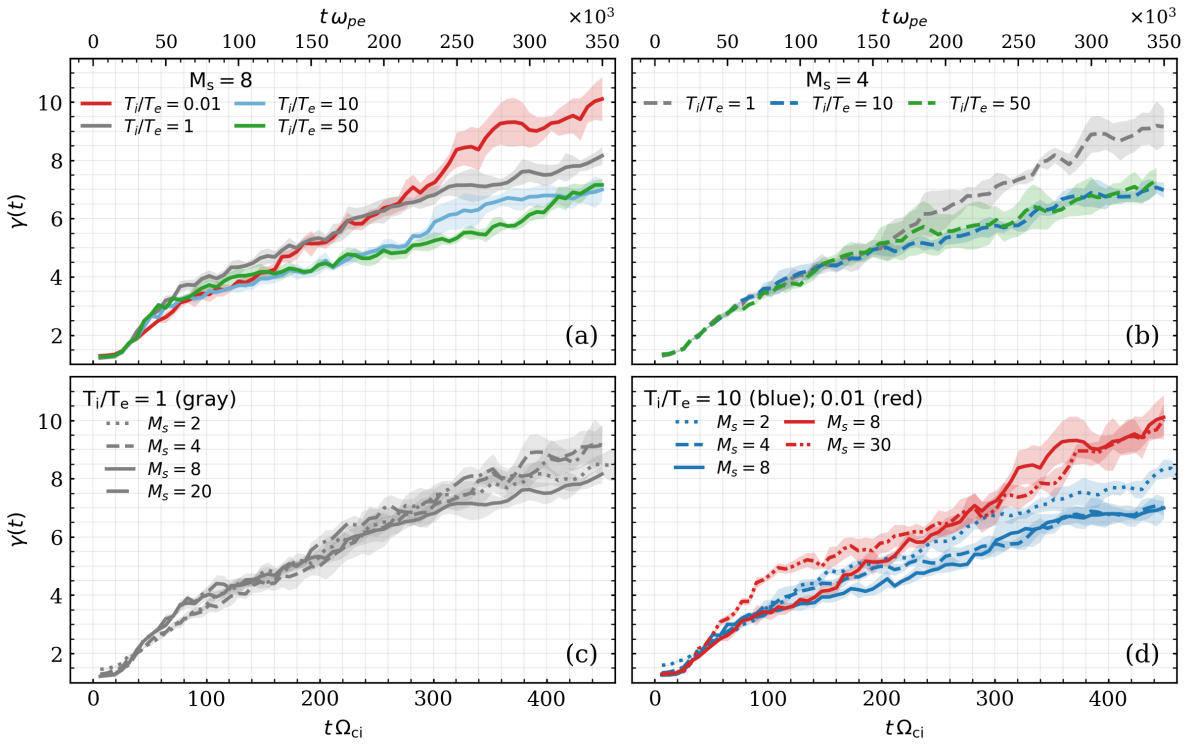

Figure 3.5: Time evolution of the mean Lorentz factor $\gamma(t)$ of the ten most energetic ions at each snapshot for different plasma conditions. The upper panels show the effect of varying the temperature ratio T_i/T_e at fixed M_s, while the lower panels show the effect of varying M_s at fixed T_i/T_e. Shaded regions represent one standard deviation. All other parameters are identical to the reference run (T10), unless otherwise noted. (a–b) Dependence on T_i/T_e for $M_s = 8$ and $M_s = 4$, respectively. (c) Dependence on M_s for $T_i/T_e = 1$. (d) Same as (c), but for both $T_i/T_e = 0.01$ (red lines) and $T_i/T_e = 10$ (blue lines).

the low-Alfvénic-Mach-number runs with $M_A = 4$ and 8 (runs A4 and A8). This trend is consistent with previous numerical studies of quasi-parallel collisionless shocks, which report that low-M_A shocks preferentially excite the RI (Caprioli & Spitkovsky, 2014a; Gupta et al., 2024b). Nevertheless, both types of instabilities are capable of generating sufficient upstream magnetic turbulence to sustain DSA of both ions and electrons.

3.5 Proton acceleration rate

We now extend our analysis to quantify the dependence of the proton energy gain, or acceleration rate, on various shock parameters. In particular, we discuss how the acceleration timescale evolves and the implications for potential neutrino emission from the corona.

3.5.1 Dependence on T_i/T_e and M_s

To illustrate how the maximum ion energy evolves over time, Figure 3.5 shows the time evolution of the average Lorentz factor $\gamma(t)$ of the ten most energetic protons at each snapshot. All cases in Figure 3.5 share the same initial drift velocity ($v_{\rm pt}/c = 0.25$) and magnetic field strength ($M_A = 26$). The top panels display the simulations with different T_i/T_e values at fixed Mach numbers: $M_s = 8$ in panel (a) and $M_s = 4$ in panel (b). The bottom panels compare cases with different M_s values while keeping T_i/T_e constant: $T_i/T_e = 1$ in panel (c), and $T_i/T_e = 10$ (blue lines) and $T_i/T_e = 0.01$ (red lines) in panel (d).

In all cases, the ion energy $\gamma(t)$ evolves in two distinct phases, separated around $t \sim 100\ \Omega_{\rm ci}^{-1}$. The early phase corresponds to the period required for the shock structure to reach a quasi-steady state and for upstream turbulence to fully develop. In the later stage ($t \gtrsim 100\ \Omega_{\rm ci}^{-1}$), the energy gain proceeds approximately linearly with time, $\gamma(t) \propto t$, consistent with the predictions of DSA theory (e.g. Drury, 1983; Blandford & Eichler, 1987b). Figures 3.5(a) and (b) show that increasing the temperature ratio T_i/T_e leads to a weak inverse correlation with the acceleration rate, roughly following $\gamma(t) \propto (T_i/T_e)^{-0.15}$. However, this dependence is weak even between the extreme cases of $T_i/T_e = 0.01$ and $T_i/T_e = 50$; at the end of the runs, $\gamma(t)$ differs by a factor $\lesssim 1.5$. The sonic Mach number M_s also appears to have minimal effect on the maximum ion energy, as shown in Figures 3.5(c) and (d), where cases with the same T_i/T_e (lines of the same color) converge to nearly identical values.

3.5.2 Dependence on M_A and $v_{\rm pt}$

We next examine the influence of the Alfvénic Mach number M_A and the injected particle velocity $v_{\rm pt}$. According to DSA theory, the acceleration timescale depends on the magnetic field strength and the shock velocity as $t(\gamma) \simeq D(\gamma)/v_{\rm sh}^2$, where the diffusion coefficient is approximately Bohm-like, $D(\gamma) \simeq cE_{\rm CR}/(eB)$ with $E_{\rm CR} \simeq \gamma m_i c^2$ (Drury, 1983; Blandford & Eichler, 1987b). This yields the scaling

$$t(\gamma) \approx \mathcal{C}\,\gamma\,\beta_{\rm sh}^{-2}\,\Omega_{\rm ci}^{-1}, \tag{3.7}$$

where $\beta_{\rm sh} = v_{\rm sh}/c$ and $\mathcal{C}$ represents a dimensionless coefficient encapsulating other factors governing the acceleration efficiency, such as the gyrofactor η_g and acceleration efficiency $\eta_{\rm acc}$. When comparing cases with different shock velocities, we normalize the acceleration rate by $(\gamma - \gamma_{\rm sh})\beta_{\rm sh}^{-2}$ to factor out the expected DSA scaling [Figure 3.6(b)].

Figures 3.6(a) and (b) illustrate the effects of varying M_A and $v_{\rm pt}/c$, respectively. As shown in Figure 3.6(a), cases with different Alfvénic Mach numbers exhibit broadly similar behaviors, except for the very low $M_A = 4$ case, which shows a slightly reduced

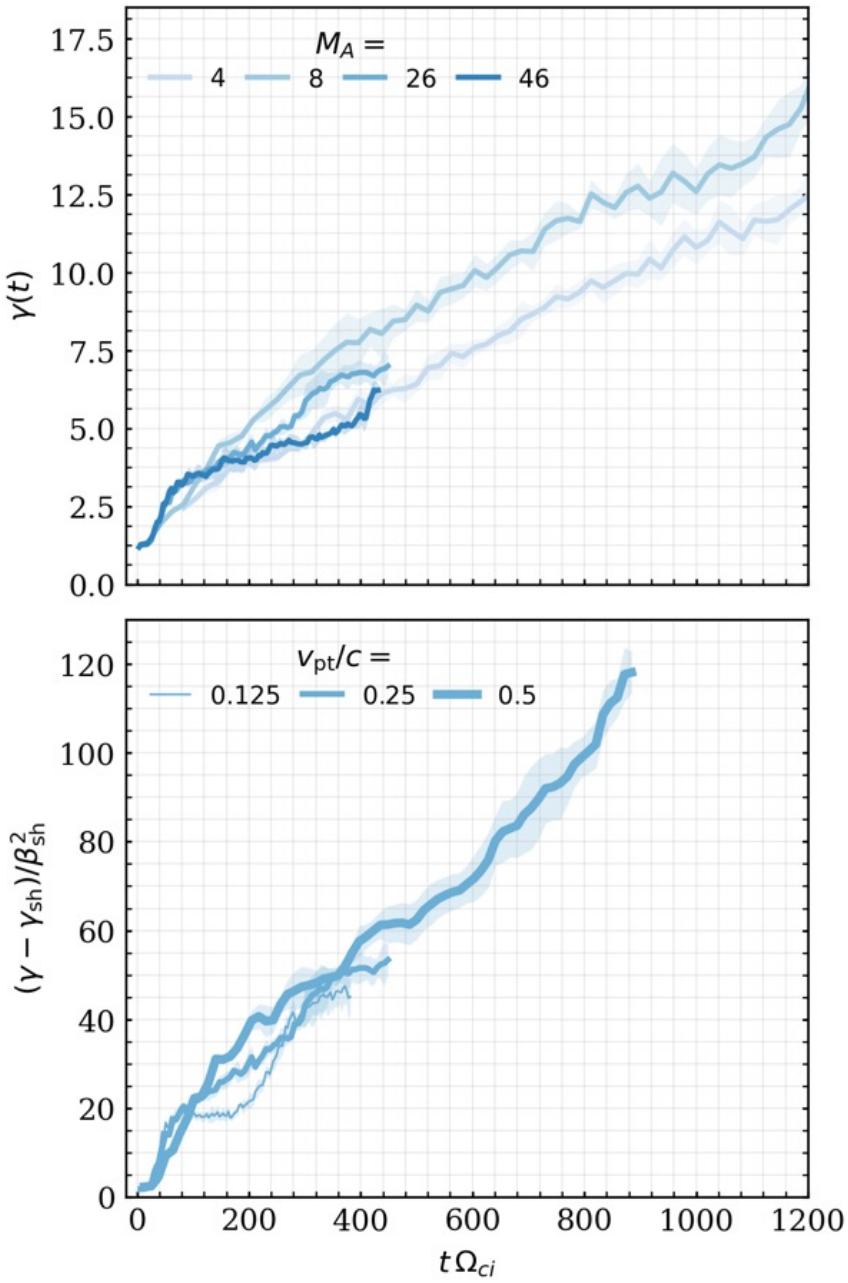

Figure 3.6: Same format as Figure 3.5, but showing the dependence on the Alfvénic Mach number and the injected particle velocity. (a) Time evolution of the mean Lorentz factor of the ten most energetic ions for different M_A. (b) Normalized energy gain, $(\gamma - \gamma_{\rm sh})\beta_{\rm sh}^{-2}$, for different injected velocities $v_{\rm pt}/c$. Shaded regions indicate one standard deviation. All other parameters are identical to the reference run (T10), unless otherwise specified.

acceleration rate compared to the reference run ($M_A = 26$). This is likely due to weaker self-generated turbulence, as confirmed by the presence of resonant streaming instability (Gupta et al., 2024b). Such a trend is expected, as the shock's Alfvénic Mach number must exceed order unity for efficient particle acceleration to occur (see Vink & Yamazaki (2014), who predicted a threshold of $M_A \simeq 5/2$). Accordingly, the acceleration rate, $\mathcal{C}^{-1}$, is expected to decrease significantly as $M_A \to 1$. When the injection velocity varies from

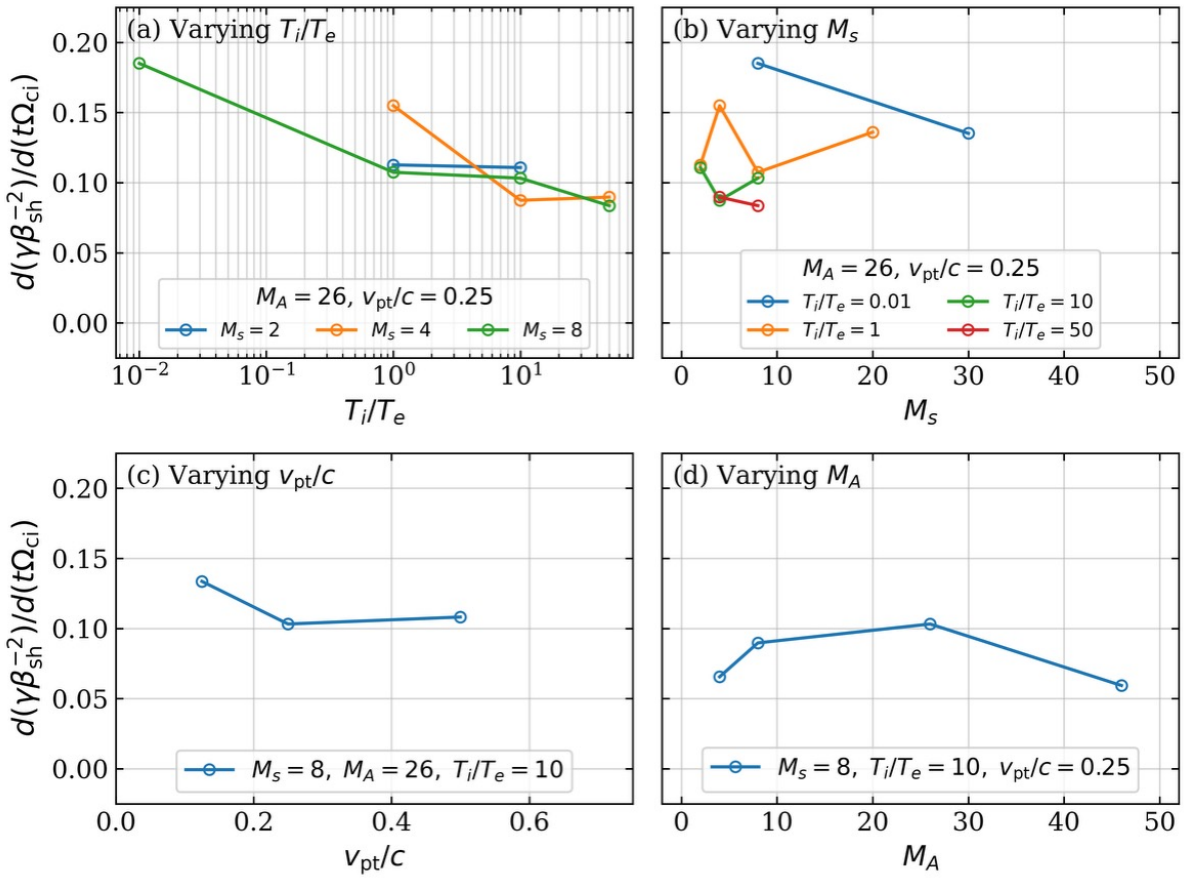

Figure 3.7: The normalized acceleration coefficient $d(\gamma/\beta_{\rm sh}^2)/d(t\Omega_{\rm ci})$ (i.e., the slope in Figures 3.5 and 3.6), as a function of key shock parameters, calculated from the linear slope of the energy gain at late times. (a) Dependence on T_i/T_e. (b) and (c) Dependence on M_s and M_A, respectively. (d) Dependence on $v_{\rm pt}/c$.

$v_{\rm pt}/c = 0.125$ to 0.5 in Figure 3.6(b), the normalized acceleration rates in all three runs remain remarkably similar, confirming that the acceleration efficiency follows the scaling predicted by Equation (3.7).

3.5.3 Scaling of acceleration rate

We next compare the normalized acceleration rate, $\mathcal{C}^{-1} = d(\gamma\beta_{\rm sh}^{-2})/d(t\Omega_{\rm ci})$, as shown in Figure 3.7. This coefficient is obtained from the slope of the mean energy gain during the late stage of acceleration [$t \gtrsim 100\ \Omega_{\rm ci}^{-1}$; see, e.g., Figure 3.6(b)]. As seen in Figure 3.7, the typical value of the normalized acceleration rate is $\mathcal{C}^{-1} \simeq 0.1$, varying by less than a factor of two across all parameter sets.

The reference parameters for Figure 3.7 are $M_A = 26$, $M_s = 8$, $T_i/T_e = 10$, and $v_{\rm pt}/c = 0.25$. Each panel varies one parameter while keeping the others fixed: T_i/T_e in (a) (colored lines for different M_s), M_s in (b) (colored lines for different T_i/T_e), M_A in (c), and $v_{\rm pt}/c$ in (d). The results show no clear dependence on M_s [Figure 3.7(b)] and only a weak, nearly flat trend with $v_{\rm pt}/c$ [Figure 3.7(d)]. A slight systematic decrease is

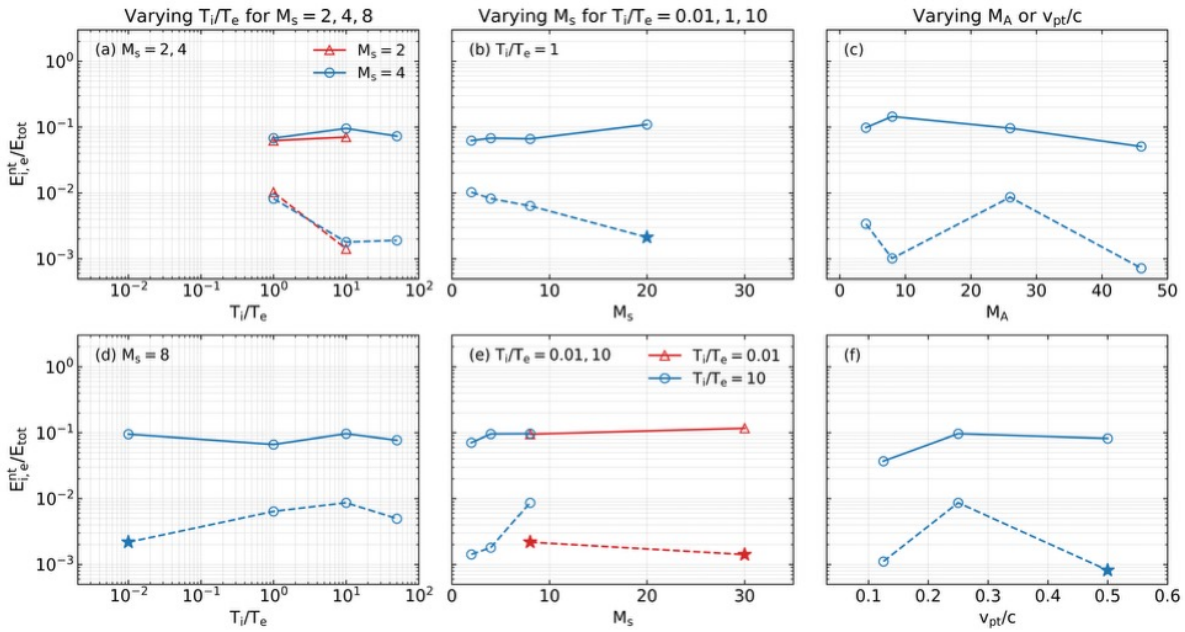

Figure 3.8: Fraction of non-thermal ion (solid lines) and electron (dashed lines) energy to total energy in the particle spectra across the parameter space. Non-thermal ions are efficiently accelerated, receiving $\sim 10\%$ of the total energy, while electrons remain much less efficient ($< 1\%$) or even suppressed in cases indicated by the $\star$ symbol. Left panels: the effect of T_i/T_e ratio with fixed $M_s = 2$ (red lines) and $M_s = 4$ (blue lines) in panel (a), and $M_s = 8$ in panel (d). Middle panels: the scaling with M_s when T_i/T_e is fixed at $T_i/T_e = 1$ in panel (b), and $T_i/T_e = 0.01$ (red) and $T_i/T_e = 10$ in panel (e). Right panels: variation with (c) M_A and (f) $v_{\rm pt}/c$. Unless explicitly stated otherwise, other parameters follow $T_i/T_e = 10$, $M_s = 8$, $M_A = 26$, and $v_{\rm pt}/c = 0.25$.

observed as ions become hotter relative to electrons (i.e., with increasing T_i/T_e).

Panel (c) indicates a modest dependence of the acceleration rate on the Alfvénic Mach number. While the acceleration efficiency is somewhat reduced at both low and high M_A, it remains comparable over the full range considered. The reduced acceleration efficiency at low M_A likely results from weaker self-generated turbulence, as discussed in Section 3.5.2. At very high M_A, however, the strong turbulence can excite SLAMS, which intermittently render parts of the shock superluminal and disrupt ion acceleration (see Zeković et al. (2025) for a detailed discussion). This suggests the existence of an optimal magnetic field strength for efficient ion acceleration by DSA in this regime.

To summarize, we have demonstrated that ions are efficiently accelerated over a broad range of physical conditions, indicating a robust capability of shocks for ion energization in BH coronae. The normalized acceleration rate varies by less than a factor of two across all tested parameters, consistent with the expectations from DSA theory.

3.6 Energy partition

In this section, we investigate the partitioning of shock energy into non-thermal ions and electrons (i.e., the acceleration efficiency), which is crucial for determining the relative power available for hadronic neutrino production and leptonic emission.

We define the energy fraction, or the acceleration efficiency, as

$$\frac{E_j^k}{E_{\rm tot}} = \frac{1}{E_{\rm tot}} \int d\gamma (\gamma - 1) m_j c^2 f_j^k(\gamma),$$

where $j \in \{i, e\}$ and $k \in \{\rm nt, th\}$ denote four different particle energy fractions: $E_i^{\rm nt}$, $E_e^{\rm nt}$, $E_i^{\rm th}$, and $E_e^{\rm th}$, corresponding to non-thermal ions, non-thermal electrons, thermal ions, and thermal electrons, respectively. The total particle energy is given by $E_{\rm tot} = \sum_j^k \int d\gamma\, (\gamma - 1) m_j c^2 f_j^k(\gamma)$. We use the same distinction between thermal and non-thermal populations of ions and electrons as described in Section 3.4.2.

The detailed scaling of the energy fractions of non-thermal ions (solid lines) and electrons (dashed lines) is depicted in Figure 3.8. Each line in the panels represents a parameter scan, varying one value while all others are held constant. Unless otherwise noted, the default parameters are those of the T10 case: $M_A = 26$, $M_s = 8$, $v_{\rm pt}/c = 0.25$, and $T_i/T_e = 10$. We present results for the scaling with varying T_i/T_e (also with a few M_s values) in the left panels (a) and (d); with varying M_s (at three T_i/T_e values) in the middle panels (b) and (e); and with M_A and $v_{\rm pt}/c$ in panels (c) and (f), respectively.

We find that non-thermal ions are efficiently accelerated, consistently receiving $\sim 10\%$ of the total energy. This high ion acceleration efficiency remains robust across all parameter surveys, even in the low sonic Mach number regime where inefficient acceleration is often assumed. As shown in the left (a, d) and middle (b, e) panels, the ion energy fraction $E_i^{\rm nt}/E_{\rm tot}$ remains nearly independent of T_i/T_e and M_s across all tested regimes. Similarly, Figures 3.8(c) and (f) show a weak dependence on M_A and $v_{\rm pt}/c$, with the ion acceleration efficiency slightly reduced at high M_A [panel (c)] and for slower shocks [panel (f)].

The electron acceleration efficiency is much lower than that of ions, with $E_e^{\rm nt}/E_{\rm tot}$ remaining below 1%. It also exhibits a more complex dependence, being highly sensitive to the upstream plasma parameters. A major contributing factor is that, in some cases with $v_{\rm pt}/c \geq 0.25$, we find that the maximum energy of the electron power-law tail does not continue to grow with time, leading to a significant reduction in the apparent acceleration efficiency. We mark such cases with the star symbol in Figure 3.8, for example, in the $T_i/T_e = 0.01$ runs in panel (e) (red dashed line) and the $v_{\rm pt}/c = 0.5$ run in panel (f). The physical origin of this behavior will be discussed in Chapter 4 (Section 4.3.1) ; however, because electrons remain energetically subdominant, this effect does not affect the ion acceleration results or the overall energy partition discussed above.

Most notably for implications relevant to BH coronae, $E_e^{\rm nt}/E_{\rm tot}$ shows a monotonically decreasing trend with increasing ion-to-electron temperature ratio T_i/T_e, as seen in panels (a) and (d). For $T_i/T_e = 1$, the efficiency is $\sim 10^{-2}$, whereas for high $T_i/T_e \gtrsim 10$, it decreases to $\sim 10^{-3}$. This result agrees with recent work on the electron injection threshold in quasi-parallel shocks (Gupta et al., 2025), which indicates that higher thermal electron speeds in the immediate upstream region favor more efficient electron acceleration.

The decline of electron acceleration in high T_i/T_e environments—conditions expected in BH coronae—imposes a strong constraint on the multi-messenger emission from these regions. In particular, it limits the energy available for primary leptons to produce synchrotron and inverse-Compton emission relative to the hadronic component responsible for neutrino production.

Chapter 4

Magnetic field and Electron dynamics

4.1 Introduction

In the previous chapter, we established that collisionless shocks in Black Hole coronae are efficient particle accelerators, particularly for protons. However, the acceleration of electrons—which is critical for the radiative signatures observed in X-rays and gamma-rays—depends sensitively on the microphysical conditions at the shock front. Unlike protons, which inject easily into the DSA cycle in quasi-parallel shocks, electrons require significant pre-heating and specific magnetic field geometries to overcome their low inertia and participate in the acceleration process. This chapter investigates the microphysical mechanisms governing these processes. First, we characterize the magnetic field amplification driven by streaming instabilities in the shock precursor, distinguishing between Resonant (RI) and Non-Resonant (NRI) modes. Second, we analyze how this self-generated turbulence regulates electron dynamics. Specifically, we explore two observed effects for electron dynamics: the trapping of electrons by superluminal magnetic structures in high-amplification regimes, and the difficulty of injection in high T_i/T_e plasmas where electrons are initially cold. Finally, we quantify the partition of energy into the thermal electron population, which serves as the reservoir for the non-thermal tail.

4.2 Magnetic field amplification

4.2.1 Resonant and Non-resonant modes

The nature of the upstream turbulence is determined primarily by the current density of the cosmic rays (streaming ions). In the regime of strong currents, non-resonant (NRI), right-handed (RH) circularly polarized modes are expected to dominate. Considering a simplified case where a cosmic ray population with density $n_{\rm cr}$ and net drift velocity v_d drives a current $J_{\rm cr} = en_{\rm cr}v_d$ through a background plasma of density n_i and magnetic field B_0, the wavenumber of the fastest-growing mode is given by linear theory (Bell,

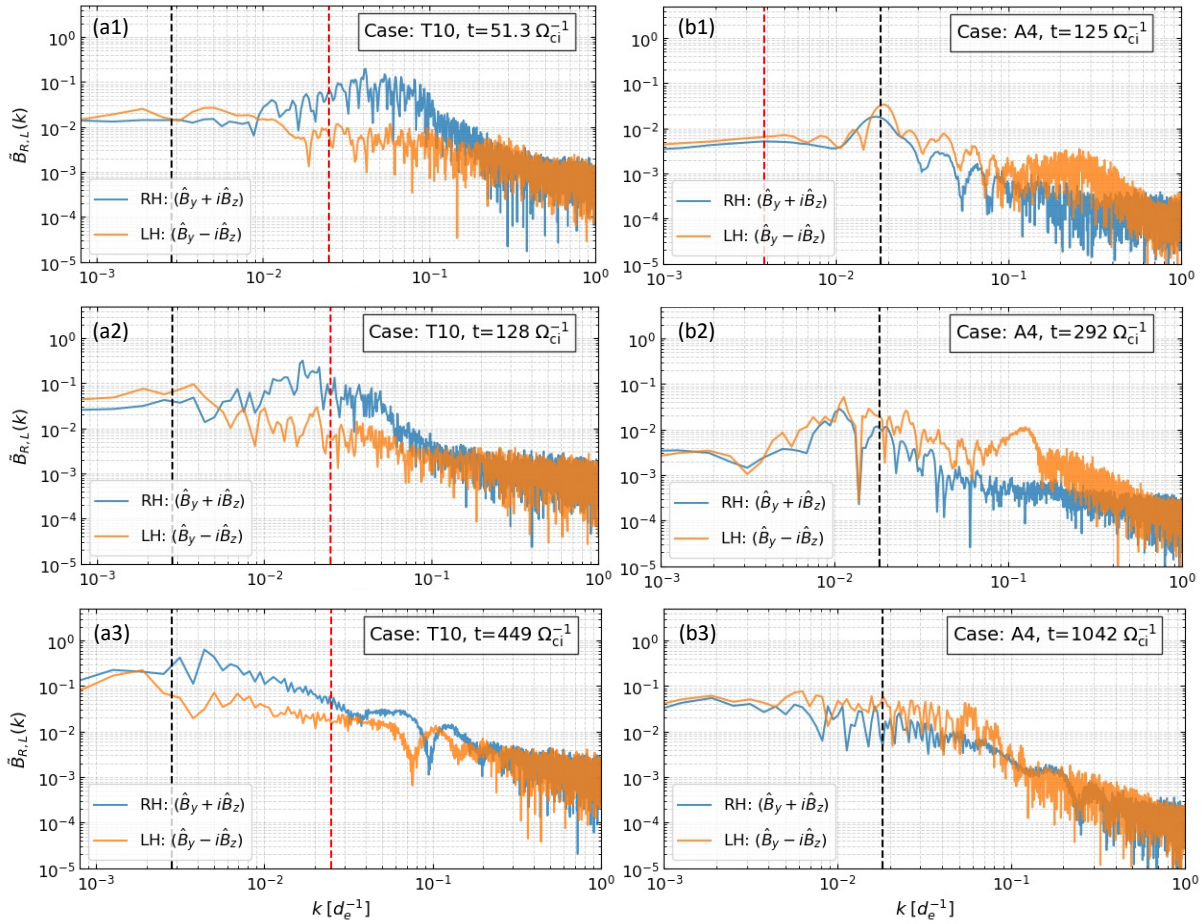

Figure 4.1: Time evolution of the spatial Fourier spectra for the NRI and RI regimes, represented by simulations T10 (left panels, $M_A = 26$) and A4 (right panels, $M_A = 8$). The spectra are calculated from the upstream magnetic field within the fixed range $500\ d_e \leq x - x_{\rm sh} \leq 10500\ d_e$. Power is decomposed into LH (orange) and RH (blue) modes to illustrate polarization. The vertical black dashed line indicates the wavenumber resonant with the mean gyroradius of back-streaming ions (Equation 4.3), while the vertical red dashed line marks the theoretical fastest-growing non-resonant mode (Equation 4.2). Panels (a1)–(a3) and (b1)–(b3) display snapshots at consecutive times for the T10 and A4 runs, respectively, showing the dominance of RH (Bell) modes in T10 and LH (Resonant) modes in A4.

2004):

$$k_{\rm max}^{\rm NR} = \frac{2\pi}{c}\frac{J_{\rm cr}}{B_0} = \frac{1}{2}\left(\frac{n_{cr}}{n_i}\right)\left(\frac{v_d}{v_{A,0}}\right) d_i^{-1} \ , \tag{4.1}$$

where $d_i = c/\omega_{pi}$ is the ion inertial length. In the context of collisionless shock simulations, the driving current is initially provided by ions reflected at the shock front. Assuming a drift velocity $v_d \simeq 2v_{\rm sh}$ and a typical injection fraction $n_{\rm cr}/n_i \sim 10^{-2}$, we can estimate the characteristic NRI wavenumber as:

$$k_{\rm max}^{\rm NR} \simeq 10^{-2} M_A \left(\frac{n_{cr}/n_i}{10^{-2}}\right) d_i^{-1} \ . \tag{4.2}$$

Conversely, in regimes with lower current densities (typically lower Alfvénic Mach numbers), the growth is dominated by the Resonant Instability (RI) (Skilling, 1971). This mode operates on the scale of the ion gyroradius, $k_{\rm max}^{R}\rho_{\rm cr} \sim 1$, and is characterized by a predominance of left-handed (LH) polarization. For shock parameters, estimating the gyroradius based on the reflected ion velocity yields:

$$k_{\rm max}^{\rm R} \simeq \frac{1}{2M_A} d_i^{-1} \ . \tag{4.3}$$

To identify the dominant instability mechanism in our simulations, we performed a spatial Fourier analysis of the upstream magnetic field, decomposing the fluctuations into LH ($|\tilde{B}_y - i\tilde{B}_z|$) and RH ($|\tilde{B}_y + i\tilde{B}_z|$) polarized modes. Figure 4.1 compares the spectral evolution of a high-Mach number case (T10, $M_A = 26$) and a low-Mach number case (A4, $M_A = 8$).

In the T10 run (left panels, a1–a3), the spectrum is consistently dominated by the RH mode (blue line), a clear signature of the Bell instability. At early times ($t = 51.3\ \Omega_{ci}^{-1}$), the power peaks at high wavenumbers, closely matching the theoretical NRI prediction indicated by the vertical red dashed line ($k \approx k_{\rm max}^{\rm NR}$). As the system evolves (panels a2–a3), the turbulence undergoes an inverse cascade: the power shifts toward smaller wavenumbers (larger scales) and broadens. By the end of the simulation, the dominant scale approaches the resonant scale of the reflected ions (vertical black dashed line). This behavior is consistent with recent studies of Bell instability saturation, where small-scale filaments coalesce into larger magnetic structures (Zacharegkas et al., 2024).

In contrast, the A4 run (right panels, b1–b3) exhibits a distinctly different behavior dominated by the LH mode (orange line), characteristic of the Resonant Instability. In this low-M_A regime, the theoretical NRI growth rate is suppressed, and the predicted NRI wavenumber (red dashed line) falls below the resonant scale, indicating that the conditions for small-scale Bell modes are not met. Consequently, the instability is driven by gyro-resonance. Notably, the spectral peak shifts progressively to the left (smaller k) over time. This shift reflects the acceleration process: as ions gain energy via DSA,

their gyroradii increase ($\rho_{\rm cr} \propto E$), driving resonant waves at progressively larger scales. Overall, the magnetic field amplification in the RI-dominated A4 case is approximately an order of magnitude weaker than in the NRI-dominated T10 case.

4.2.2 Magnetic field profile

Having identified the dominant instability modes, we now examine the spatial structure of the amplified magnetic field and its dependence on shock parameters. To isolate the secular trends from the strong temporal fluctuations characteristic of the turbulent precursor, we calculate the time-averaged spatial profile of the magnetic field. In our 1D simulation geometry, the longitudinal component B_x remains constant; therefore, we focus on the evolution of the transverse component, $B_\perp = \sqrt{B_y^2 + B_z^2}$, which captures the wave power generated by streaming instabilities.

4.2.2.1 Dependence on M_A and $v_{\rm pt}$

The Alfvénic Mach number (M_A) and the shock velocity (parameterized here by the upstream drift velocity $v_{\rm pt}$) are usually thought to be the primary determinants of the free energy available for magnetic field amplification.

Theoretical arguments based on equipartition suggest that the saturation level of the magnetic field in the limit of strong driving (Bell, 2004) should scale as $(B_{\rm sat}/B_0)^2 \propto M_A^2$, or more explicitly

$$\frac{B_{\rm sat}^2}{8\pi} \simeq \xi_{\rm cr}\, \rho\, v_{\rm sh}^2 \quad \Rightarrow \quad \frac{B_{\rm sat}}{B_0} \simeq M_A \sqrt{\xi_{\rm cr}}, \tag{4.4}$$

where $B_{\rm sat}$ is the saturated magnetic-field amplitude, B_0 the background field, ρ the upstream mass density, $v_{\rm sh}$ the shock (or CR drift) velocity, $\xi_{\rm cr}$ the fraction of the upstream ram pressure carried by cosmic rays, and $M_A \equiv v_{\rm sh}/v_A$ is the Alfvénic Mach number with $v_A = B_0/\sqrt{4\pi\rho}$. While controlled periodic-box simulations have confirmed this scaling under idealized conditions (Zacharegkas et al., 2024), the dynamic environment of a collisionless shock adds complexity As we will explore in detail later in this chapter, we generally do not expect the amplification to reach the equipartition level.

Figure 4.2 presents the time-averaged transverse magnetic field profiles for varying M_A [panels (a1), (a2)] and $v_{\rm pt}$ [panels (b1), (b2)]. Other parameters are fixed to the reference run, $M_s = 8$ and $T_i/T_e = 10$, for cases with varying M_A, $v_{\rm pt}/c$ is kept constant at 0.25. For the case with varying $v_{\rm pt}$, M_A remains at 26. The profiles are averaged over a duration of 100 $\Omega_{\rm ci}^{-1}$ specifically within the interval $150 \leq t\,\Omega_{\rm ci} \leq 250$. This window was selected to exclude initial numerical transients; particularly in low-M_A cases (where $150\ \Omega_{\rm ci}^{-1} < 80,000\ \omega_{\rm pe}^{-1}$), this timing ensures that the analysis remains unaffected by numerical artifacts or boundary effects.

As shown in Figures 4.2(a1) and (a2), the magnetic field amplification is strongly

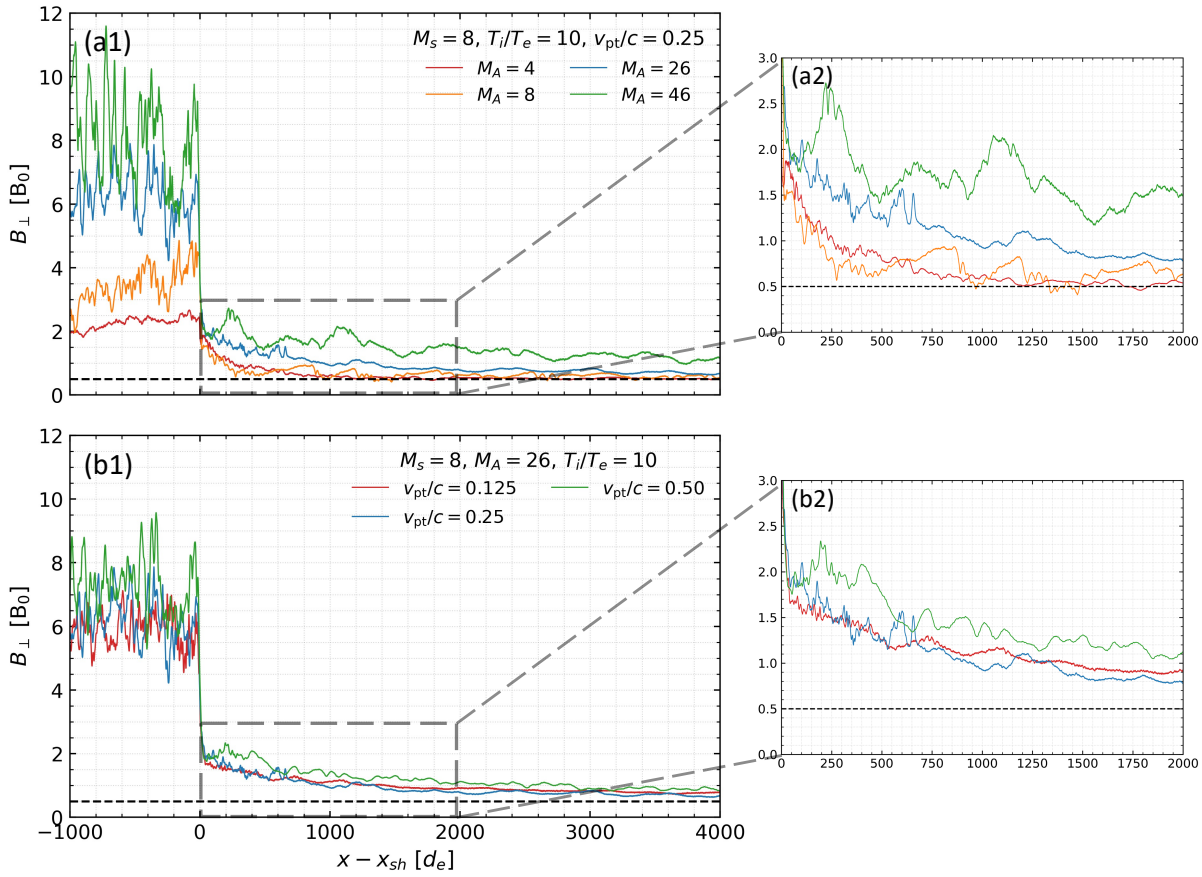

Figure 4.2: Time-averaged spatial profiles of the transverse magnetic field $B_\perp = \sqrt{B_y^2 + B_z^2}$. The profiles are averaged over a duration of 100 Ω_{ci}^{-1}, and the horizontal black dashed line indicates the initial transverse field strength ($B_0 \sin 30°$). Unless otherwise stated, shock parameters correspond to the reference run T10: $M_A = 26$, $M_s = 8$, $v_{pt}/c = 0.25$ (yielding $v_{sh}/c \approx 0.33$), and $T_i/T_e = 10$. (a1) Cases with varying Alfvénic Mach number M_A. (b1) Profiles for simulations with varying initial drift speed v_{pt}/c. Panels (a2) and (b2) display zoomed-in views of the near-shock region for (a1) and (b1), respectively.

positively correlated with M_A. For the highest Mach number case ($M_A = 46$, green line), the transverse field reaches peak values of $B_\perp/B_0 \gtrsim 10$ near the shock front ($x \approx x_{sh}$). Conversely, for the low-Mach number case ($M_A = 4$, orange line), the amplification is modest, barely exceeding the initial background field (indicated by the horizontal dashed line). This trend is consistent with previous kinetic simulations (Caprioli & Spitkovsky, 2014a; Gupta et al., 2024b). High-M_A shocks possess a larger reservoir of kinetic energy relative to the background magnetic energy density, allowing the instability to drive the field to much higher non-linear amplitudes before saturation occurs. Furthermore, the precursor region—where $B_\perp$ is significantly enhanced—extends further upstream for higher M_A cases, reflecting the longer diffusion lengths of the more energetic particles accelerated in strong shocks.

The dependence of the magnetic field profile on the upstream flow velocity v_{pt}/c

is shown in Figures 4.2(b1) and (b2). We observe that the saturation level increases with $v_{\rm pt}/c$, an effect that is most pronounced when comparing the trans-relativistic case ($v_{\rm pt}/c = 0.5$) to the slower cases ($v_{\rm pt}/c = 0.125$ or 0.25).This behavior contrasts with recent studies of non-relativistic shocks ($v_{\rm pt}/c = 0.05 - 0.2$), where Gupta et al. (2024b) found no noticeable dependence on $v_{\rm pt}/c$ when isolating the effect.

This discrepancy suggests that trans-relativistic shocks operate in a distinct regime compared to their non-relativistic counterparts. While Equation 4.4 predicts a scaling with M_A, it does not explicitly account for intrinsic velocity dependence in the injection physics. Our results imply that as the shock speed approaches c, the injection efficiency $\xi_{\rm cr}$ is no longer constant but likely increases, thereby driving stronger magnetic field amplification than predicted by non-relativistic scalings.

4.2.2.2 Dependence on M_s and T_i/T_e

Figure 4.3 presents the time-averaged profiles of the transverse field $B_\perp$ for a fixed Alfvénic Mach number ($M_A = 26$) and flow velocity ($v_{\rm pt}/c = 0.25$), systematically varying the upstream thermodynamic parameters M_s and T_i/T_e.

While M_A is the dominant control parameter, the dependence of magnetic field amplification on the sonic Mach number (M_s) and the ion-to-electron temperature ratio (T_i/T_e) remains less explored. As demonstrated in Figure 4.3, these thermodynamic parameters play a significant role in governing the saturation level of the magnetic field. We observe an inverse relationship between the temperature ratio and field amplification: increasing T_i/T_e at fixed M_s tends to suppress magnetic growth. In contrast, increasing M_s at fixed T_i/T_e generally enhances amplification.

Varying T_i/T_e at fixed M_s (panels a1–a3) modulates the overall amplification level, a sensitivity that becomes more pronounced at higher sonic Mach numbers. For $M_s = 2$ (a1), varying T_i/T_e from 1 to 10 yields only a modest effect; both profiles remain near $B_\perp/B_0 \sim \mathcal{O}(1)$ downstream, with relatively weak precursor activity. At $M_s = 4$ (a2), the dependence becomes distinct: the $T_i/T_e = 1$ case maintains a systematically higher $B_\perp$ than the hotter-ion cases ($T_i/T_e = 10, 50$), both in the near-shock region and further upstream. This trend peaks at $M_s = 8$ (a3), where low T_i/T_e results in substantially stronger and more spatially extended amplification. Notably, the $T_i/T_e = 0.01$ case remains elevated by a factor of a few over distances $\gtrsim 10^3 d_e$, whereas for $T_i/T_e \gtrsim 10$, the field relaxes to background levels much closer to the shock.

Similarly, case of varying M_s at fixed T_i/T_e [panels (b1)–(b3)] can also change amplification level. At $T_i/T_e = 10$ (b1), increasing M_s from 2 to 8 boosts the precursor peak amplitudes and raises the near-shock level (see inset), although the far-upstream profiles eventually converge. At $T_i/T_e = 1$ (b2), this trend extends to higher Mach numbers: the $M_s = 20$ case exhibits dramatically enhanced and spatially extended $B_\perp$, remaining well

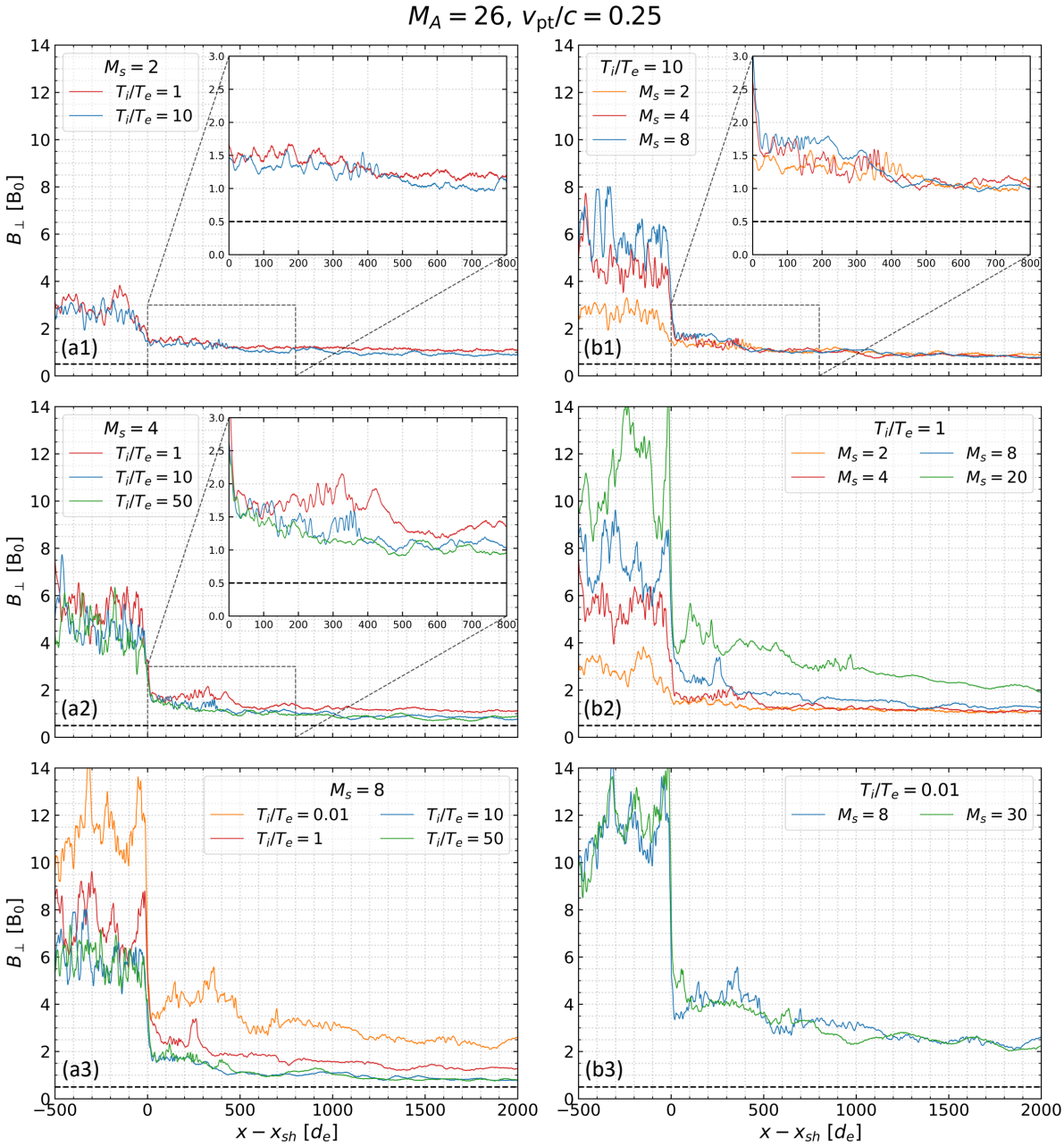

Figure 4.3: Time-averaged spatial profiles of the transverse magnetic field ($B_\perp = \sqrt{B_y^2 + B_z^2}$), formatted similarly to Figure 4.2. The profiles are averaged over a duration of $\Delta t = 100\ \Omega_{ci}^{-1}$ (see text for details); the horizontal black dashed line indicates the initial transverse field strength ($B_0 \sin 30°$). Panels are organized to isolate thermodynamic effects: (a1)–(a3) show variations in T_i/T_e at fixed M_s, while (b1)–(b3) show variations in M_s at fixed T_i/T_e. Unless otherwise stated, shock parameters correspond to the reference run T10: $M_A = 26$, $M_s = 8$, $v_{pt}/c = 0.25$, and $T_i/T_e = 10$. Insets display zoomed-in views of the shock transition.

above the lower-M_s runs out to the edge of the plotted domain. However, at very small T_i/T_e (b3), increasing M_s from 8 to 30 alters the profile only marginally. This suggests that once the precursor is strongly driven (as facilitated by the low temperature ratio), the amplification saturates, rendering the profile less sensitive to further increases in M_s over the explored range.

The increase of magnetic-field amplification with increasing sonic Mach number M_s and decreasing temperature ratio T_i/T_e indicates that colder upstream ions favor stronger amplification. A similar positive dependence on M_s has been reported in recent quasi-parallel shock simulations (Gupta et al., 2024b). In addition, our parameter survey shows that T_i/T_e can strongly modulate the amplified field level, consistent with controlled numerical expectations that finite ion temperature can reduce the efficiency of the NRI through thermal/kinetic effects and damping (e.g., Reville et al., 2008; Zweibel & Everett, 2010; Marret et al., 2021).

4.2.3 Magnetic field amplification

In Figure 4.4, we summarize how the saturated upstream magnetic-field amplification depends on the four control parameters explored in this work: M_s, M_A, $v_{\rm pt}/c$, and T_i/T_e. For each simulation, we quantify the amplification using the spatially and temporally averaged field in the upstream precursor, $\langle (B_{\rm sat}/B_0)^2 \rangle_{x,t}$, where the spatial average is taken over $x_{\rm sh} \leq x \leq 3M_A d_i$ (i.e., out to a few typical ion gyroradii upstream) and the temporal average is taken over $\Delta t = 50\,\Omega_{\rm ci}^{-1}$ during the quasi-steady saturation stage. This definition is designed to capture the amplification level that is dynamically relevant for particle scattering and injection, while avoiding the immediate shock transition where strong gradients and intermittency can bias the measurement.

To capture these dependencies in a compact form, we fit all simulations simultaneously with a single multiplicative power-law scaling,

$$\left(\frac{B_{\rm sat}}{B_0}\right)^2 = 1.86\, M_s^{0.69\pm0.11}\, M_A^{0.26\pm0.10} \left(\frac{v_{\rm pt}}{c}\right)^{0.89\pm0.28} \left(\frac{T_i}{T_e}\right)^{-0.17\pm0.03}, \tag{4.5}$$

obtained via a log–log least-squares regression across the full dataset. The solid curves in Figure 4.4 show the best-fit prediction evaluated along the corresponding one-parameter slices through parameter space (i.e., varying one parameter while holding the others at the values indicated in each panel). The shaded regions are the associated uncertainty bands propagated from the fitted parameter uncertainties; they illustrate how the combined uncertainty maps into $(B_{\rm sat}/B_0)^2$ across the plotted ranges.

The fitting results suggest a rather weak dependence of the amplification level on Alfvénic Mach number, $(B_{\rm sat}/B_0) \propto M_A^{0.26}$ compared to Equation 4.4. This deviation is consistent with the non-linear saturation mechanism of NRI described by Riquelme &

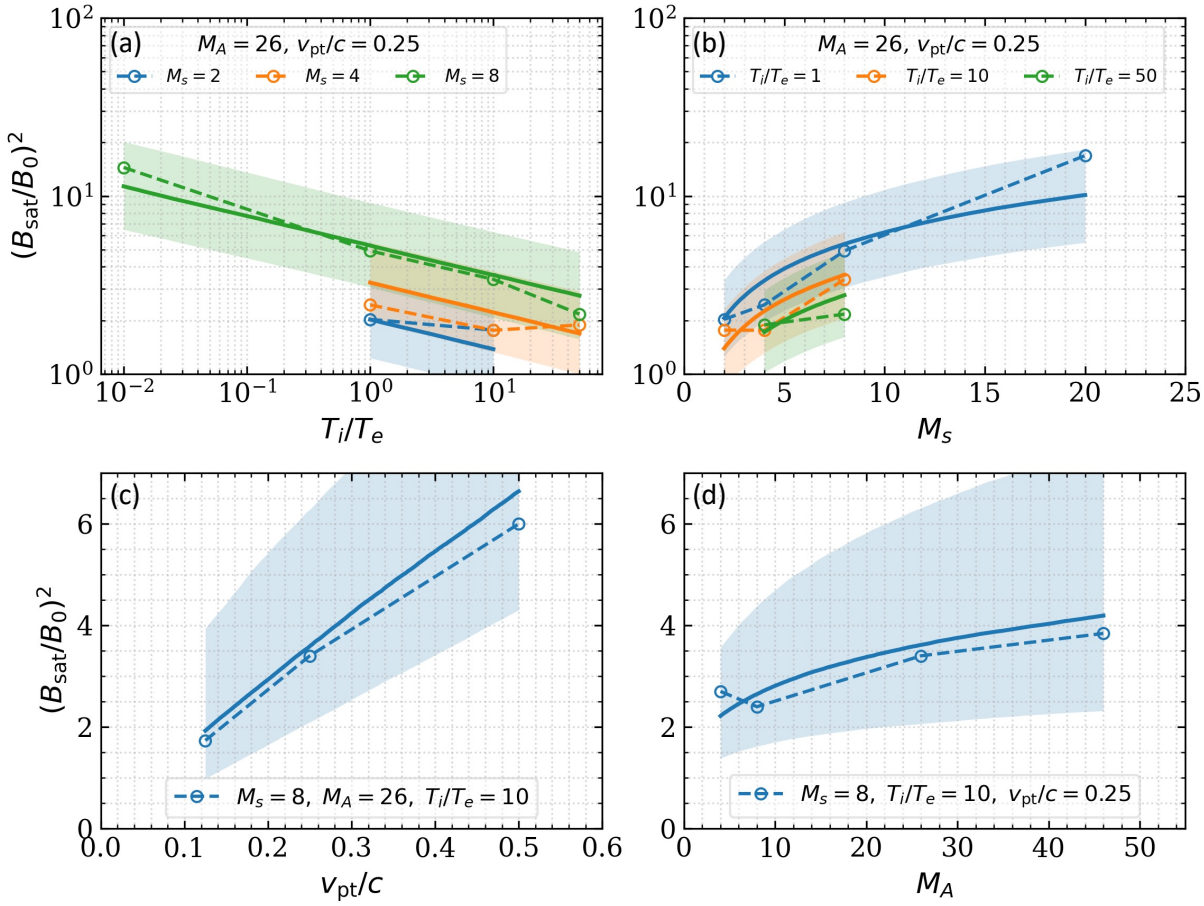

Figure 4.4: Dependence of the saturation total magnetic field amplification $(B_{\rm sat}/B_0)^2$ on M_s, M_A, $v_{\rm pt}/c$, and T_i/T_e. The field values are averaged spatially over $x_{\rm sh} < x < 3M_A d_i$ (corresponding to three typical ion gyroradii) and temporally over $\Delta t = 50\ \Omega_{\rm ci}^{-1}$. Circles connected by dashed lines represent simulation data. Solid lines of the corresponding color indicate best fits in Equation 4.5, with shaded regions denoting the uncertainty of the fitted parameters. (a) Dependence on T_i/T_e; each line represents a fixed sonic Mach number $M_s = 2, 4$, or 8. (b) Dependence on M_s for various temperature ratios T_i/T_e ranging from 1 to 50. Panels (c) and (d) display the scaling with $v_{\rm pt}/c$ and M_A, respectively. Unless otherwise stated, shock parameters correspond to the reference run T10: $M_A = 26$, $M_s = 8$, $v_{\rm pt}/c = 0.25$, and $T_i/T_e = 10$.

Spitkovsky (2009). They demonstrated that the instability saturates via current disruption when the gyroradius of the driving cosmic rays becomes comparable to the wavelength of the growing mode ($\rho_{\rm cr} \sim \lambda_I$), preventing the magnetic field from reaching equipartition. While Riquelme & Spitkovsky noted that an externally enforced current could drive the field until $v_A \sim v_d$, the self-consistent saturation observed here aligns with the current-disruption limit.

Hybrid PIC simulations of non-relativistic shocks have similarly reported saturation levels below the M_A^2 prediction, finding instead that $(B/B_0)^2$ scales linearly with M_A (Caprioli & Spitkovsky, 2014a). While our fitted Alfvénic exponent ($\alpha_A = 0.26$) initially appears inconsistent with this linear scaling, it is important to note that the simulations in Caprioli & Spitkovsky (2014a) assumed the sonic and Alfvénic Mach numbers such that $M_s = M_A$, effectively fixed $\beta \sim 1$. If we enforce this constraint in Equation 4.5 by summing the exponents for M_s and M_A, we recover a total Mach-number dependence of $0.69 + 0.26 = 0.95$. This is remarkably close to unity, confirming that our results are consistent with the linear scaling found in Caprioli & Spitkovsky (2014a).

Overall, Figure 4.4 shows that a single global scaling law provides a useful description of the saturation level across the parameter space studied here, and it provides a convenient bridge between the upstream instability physics and the electron dynamics discussed in the next sections.

4.3 Electron dynamics

In this section, we examine the electron dynamics from our shock simulations (Table 3.1). As briefly discussed in Section 3.6, in contrast to the universally efficient acceleration of ions, the electron dynamics are much more complex. Here, we outline several effects observed in our simulations and analyze their underlying mechanisms.

Having characterized the upstream magnetic turbulence in the previous section, we now explore its interplay with electron dynamics.

4.3.1 Electron acceleration suppression by strong magnetic field amplification

Instabilities driven by streaming ions are essential not only for ion acceleration but also for electron acceleration through DSA. This effect is evident in the electron spectrum in Figure 3.3(a), where the initial power-law tails of electrons stall at the pre-acceleration stage until $t \sim 150\ \Omega_{\rm ci}^{-1}$, when ion-driven fluctuations are well developed.

However, when the amplification becomes too strong, the injection into DSA process of electrons can be suppressed (preacceleration may still operate). These are the cases marked by star symbol brieftly discussed in Section 3.6.

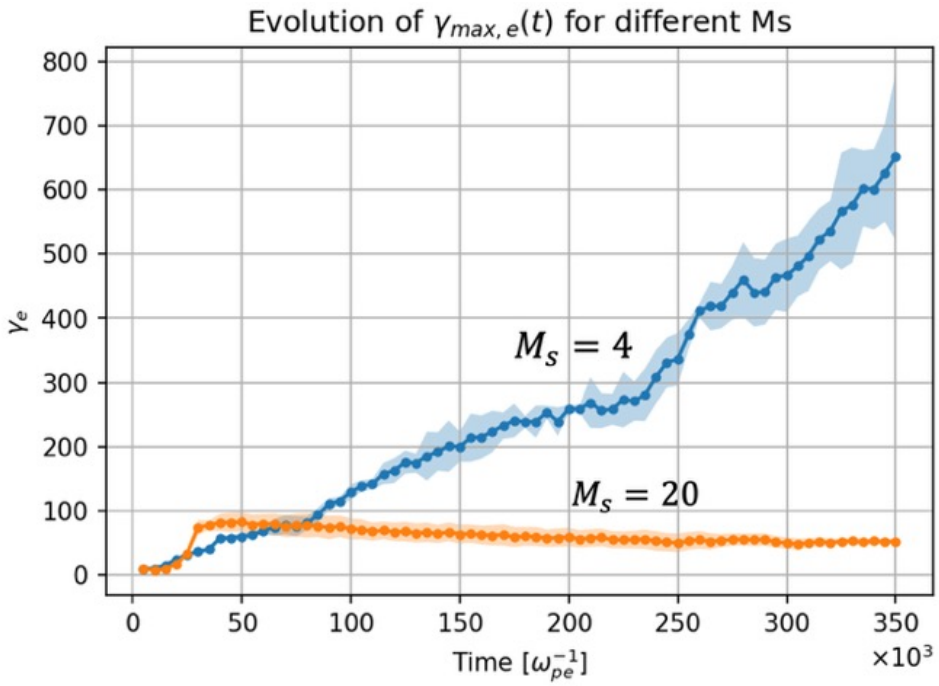

Figure 4.5: Time evolution of the mean Lorentz factor $\gamma_e(t)$ of the ten most energetic electrons for runs S4T1 ($M_s = 4$) and S20T1 ($M_s = 20$). Common parameters are $M_A = 26$, $T_i/T_e = 1$, and $v_{\rm pt}/c = 0.25$. Shaded regions indicate the standard deviation. In the $M_s = 4$ case, the electron energy increases steadily over time, indicative of the DSA process. In contrast, for the $M_s = 20$ case, although electrons quickly reach $\gamma_e \sim 100$ via pre-acceleration, their acceleration subsequently stalls. This corresponds to the much stronger magnetic field amplification observed in the $M_s = 20$ case [see Figure 4.3(b2)].

4.3.1.1 Critical field assesment

First, we illustrate the impact of magnetic field amplification on electron energization. Figure 4.5 compares the time evolution of the mean Lorentz factor of the most energetic electrons in two runs differing only in sonic Mach number. Despite identical upstream Alfvénic Mach numbers and plasma parameters, the acceleration histories diverge significantly.

For the lower Mach number case ($M_s = 4$), $\gamma_e(t)$ grows continuously, consistent with the DSA process. In contrast, for the high Mach number case ($M_s = 20$), electrons experience an initial phase of efficient pre-acceleration but fail to undergo further energization, leading to a clear saturation in γ_e. This behavior is directly linked to the stronger magnetic field amplification in the high M_s run [see Figure 4.3(b2) for comparison between these two cases].

To understand the suppression mechanism, we consider the kinematic constraints on electron transport in the upstream rest frame. For an electron to inject intp the DSA cycle, it must be able to move back and forth across the shock interface. Since electrons have gyroradii much smaller than the coherence length of the turbulence, they

are effectively tied to magnetic field lines and diffuse primarily parallel to them. The maximum velocity an electron can sustain along the shock normal (the x axis in our case) is limited by the projection of its speed along the magnetic field line. Assuming the electron travels at nearly the speed of light c, this projected velocity is $v_{x,\max} \approx c \cos\theta_{Bn}$, where θ_B is the angle between the local magnetic field and the shock normal.

A shock is defined as *superluminal* when the shock propagation velocity, $v_{\rm sh}$, exceeds the speed of the intersection point between the magnetic field line and the shock front:

$$v_{\rm sh} \geq c \cos\theta_B. \tag{4.6}$$

Physically, this condition implies that electrons moving toward the upstream cannot kinetically outrun the shock. Consequently, they remain trapped in the downstream region, thereby suppressing injection into DSA.

Initially, the simulations listed in Table 3.1 (where $\theta_{B,0} = 30°$) are subluminal. However, strong upstream amplification can significantly modify the obliquity. At saturation, the effective magnetic obliquity becomes $\cos\theta_B = B_x/B_{\rm sat}$. Since the streaming instability primarily amplifies transverse components [consistent with our configuration and multi-dimensional studies; e.g., Zacharegkas et al. (2024)], we approximate $B_x \approx B_{x,0} = B_0 \cos\theta_{B,0}$. Substituting this relation into the superluminal condition yields:

$$\frac{B_{\rm sat}}{B_0} \geq \frac{c}{v_{\rm sh}} \cos\theta_{B,0}\ . \tag{4.7}$$

This inequality establishes the threshold of magnetic field amplification required for the shock to become superluminal to electrons. Equivalently, one may define a critical field strength,

$$B_{\rm sat} \geq B_{\rm crit} \equiv B_0 \left(\frac{c}{v_{\rm sh}}\right) \cos\theta_{B,0}, \tag{4.8}$$

above which electron injection into DSA is strongly suppressed.

4.3.1.2 Consequences of suppression by strong magnetic field amplification

Next, we investigate the impact of this critical field amplification ($B_{\rm sat}/B_{\rm crit} \gtrsim 1$) on electron acceleration. We quantify this impact using two primary metrics: the rate of increase of the maximum electron energy, $\dot{E}_{\rm max,e} \equiv dE_{\rm max,e}/dt$ (normalized to $m_i v_{\rm sh}^2 \Omega_{ci}$), which tracks the temporal evolution of γ_e shown in Figure 4.5 (representing the extension of the power-law tail); and the electron acceleration efficiency, $E_e^{\rm nt}/E_{\rm tot}$ (as defined in Chapter 3, Section 3.6).

As illustrated in Figure 4.6, both measured quantities drop significantly in the superluminal regime. The stagnation or decrease of $\dot{E}_{\rm max,e}$ in panel (a) provides the most direct evidence of this suppression, as DSA is the only channel for accelerated electrons to gain energy following pre-acceleration. The only instance where $\dot{E}_{\rm max,e} \sim 0$ despite

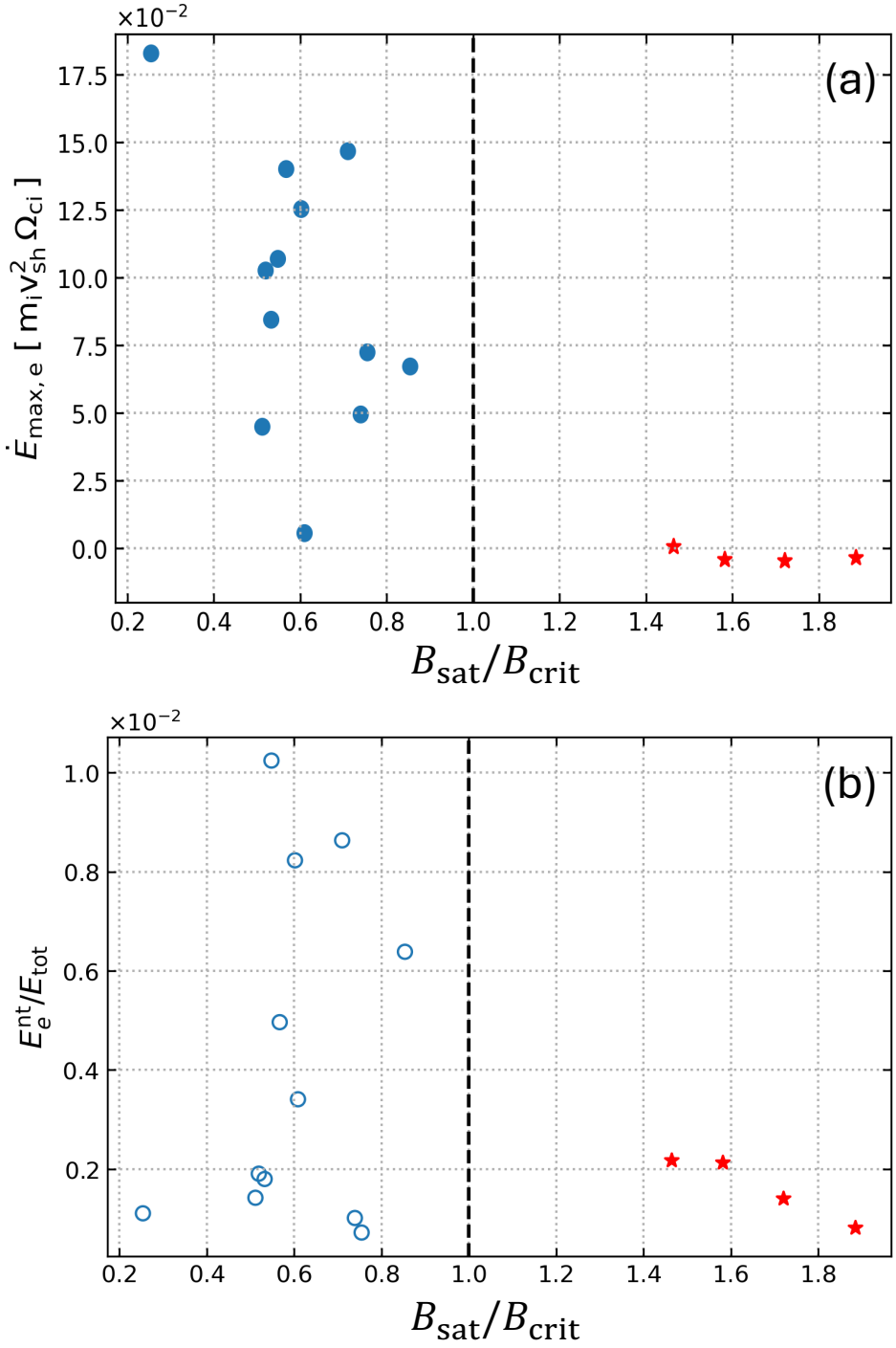

Figure 4.6: Dependence of electron acceleration metrics on the magnetic field amplification level, specifically the ratio of the saturation field to the critical superluminal field ($B_{\rm sat}/B_{\rm crit}$). The vertical dashed line at $B_{\rm sat}/B_{\rm crit} = 1$ marks the transition threshold: configurations with $B_{\rm sat} < B_{\rm crit}$ (blue circles) remain locally subluminal, while those with $B_{\rm sat} > B_{\rm crit}$ (red stars) become locally superluminal. (a) Normalized rate of increase of the maximum electron energy, $\dot{E}_{\rm max,e} \equiv dE_{\rm max,e}/dt$, in units of $m_i v_{\rm sh}^2 \Omega_{ci}$ (note the $\times 10^{-2}$ scale). (b) Non-thermal electron acceleration efficiency, $E_e^{\rm nt}/E_{\rm tot}$ (defined in Chapter 3; $\times 10^{-2}$ scale). Both quantities decrease sharply for $B_{\rm sat}/B_{\rm crit} \gtrsim 1$, demonstrating the suppression of electron injection in the locally superluminal regime.

$B_{\rm sat}/B_{\rm crit} < 1$ is the A4 run ($M_A = 4$), as seen in Figure 4.6. This exception is attributed to the lack of magnetic turbulence generated by streaming instabilities in the shock upstream. Similar 1D PIC simulation studies Gupta et al. (2024b); Shalaby (2024) also report this slow energy increase when $M_A \leq 5$.

The acceleration efficiency $E_e^{\rm nt}/E_{\rm tot}$ is also suppressed to $\sim 0.1\%$, approximately an order of magnitude lower than the typical efficiency of $\sim 1\%$. However, the situation is nuanced because the electron population may still undergo pre-acceleration processes, such as SDA, to reach $\gamma_e \sim 100$. Although not observed in our survey, if this process is efficient, it could artificially inflate the acceleration efficiency even if the maximum energy does not increase. Furthermore, some cases where $B_{\rm crit}/B_0 < 1$ also exhibit low acceleration efficiency due to other factors. This includes cases with high T_i/T_e and low $M_s \leq 4$. As we will clarify later, electrons in these simulations had not yet reached a steady state by the end of the run, suggesting the low efficiency in these cases may be transient.

We also note relevant results from 2D shock studies. Although inhibited by 1D geometry, multi-dimensional fluctuations could provide paths for a small fraction of electrons to escape. This can lead to an unclear signature in $\dot{E}_{\rm max,e}$, while suppression of the acceleration efficiency is still expected, at the level of $\sim 0.1\%$ as Figure 4.6(b). Simulating 2D Bell-mediated shocks is computationally expensive; consequently, while such studies exist, they typically require shock parameters of order $v_{\rm sh}\gamma_{\rm sh} > 1$ to yield meaningful results, often limiting them to the $B_{\rm sat}/B_{\rm crit} > 1$ regime studied here. Additionally, if the transverse box size is too small—less than $2\rho_i$ (about 5000 y-grids in the reference simulation) according to P Crumley et al. (2019)—the results essentially mimic 1D shocks. Nevertheless, two previous studies are particularly relevant P Crumley et al. 2019; Jikei et al. 2025. These studies report an electron acceleration efficiency of $E_e^{\rm nt}/E_{\rm tot} \sim 0.1\%$, consistent with our findings (Jikei et al. (2025) reports slightly higher values due to a different choice in the break Lorentz factor). While $E_e^{\rm nt}/E_{\rm tot}$ was reported to increase, it remains unclear if the electron dynamics reached a steady state, as their simulation timescales were much shorter than those presented here.

In summary, the combined suppression of $\dot{E}_{\rm max,e}$ and $E_e^{\rm nt}/E_{\rm tot}$ for $B_{\rm sat}/B_{\rm crit} > 1$ confirms that electron injection into DSA is suppressed once magnetic field amplification forces the shock obliquity beyond the critical limit.

4.3.2 Electron acceleration with different Ti/Te

Figure 4.7 shows the downstream evolution of electron and ion energy spectra, $(\gamma-1)f(\gamma)$, for shocks with varying T_i/T_e, comparing cases with $M_s = 4$ (left panels) and $M_s = 2$ (right panels). Panels (a1)–(a3) correspond to $M_s = 4$ with increasing $T_i/T_e = 1$, 10, and 50, while panels (b1)–(b2) show $M_s = 2$ cases with $T_i/T_e = 1$ and 10. In each panel, the

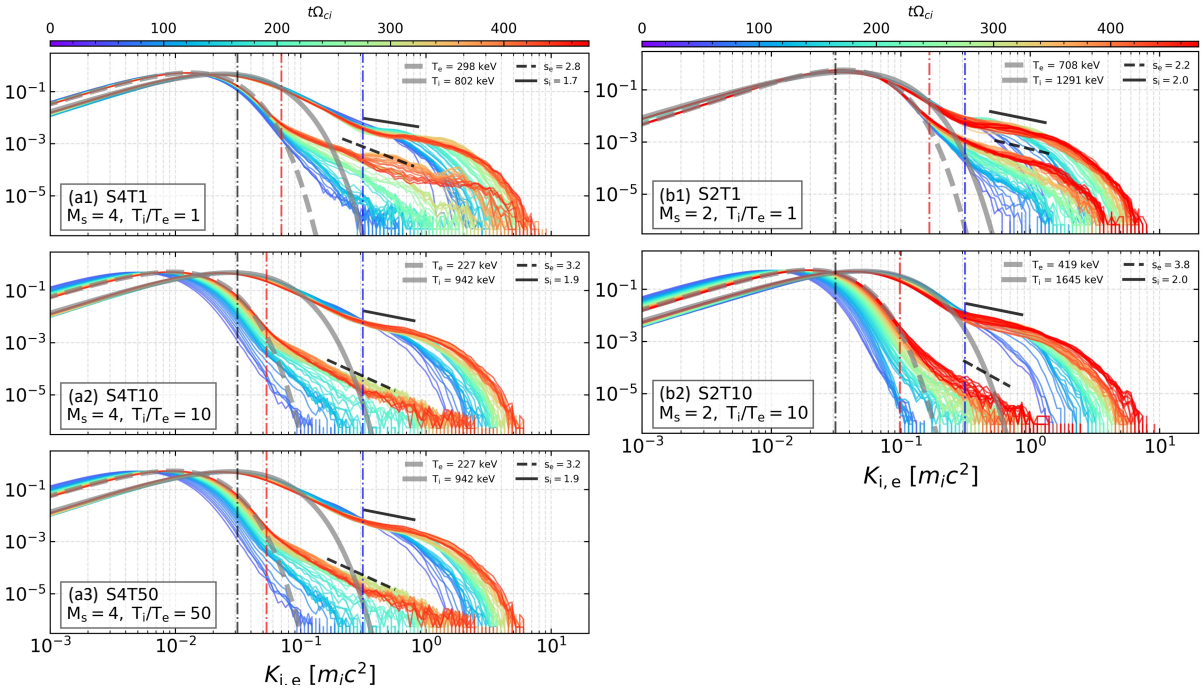

Figure 4.7: Downstream electron and ion spectra, $(\gamma - 1)f(\gamma)$, and their time evolution [similar to Figure 3.3(a)], for simulations with fixed $M_s = 4$ (left panels) and $M_s = 2$ (right panels), and varying T_i/T_e. We focus on the evolution of the electron spectra to illustrate the reduced electron acceleration efficiency in cases with high T_i/T_e, compared to the $T_i/T_e = 1$ case. For high T_i/T_e runs [panels (a2), (a3), and (b2)], thermal electrons with $K_e < (\gamma_{\rm br,e} - 1)m_ec^2$ (i.e., bulk electron population on the left side of the red dashed-dotted lines) increase steadily over the duration of the simulations, whereas the $T_i/T_e = 1$ cases [panels (a1) and (b1)] show no significant electron heating. Other parameters are identical for all cases: $M_A = 26$ and $v_{\rm pt}/c = 0.25$.

spectra are tracked over time, with color indicating progression from early (blue) to late (red) stages of the simulation. The vertical dashed lines mark the electron break energy $\gamma_{\rm br,e}$ separating the bulk thermal population from the non-thermal tail.

For the $T_i/T_e = 1$ cases [panels (a1) and (b1)], the electron spectra exhibit a relatively stable thermal peak and a well-developed non-thermal tail, with little evolution in the thermal component over time. In contrast, for higher T_i/T_e runs [panels (a2), (a3), and (b2)], the low-energy electron population below $\gamma_{\rm br,e}$ increases steadily throughout the simulation. This trend indicates continuous electron heating in the downstream region, while the non-thermal tail remains comparatively weak and shows limited extension to higher energies over the simulated timescales.

The effect is more pronounced at lower sonic Mach number. For $M_s = 2$ and $T_i/T_e = 10$ [panel (b2)], the thermal electron population grows significantly, but the formation of an extended power-law tail is strongly suppressed compared to the $T_i/T_e = 1$ case. Even for $M_s = 4$, increasing T_i/T_e from 10 to 50 primarily enhances the bulk electron energy, with only modest changes to the high-energy tail.

These results suggest that, in simulations with high T_i/T_e, electrons may still be in the process of heating toward a quasi-saturated downstream state by the end of the run. If efficient diffusive shock acceleration requires electrons to reach a sufficiently high thermal energy before injection becomes effective, then the low acceleration efficiency observed in these cases may be, at least in part, transient. While our simulations do not extend long enough to determine whether such saturation is eventually reached, the persistent growth of the thermal electron component indicates that the electron population has not yet fully equilibrated. Consequently, the suppressed non-thermal acceleration seen here should be interpreted with caution, particularly for low-M_s and high-T_i/T_e configurations.

4.3.3 Partition into thermal electron

Figure 4.8 summarizes the downstream energy partition in our shock survey, plotting the fractions of the total energy carried by thermal ions ($E_i^{\rm th}$; green), thermal electrons ($E_e^{\rm th}$; orange), non-thermal ions ($E_i^{\rm nt}$; blue), and non-thermal electrons ($E_e^{\rm nt}$; red). Each panel varies one control parameter while keeping the others fixed (as indicated), and the $\star$ symbols mark cases with $B_{\rm sat}/B_{\rm crit} > 1$.

A robust feature across all panels is that shocks deposit a substantial and fairly stable fraction of the downstream energy into thermal electrons, $E_e^{\rm th}/E_{\rm tot} \sim 0.2$–$0.3$, with only weak dependence on T_i/T_e, M_s, M_A, or $v_{\rm pt}/c$ within the explored parameter space (orange curves in panels a–f). In contrast, the non-thermal electron fraction $E_e^{\rm nt}/E_{\rm tot}$ (red) remains much smaller and is more sensitive to parameters and to the superluminal transition, consistent with the suppression trends discussed earlier. The ion components show the complementary behavior: $E_i^{\rm th}/E_{\rm tot}$ (green) stays at the dominant level, while

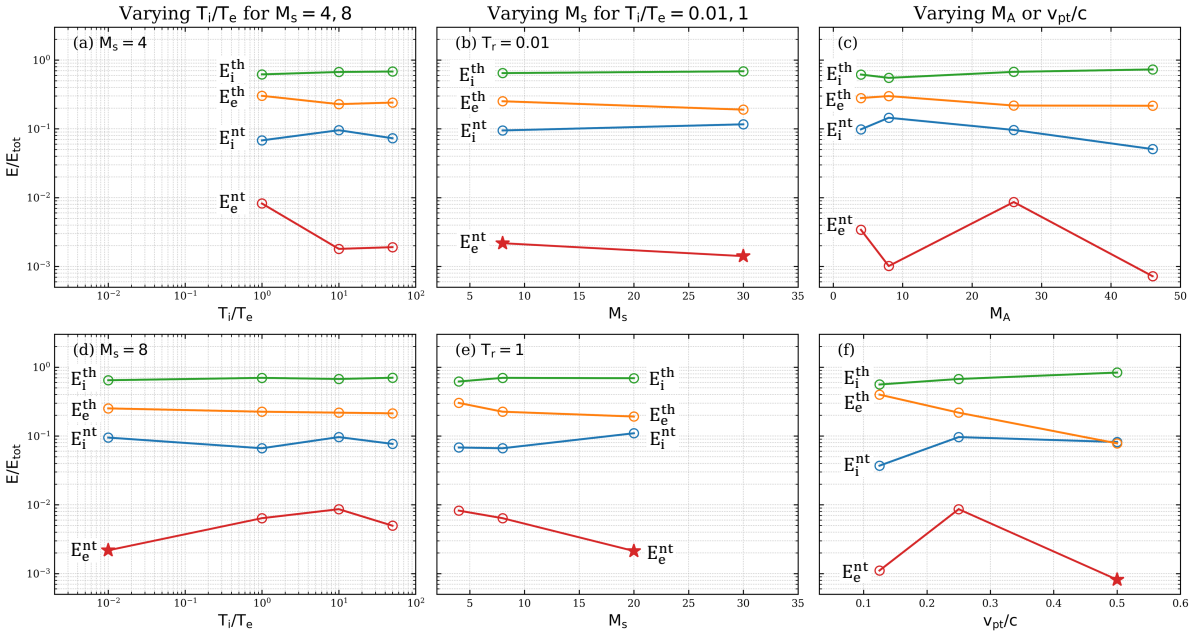

Figure 4.8: Full version of the energy fractions, similar to Figure 3.6, but including the post-shock (downstream) thermal energy fractions of ions and electrons relative to the total energy. Here we focus on the thermal electron energy fraction $E_e^{\rm th}$ (orange line). Shocks consistently inject a significant fraction of energy into electron heating, resulting in a post-shock thermal electron energy fraction of $E_e^{\rm th}/E_{\rm tot} \sim 0.3$. The $\star$ symbols again indicate cases with $B_{\rm sat}/B_{\rm crit} > 1$. Left panels: effect of the T_i/T_e ratio at fixed $M_s = 4$ in panel (a) and $M_s = 8$ in panel (d). Middle panels: scaling with M_s at fixed $T_i/T_e = 0.01$ in panel (b), and $T_i/T_e = 1$ in panel (e). Right panels: variation with (c) M_A and (f) $v_{\rm pt}/c$. Unless explicitly stated otherwise, parameters are $T_i/T_e = 10$, $M_s = 8$, $M_A = 26$, and $v_{\rm pt}/c = 0.25$.

$E_i^{\rm nt}/E_{\rm tot}$ (blue) varies at the ~ 0.05–0.2 level depending on the setup.

Interpreting this in terms of shock dissipation, Figure 4.8 indicates a near-universal channel in which a non-negligible fraction of the bulk kinetic energy processed by collisionless shocks is converted into downstream thermal electrons. In astrophysical environments where such shocks are plausible—including black-hole coronae and AGN systems—an injected thermal-electron energy fraction at the level of ~ 0.3 is potentially important for radiative modeling. Even if electron injection into DSA is inefficient in some regimes (e.g., locally superluminal configurations), the thermal electron reservoir produced by shock heating can still be energetically significant, and may lead to measurable changes in the emitted spectrum (e.g., by modifying the temperature and normalization of the radiating electron population).

This point becomes particularly relevant if the same shocks are invoked primarily as ion accelerators, for example in scenarios aiming to account for high-energy neutrinos (such as those detected by IceCube) via hadronic interactions. In such a picture, the ion non-thermal component can be the main driver of neutrino production, while Figure 4.8 suggests that electron heating is nevertheless an unavoidable by-product at the tens-of-

percent level in the downstream energy budget. We emphasize that our results are based on the parameter ranges and timescales accessible to the simulations shown here, and that translating these fractions to specific AGN or corona conditions requires additional modeling (including geometry, escape, and radiative losses). However, within our survey, the thermal electron energy fraction appears to be a robust outcome of shock dissipation, and therefore a natural ingredient to include when connecting ion-acceleration-motivated shock models to electromagnetic observables.

Chapter 5

Implications for neutrino emission from NGC 1068

5.1 Introduction

Here, we explore the implications of our results for neutrino emission from NGC 1068—the most prominent detection from the IceCube observatory to date (IceCube Collaboration*† et al., 2022). The detection is constrained in the neutrino energy range $E_\nu = 1.5$–15 TeV, which implies the presence of protons with energies $E_p \approx 30$–300 TeV. To reach such energies, the proton acceleration timescale must be shorter than the timescales associated with energy losses from cooling and neutrino production. We therefore begin by comparing these relevant timescales. Then, we examine whether the proton acceleration efficiency inferred from our simulations (Section 3.6) can fulfill the energy budget implied by the neutrino spectrum of the source.

In the following analysis, we adopt a set of coronal parameters for NGC 1068 listed in Padovani et al. (2024), which we use consistently throughout this chapter unless stated otherwise. We assume a black hole mass of $M_{\rm BH} = 10^{7.2}\,M_\odot$ and a characteristic coronal size of $R_c = 20\,R_g$. The coronal photon field consists of a multi-temperature blackbody emission from the accretion disk (Shakura & Sunyaev, 1973), parameterized as $L_{\rm disk} \propto E^{4/3}\exp(-E/E_{\rm cut})$ with $E_{\rm cut} = 30$ eV, together with a Comptonized X-ray component described by $L_X \propto E^{1-\Gamma_X}\exp(-E/E_{\rm cut,X})$, where $E_{\rm cut,X} = 128$ keV and $\Gamma_X = 1.95$. Assuming a luminosity distance of $d_L = 10$ Mpc, this corresponds to an integrated disk luminosity of $L_{\rm disk} = 5\times10^{44}$ erg s^{-1} and a 2–10 keV X-ray luminosity of $L_{2-10\,\rm keV} = 4\times10^{43}$ erg s^{-1}.

5.2 Timescales

All the relevant timescales are summarized in Figure 5.1 as a function of proton energy.

In the scenario shown in Figure 3.1 discussed in Section 3.2, the dynamical timescale

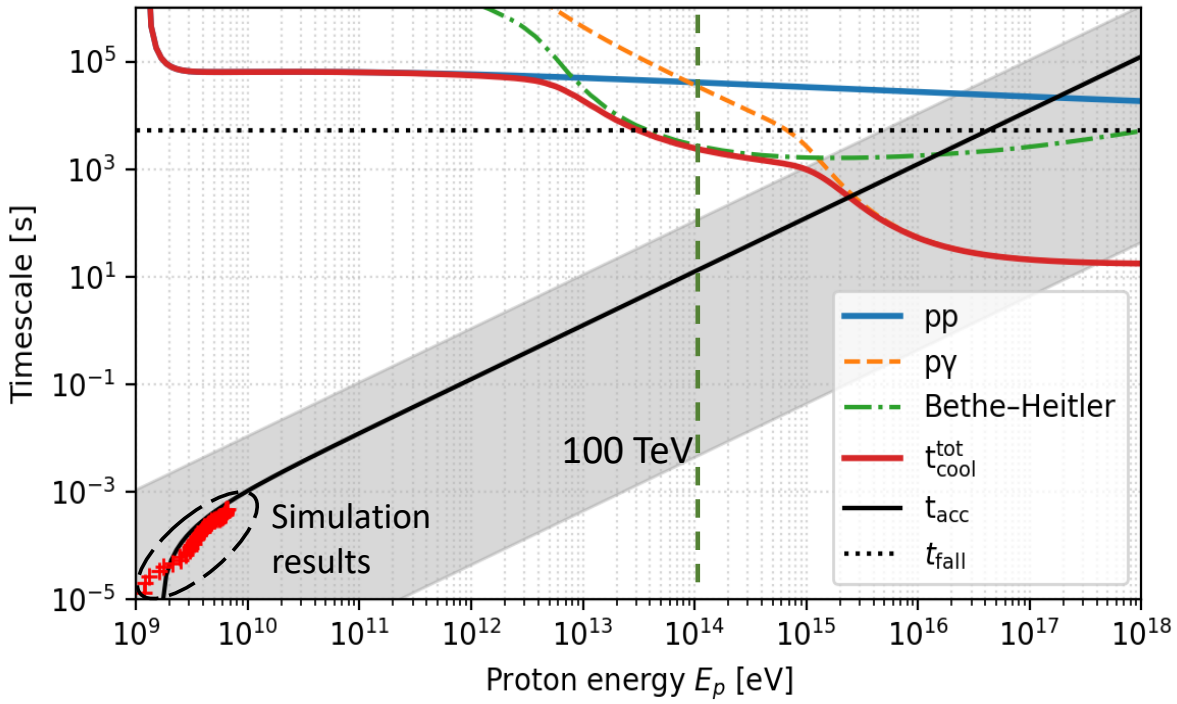

Figure 5.1: Various timescales in the BH corona of NGC 1068 as a function of proton energy. The typical acceleration timescale $t_{\rm acc}$ (solid black line) is calculated using Equation (5.6) with $B_0 = 100$ G and $\beta_{\rm sh} = 0.32$. The free-fall timescale $t_{\rm fall}$ (dotted black line) is calculated using Equation (5.1). The simulation results taken from run T10 give the normalization of $t_{\rm acc}$. The gray shaded region indicates the range of $t_{\rm acc}$ when varying $B_0 = 10$–1000 G and $\beta_{\rm sh} = 0.1$–0.5. The cooling timescales for pp interactions t_{pp} (blue line), $p\gamma$ interactions $t_{p\gamma}$ (orange dashed line), and Bethe–Heitler pair production $t_{\rm BH}$ (green dash-dotted line) are calculated following the methods in Inoue et al. (2019). The total cooling timescale $t_{\rm cool}$ (red line) is obtained by combining all cooling processes. The vertical green dashed line marks $E_p = 100$ TeV, representative of the proton energy required to produce TeV neutrinos.

is determined by the free-fall time,

$$t_{\rm fall} = \frac{R_c}{v_{\rm ff}} \simeq 0.52 \times 10^4 \left(\frac{r_c}{20}\right)^{3/2} \left(\frac{M_{\rm BH}/M_\odot}{10^{7.2}}\right) \ [\rm s] \ . \tag{5.1}$$

To account for the observed neutrino emission, protons must be accelerated to energies of $E_p \sim 100$ TeV. At these energies, in addition to hadronic pion production via pp and $p\gamma$ interactions, protons also experience energy losses through Bethe–Heitler pair production. We calculate these cooling timescales by considering the interaction of relativistic protons with the coronal matter density and the coronal photon fields.

The cooling rate for inelastic proton–proton (pp) collisions is determined by the coronal proton density n_p. Assuming the plasma is composed of protons and electrons ($n_p \approx n_e$) and the density is uniform, we estimate n_p from the Thomson scattering opacity τ_T as $n_p \simeq \tau_T/(\sigma_T R_c)$.. The pp cooling timescale is then given by

$$t_{pp}^{-1} = n_p \, c \, \sigma_{pp} \, \kappa_{pp} \ , \tag{5.2}$$

where $\kappa_{pp} \approx 0.5$ is the inelasticity of the interaction. We adopt the parameterization for the total inelastic pp cross section, $\sigma_{pp}(E_p)$, from Kelner et al. (2006):

$$\sigma_{pp}(E_p) \simeq \left(34.3 + 1.88L + 0.25L^2\right) \left[1 - \left(\frac{E_{th}}{E_p}\right)^4\right]^2 \ \rm mb \ , \tag{5.3}$$

where $L = \ln(E_p/1\,\rm TeV)$ and the threshold energy is $E_{th} = 1.22\,\rm GeV$. As shown in Figure 5.1 (solid blue line), pp interactions provide a nearly energy-independent cooling floor, which dominates at lower proton energies ($E_p \lesssim 10\,\rm TeV$) where the photohadronic cross sections are suppressed by kinematic thresholds.

For photohadronic interactions, the target photon field $U_{ph}(\epsilon)$ is constructed from the two spectral components described in the Introduction: the multi-temperature blackbody emission from the accretion disk ($L_{\rm disk}$) and the Comptonized coronal X-ray emission (L_X). Assuming a uniform photon distribution inside the corona, the differential photon energy density is $U_{ph}(\epsilon) = [L_{\rm disk}(\epsilon) + L_X(\epsilon)]/(4\pi R_c^2 c)$. Given the compact source size ($R_c = 20\,R_g$) and high luminosity of NGC 1068, the total photon energy density is extremely high, $U_{ph} \sim 10^5\,\rm erg\,cm^{-3}$, making photohadronic cooling highly efficient.

The cooling rate via photomeson production ($p\gamma$) is calculated by integrating over the photon field following the formalism of Kelner & Aharonian (2008):

$$t_{p\gamma}^{-1} = \frac{c}{2\gamma_p^2} \int_{\bar\epsilon_{th}}^{\infty} d\bar\epsilon \, \sigma_{p\gamma}(\bar\epsilon) \, K_{p\gamma}(\bar\epsilon) \, \bar\epsilon \int_{\bar\epsilon/2\gamma_p}^{\infty} d\epsilon \, \frac{U_{ph}(\epsilon)}{\epsilon^2} \ , \tag{5.4}$$

where $\gamma_p = E_p/m_p c^2$ is the proton Lorentz factor, ϵ is the photon energy in the laboratory

frame, and $\bar{\epsilon}$ is the photon energy in the proton rest frame. The threshold for pion production is $\bar{\epsilon}_{th} \approx 145\,\mathrm{MeV}$. The interaction is governed by the product of the cross section $\sigma_{p\gamma}$ and the inelasticity $K_{p\gamma}$. As seen in Figure 5.1 (orange dashed line), $p\gamma$ cooling drops rapidly above $E_p \sim 100\,\mathrm{TeV}$ because protons of these energies can interact with the abundant UV disk photons near the peak of the SED.

Finally, we consider the cooling due to Bethe–Heitler (BH) pair production ($p + \gamma \to p + e^+ + e^-$). Although the inelasticity of this process is low ($K_{\mathrm{BH}} \sim 10^{-3}$), the cross section is large, and the energy threshold is lower ($\bar{\epsilon}_{th} \sim 1\,\mathrm{MeV}$) compared to photomeson production. We estimate the BH cooling timescale using the analytic approximation derived by Gao et al. (2012):

$$t_{\mathrm{BH}}^{-1} \approx \frac{7(m_e c^2)^3 \alpha_{\mathrm{f}} \sigma_T c}{9\sqrt{2}\pi m_p c^2 \gamma_p^2} \int_{m_e c^2/\gamma_p}^{\infty} d\epsilon \, \frac{U_{ph}(\epsilon)}{\epsilon^2} \left\{ \left(\frac{2\gamma_p \epsilon}{m_e c^2} \right)^{3/2} \left[\ln\left(\frac{2\gamma_p \epsilon}{m_e c^2} \right) - \frac{2}{3} \right] + \frac{2}{3} \right\} , \tag{5.5}$$

where α_{f} is the fine-structure constant. The resulting timescale is shown in Figure 5.1 (green dash-dotted line). Notably, for the specific radiation field of NGC 1068, Bethe–Heitler cooling becomes the dominant energy loss channel in the intermediate energy range ($E_p \approx 10$–$100\,\mathrm{TeV}$), bridging the gap between the pp-dominated and $p\gamma$-dominated regimes.

For the proton acceleration timescale t_{acc}, we make use of our result obtained in Section 3.5. In particular, we adopt the scaling of Equation (3.7) with the typical value of $\mathcal{C}^{-1} = d(\gamma\beta_{\mathrm{sh}}^{-2})/d(t\Omega_{\mathrm{ci}}) \simeq 0.1$. The resulting scaling for the proton acceleration timescale reads

$$\begin{aligned} t_{\mathrm{acc}} &\simeq \mathcal{C}\,\gamma\,\beta_{\mathrm{sh}}^{-2}\,\Omega_{\mathrm{ci}}^{-1} \\ &\simeq 11.1 \left(\frac{E_p}{100\ \mathrm{TeV}} \right) \left(\frac{\mathcal{C}^{-1}}{0.1} \right)^{-1} \left(\frac{\beta_{\mathrm{sh}}}{0.32} \right)^{-2} \left(\frac{B_0}{100\ \mathrm{G}} \right)^{-1} \ [\mathrm{s}] \, . \end{aligned} \tag{5.6}$$

In Figure 5.1, we extrapolate the simulation scaling given by Equation (5.6) over several orders of magnitude, assuming the same late-time trend continues.

In addition to the balance between acceleration and cooling, the maximum proton energy is constrained by the finite size of the BH corona. This geometrical constraint, $\rho_i \lesssim R_c$, is known as the Hillas limit (Hillas, 1984) and implies a maximum achievable energy $E_{\mathrm{max}} \lesssim eB_0R_c$. In the context of DSA, a tighter constraint is often applied, taking the form $E_{\mathrm{max}} \lesssim eB_0R_c\beta_{\mathrm{sh}}$ (Drury, 2012; Oka et al., 2025), which yields the scaling

$$E_{p,\mathrm{max}} \lesssim 467 \left(\frac{B_0}{100\ \mathrm{G}} \right) \left(\frac{r_c}{20} \right) \left(\frac{M_{\mathrm{BH}}/M_\odot}{10^{7.2}} \right) \left(\frac{\beta_{\mathrm{sh}}}{0.32} \right) \ [\mathrm{PeV}] \, . \tag{5.7}$$

Equation (5.7) shows that the Hillas criterion allows proton acceleration to ~ 100 TeV provided that $B_0 \gtrsim 10$ G and $\beta_{\mathrm{sh}} \gtrsim 10^{-2}$. Moreover, as shown in Figure 5.1, the accel-

eration timescale $t_{\rm acc}$ remains shorter than the total cooling timescale $t_{\rm cool}$ up to proton energies of $E_p \sim 1\,\mathrm{PeV}$ for the same range of parameters. Hence, these results demonstrate that our DSA framework can robustly supply the high-energy protons responsible for the neutrinos in the energy range observed by IceCube.

5.3 Energy budget

Finally, we discuss whether the acceleration efficiency derived from our simulations ($E_p^{\rm nt}/E_{\rm tot} \approx 10\%$) is sufficient to produce the observed neutrino flux. In the scenario of a spherical shock with $R_{\rm sh} \simeq R_c$ as we assume here, the shock power can be estimated as

$$\begin{aligned} L_{\rm sh} &= \frac{1}{2} n_i m_i v_{\rm sh}^3 (4\pi R_{\rm sh}^2) \\ &\simeq 7.3 \times 10^{44} \left(\frac{r_c}{20}\right) \left(\frac{M_{\rm BH}/M_\odot}{10^{7.2}}\right) \left(\frac{v_{\rm sh}/c}{0.32}\right)^3 \ [\mathrm{erg/s}] \ , \end{aligned} \tag{5.8}$$

where we assume $n_i \simeq n_e \simeq (\sigma_T R_c)^{-1}$.

According to the latest IceCube report (Abbasi et al., 2025), the best-fit flux at 1 TeV is $\Phi_\nu = 4.7^{+1.1}_{-1.3} \times 10^{-11}$ TeV^{-1} cm^{-2} s^{-1}, corresponding to a neutrino luminosity $L_\nu \approx 4\pi d_L^2 E_\nu^2 \Phi_\nu \simeq 9 \times 10^{41} \times [d_L/(10\ \mathrm{Mpc})]^2$ erg/s. The non-thermal proton luminosity required to produce such a neutrino luminosity can be estimated as

$$L_p^{\rm nt} \approx \frac{\mathcal{S} L_\nu}{f_\nu} \ , \tag{5.9}$$

where f_ν is the per-flavor production fraction, and $\mathcal{S} \geq 1$ is a spectral-shape factor that accounts for the continuous nature of the non-thermal proton spectrum. Neutrinos with $E_\nu = 1$ TeV are mainly produced by protons with energy $E_p \sim 20 E_\nu \sim 20$ TeV through pp interactions (Figure 5.1). Hence, we adopt $f_\nu \sim 1/6$ and $\mathcal{S} \gtrsim 4$ for a proton spectrum with power-law index $s_p = 2$, as seen in most of our simulations. The required non-thermal proton luminosity is therefore $L_p^{\rm nt} \approx 2.2 \times 10^{43}$ erg s^{-1}, corresponding to a fractional power $L_p^{\rm nt}/L_{\rm sh} \approx 0.03$, well below the proton acceleration efficiency inferred from our simulations (e.g., $E_p^{\rm nt}/E_{\rm sh} \sim 0.1$). Consequently, collisionless shocks can readily supply sufficient power to account for the neutrino luminosity observed from NGC 1068.

Finally, we stress that this estimate is intended to put our results into perspective and provide an intuitive picture of neutrino production in NGC 1068. Applying results from local, first-principles kinetic simulations to a complex astrophysical object such as an AGN corona requires careful consideration. In this work, we have self-consistently determined the physical conditions at the localized shock front from first principles. The estimate presented here should be regarded as an order-of-magnitude assessment based on the microphysics established in this thesis. Nonetheless, it offers a useful bridge between

microscopic plasma physics and the macroscopic high-energy phenomena observed by IceCube.

Chapter 6

Conclusion

6.1 Summary of the Thesis

The recent identification of the Seyfert galaxy NGC 1068 as a source of high-energy neutrinos by the IceCube Neutrino Observatory presents a major challenge to standard high-energy astrophysical models. The detected neutrino flux, unaccompanied by a comparable flux of TeV gamma-rays, points to a particle acceleration environment that is transparent to neutrinos but opaque to gamma-rays: likely the hot coronal region surrounding the supermassive black hole.

The primary objective of this thesis was to investigate the microphysics of DSA in BH coronae through a comprehensive suite of first-principles, one-dimensional PIC simulations. To build a rigorous foundation for this complex environment, we first established a kinetic baseline in the unmagnetized electrostatic limit. By updating the conventional collisionless shock model to account for density expansion, we mapped the critical density ratio threshold ($\Gamma \approx 40$) where shocks transition into electrostatic double-layer structures.

Building upon this fundamental framework of potential structures and ion dynamics, we extended our analysis to the magnetized regime to resolve critical uncertainties regarding the viability of DSA in BH coronae. Specifically, we focused on environments characterized by low sonic Mach numbers (M_s) and non-equilibrium temperatures ($T_i \neq T_e$).

Our results demonstrate a fundamental property in the acceleration efficiency of hadronic and leptonic species. We found that quasi-parallel collisionless shocks are robust proton accelerators, whereas electron acceleration is highly sensitive to the upstream parameters and is often suppressed by self-generated magnetic turbulence.

6.1.1 On collisionless electrostatic shocks

Before introducing magnetic field, this thesis established a kinetic baseline by investigating the fundamental dynamics of collisionless electrostatic shocks. Using 1D PIC simulations of two interacting plasma slabs, we examined the shock structure that emerges at the interface of varying pressure gradients to understand baseline potential structures and ion dynamics.

A key discovery of this analysis is the structural transition from a conventional collisionless shock to an electrostatic double-layer at high density gradients. We identified that this structural transformation occurs at a critical initial density ratio of $\Gamma \approx 40$, a threshold that remains robust regardless of the initial temperature ratio between the plasmas.

To address inconsistencies in existing theoretical frameworks, where observed shock speeds sometimes exceeded theoretical limits, we developed an updated collisionless shock model. By incorporating the density expansion effects caused by a rarefaction wave and introducing a semi-analytical approach based on the accelerated particle fraction (α), our new model significantly improves the prediction of critical Mach numbers and the shock velocity. This purely electrostatic framework defines the baseline dissipation mechanisms, setting the stage for the subsequent analysis of magnetized coronal environments.

6.1.2 Proton acceleration

A central finding of this work is the resilience of proton acceleration via the DSA mechanism. We demonstrated that quasi-parallel collisionless shocks consistently convert approximately 10% of the shock wave's kinetic energy into non-thermal ions. This efficiency holds true even in the low-Mach-number regime ($M_s \approx 2$), which was traditionally considered inefficient for particle acceleration.

Furthermore, we verified that the acceleration rates are sufficient to reach the requisite ~ 100 TeV energies, providing the necessary reservoir for hadronic neutrino production[cite: 18]. The normalized acceleration rate was found to be $\mathcal{C}^{-1} \simeq 0.1$, varying by less than a factor of two across all parameter sets. Our parameter survey indicates that this high ion acceleration efficiency is robust against variations in the ion-to-electron temperature ratio (T_i/T_e) and the Alfvénic Mach number (M_A).

In investigating the accompanying electron dynamics, we revealed a complex interplay between self-generated turbulence and particle injection. We characterized the self-generated magnetic turbulence driven by non-resonant (Bell) and resonant streaming instabilities.

Crucially, we linked strong magnetic amplification to the suppression of primary electron acceleration. We found that when the magnetic field amplification exceeds a critical threshold ($B_{sat} > B_{crit}$), the shock front becomes locally superluminal. This kinematic constraint traps thermal electrons in the downstream region, inhibiting their injection into the DSA cycle and causing the acceleration rate $\dot{E}_{max,e}$ to stall.

Additionally, we found that the thermodynamic state of the upstream plasma plays a significant role. A high ion-to-electron temperature ratio ($T_i/T_e \geq 10$), which is expected in coronal plasmas, leads to a monotonic decrease in electron acceleration efficiency. While non-thermal electron acceleration is often suppressed, our energy partition analysis

indicates that shocks consistently inject a significant fraction of energy ($\sim$ 30%) into thermal electron heating.

6.1.3 Multi-messenger implications for NGC 1068

The microphysical constraints derived in this thesis offer a coherent physical picture for the multi-messenger signals from NGC 1068. We compared the acceleration timescales with relevant cooling timescales (proton-proton, photomeson, and Bethe-Heitler interactions) and found that the acceleration timescale t_{acc} remains shorter than the total cooling timescale up to proton energies of $E_p \sim 1$ PeV.

Regarding the energy budget, we estimated the non-thermal proton luminosity required to produce the observed neutrino flux. The required fractional power is $L_p^{nt}/L_{sh} \approx 0.03$, which is well below the proton acceleration efficiency ($E_p^{nt}/E_{tot} \sim 0.1$) inferred from our simulations. Consequently, collisionless shocks in the corona can readily supply sufficient power to account for the neutrino luminosity observed from NGC 1068. The concomitant suppression of electron acceleration supports scenarios where the radiative output is dominated by thermal Comptonization rather than non-thermal leptonic emission.

6.2 Limitations and Future Work

While this thesis establishes a firm foundation for shock acceleration in coronal environments, we acknowledge the following limitations for improvement in future works.

Our use of 1D simulations limits the analysis of cross-field diffusion and particle drift in the transverse direction. While 1D geometries accurately capture the parallel diffusion essential for DSA in quasi-parallel shocks, multi-dimensional effects could modify the injection thresholds for electrons. Future 2D or 3D studies are necessary to fully characterize the impact of transverse magnetic fluctuations on the critical superluminal transition discussed in Chapter 3.

In conclusion, this thesis demonstrates that collisionless shocks are not only viable but are energetically capable of powering the high-energy neutrino emission observed from NGC 1068. By providing first-principles constraints on the efficiency of these shocks, we bridge the gap between microscopic plasma kinetics and macroscopic astrophysical phenomenology.

Bibliography

Abbasi, R., Ackermann, M., Adams, J., et al. 2025, Evidence for Neutrino Emission from X-ray Bright Active Galactic Nuclei with IceCube, arXiv, doi: 10.48550/arXiv.2510.13403

Allen, J. E., & Andrews, J. G. 1970, Journal of Plasma Physics, 4, 187, doi: 10.1017/S0022377800004906

Balogh, A., & Treumann, R. A. 2013a, Physics of Collisionless Shocks (New York, NY: Springer New York), doi: 10.1007/978-1-4614-6099-2

—. 2013b, Physics of Collisionless Shocks: Space Plasma Shock Waves (New York: Springer), doi: 10.1007/978-1-4614-6099-2

Bambi, C., Brenneman, L. W., Dauser, T., et al. 2021, , 217, 65, doi: 10.1007/s11214-021-00841-8

Bell, A. R. 2004, Monthly Notices of the Royal Astronomical Society, 353, 550, doi: 10.1111/j.1365-2966.2004.08097.x

Blandford, R., & Eichler, D. 1987a, Physics Reports, 154, 1, doi: 10.1016/0370-1573(87)90134-7

—. 1987b, Physics Reports, 154, 1, doi: 10.1016/0370-1573(87)90134-7

Blasi, P. 2013, The Astronomy and Astrophysics Review, 21, 70, doi: 10.1007/s00159-013-0070-7

Caprioli, D., & Spitkovsky, A. 2014a, The Astrophysical Journal, 794, 46, doi: 10.1088/0004-637X/794/1/46

—. 2014b, The Astrophysical Journal, 783, 91, doi: 10.1088/0004-637X/783/2/91

Das, A., Zhang, B. T., & Murase, K. 2024, The Astrophysical Journal, 972, 44, doi: 10.3847/1538-4357/ad5a04

De Hoffmann, F., & Teller, E. 1950, Phys. Rev., 80, 692, doi: 10.1103/PhysRev.80.692

del Palacio, S., Yang, C., Aalto, S., et al. 2025, Astronomy & Astrophysics, 701, A41, doi: 10.1051/0004-6361/202554936

Derouillat, J., Beck, A., Pérez, F., et al. 2018, Computer Physics Communications, 222, 351, doi: 10.1016/j.cpc.2017.09.024

Dieckmann, M. E., Ahmed, H., Sarri, G., et al. 2013a, Physics of Plasmas, 20, 042111, doi: 10.1063/1.4801447

Dieckmann, M. E., Sarri, G., Doria, D., Pohl, M., & Borghesi, M. 2013b, Physics of Plasmas, 20, 102112, doi: 10.1063/1.4825339

Drake, R. P. 2018, High-Energy-Density Physics (Cham: Springer International Publishing), doi: 10.1007/978-3-319-67711-8

Drury, L. O. 1983, Reports on Progress in Physics, 46, 973, doi: 10.1088/0034-4885/46/8/002

—. 2012, Astroparticle Physics, 39–40, 52, doi: 10.1016/j.astropartphys.2012.02.006

Ergun, R. E., Andersson, L., Tao, J., et al. 2009, Physical Review Letters, 102, 155002, doi: 10.1103/PhysRevLett.102.155002

Fabian, A. C., Lohfink, A., Kara, E., et al. 2015, Monthly Notices of the Royal Astronomical Society, 451, 4375, doi: 10.1093/mnras/stv1218

Fiorillo, D. F. G., Comisso, L., Peretti, E., Petropoulou, M., & Sironi, L. 2024a, The Astrophysical Journal, 974, 75, doi: 10.3847/1538-4357/ad7021

Fiorillo, D. F. G., Petropoulou, M., Comisso, L., Peretti, E., & Sironi, L. 2024b, The Astrophysical Journal Letters, 961, L14, doi: 10.3847/2041-8213/ad192b

Fiuza, F., Stockem, A., Boella, E., et al. 2012, Physical Review Letters, 109, 215001, doi: 10.1103/PhysRevLett.109.215001

—. 2013, Physics of Plasmas, 20, 056304, doi: 10.1063/1.4801526

Forslund, D. W., & Shonk, C. R. 1970, Phys. Rev. Lett., 25, 1699

Gao, S., Asano, K., & Mészáros, P. 2012, Journal of Cosmology and Astroparticle Physics, 2012, 058, doi: 10.1088/1475-7516/2012/11/058

Goertz, C. K. 1979, Reviews of Geophysics, 17, 418, doi: 10.1029/RG017i003p00418

Gupta, S., Caprioli, D., & Spitkovsky, A. 2024a, The Astrophysical Journal, 968, 17, doi: 10.3847/1538-4357/ad3e75

—. 2024b, The Astrophysical Journal, 976, 10, doi: 10.3847/1538-4357/ad7c4c

—. 2025, Speed-Dependent Threshold for Electron Injection into Diffusive Shock Acceleration, arXiv, doi: 10.48550/arXiv.2506.09134

Haberberger, D., Tochitsky, S., Fiuza, F., et al. 2012, Nature Physics, 8, 95, doi: 10.1038/nphys2130

Haggerty, C. C., & Caprioli, D. 2019, The Astrophysical Journal, 887, 165, doi: 10.3847/1538-4357/ab58c8

Hankla, A., Philippov, A., Mbarek, R., et al. 2025, arXiv e-prints, arXiv:2512.01662, doi: 10.48550/arXiv.2512.01662

Hershkowitz, N. 1981, Journal of Geophysical Research, 86, 3307, doi: 10.1029/ja086ia05p03307

Hershkowitz, N., Payne, G. L., Chan, C., & Dekock, J. R. 1981, Plasma Physics, 23, 903, doi: 10.1088/0032-1028/23/10/003

Hillas, A. M. 1984, Annual Review of Astronomy and Astrophysics, 22, 425, doi: 10.1146/annurev.aa.22.090184.002233

Huntington, C. M., Fiuza, F., Ross, J. S., et al. 2015, Nature Physics, 11, 173, doi: 10.1038/nphys3178

IceCube Collaboration*†, Abbasi, R., Ackermann, M., et al. 2022, Science, 378, 538, doi: 10.1126/science.abg3395

Inoue, S., Cerruti, M., Murase, K., & Liu, R.-Y. 2024a, High-Energy Neutrinos and Gamma Rays from Winds and Tori in Active Galactic Nuclei, arXiv, doi: 10.48550/arXiv.2207.02097

Inoue, Y., & Doi, A. 2018, The Astrophysical Journal, 869, 114, doi: 10.3847/1538-4357/aaeb95

Inoue, Y., Khangulyan, D., & Doi, A. 2020, The Astrophysical Journal, 891, L33, doi: 10.3847/2041-8213/ab7661

Inoue, Y., Khangulyan, D., Inoue, S., & Doi, A. 2019, The Astrophysical Journal, 880, 40, doi: 10.3847/1538-4357/ab2715

Inoue, Y., Takasao, S., & Khangulyan, D. 2024b, Upper Limit on the Coronal Cosmic Ray Energy Budget in Seyfert Galaxies, arXiv, doi: 10.48550/arXiv.2401.07580

Jana, A., Ricci, C., Venselaar, S. M., et al. 2025, , 699, A62, doi: 10.1051/0004-6361/202554491

Jikei, T., Groselj, D., & Sironi, L. 2025, Magnetic Field Amplification and Particle Acceleration in Weakly Magnetized Trans-relativistic Electron-ion Shocks, arXiv, doi: 10.48550/arXiv.2512.03169

Johlander, A., Battarbee, M., Vaivads, A., et al. 2021, The Astrophysical Journal, 914, 82, doi: 10.3847/1538-4357/abfafc

Karavola, D., Petropoulou, M., Fiorillo, D. F. G., Comisso, L., & Sironi, L. 2025, Neutrino and Pair Creation in Reconnection-Powered Coronae of Accreting Black Holes, arXiv, doi: 10.48550/arXiv.2410.12638

Kato, T. N. 2015, The Astrophysical Journal, 802, 115, doi: 10.1088/0004-637X/802/2/115

Kelner, S. R., & Aharonian, F. A. 2008, Physical Review D, 78, 034013, doi: 10.1103/PhysRevD.78.034013

Kelner, S. R., Aharonian, F. A., & Bugayov, V. V. 2006, Physical Review D, 74, 034018, doi: 10.1103/PhysRevD.74.034018

Kheirandish, A., Murase, K., & Kimura, S. S. 2021, The Astrophysical Journal, 922, 45, doi: 10.3847/1538-4357/ac1c77

Koyama, K., Petre, R., Gotthelf, E. V., et al. 1995, Nature, 378, 255, doi: 10.1038/378255a0

Laha, S., Ricci, C., Mather, J. C., et al. 2025, Frontiers in Astronomy and Space Sciences, 11, 1530392, doi: 10.3389/fspas.2024.1530392

Landau, L., & Lifshitz, E. 1959, Fluid Mechanics (Elsevier), doi: 10.1016/C2013-0-03650-X

Li, T. C., Drake, J. F., & Swisdak, M. 2012, The Astrophysical Journal, 757, 20, doi: 10.1088/0004-637X/757/1/20

Ly, M. N., Sano, T., Sakawa, Y., & Sentoku, Y. 2023, Physical Review E, 108, 025208, doi: 10.1103/PhysRevE.108.025208

Mach, E., & Salcher, P. 1887, II Abth, 95, 764

Malkov, M. A., Sagdeev, R. Z., Dudnikova, G. I., et al. 2016, Physics of Plasmas, 23, 043105, doi: 10.1063/1.4945649

Marcowith, A., Van Marle, A. J., & Plotnikov, I. 2021, Physics of Plasmas, 28, 080601, doi: 10.1063/5.0013662

Marcowith, A., Bret, A., Bykov, A., et al. 2016, Reports on Progress in Physics, 79, 046901, doi: 10.1088/0034-4885/79/4/046901

Marret, A., Ciardi, A., Smets, R., & Fuchs, J. 2021, Monthly Notices of the Royal Astronomical Society, 500, 2302, doi: 10.1093/mnras/staa3465

Marshall, W. 1955, Proc. R. Soc. Lond., 233, 367

Mbarek, R., Philippov, A., Chernoglazov, A., Levinson, A., & Mushotzky, R. 2023. https://arxiv.org/abs/2310.15222

Michiyama, T., Inoue, Y., & Doi, A. 2023, Publications of the Astronomical Society of Japan, 75, 874, doi: 10.1093/pasj/psad044

Michiyama, T., Inoue, Y., Doi, A., et al. 2024, , 965, 68, doi: 10.3847/1538-4357/ad2fae

Moreno, Q., Dieckmann, M. E., Folini, D., et al. 2020, Plasma Physics and Controlled Fusion, 62, 025022, doi: 10.1088/1361-6587/ab5bfb

Müller, A. L., Naddaf, M.-H., Zajaček, M., et al. 2022, The Astrophysical Journal, 931, 39, doi: 10.3847/1538-4357/ac660a

Müller, A. L., & Romero, G. E. 2020, Astronomy & Astrophysics, 636, A92, doi: 10.1051/0004-6361/202037639

Murase, K. 2022, The Astrophysical Journal Letters, 941, L17, doi: 10.3847/2041-8213/aca53c

Murase, K., Kimura, S. S., & Mészáros, P. 2020, Physical Review Letters, 125, 011101, doi: 10.1103/PhysRevLett.125.011101

Mutie, I. M., Del Palacio, S., Beswick, R. J., et al. 2025, Monthly Notices of the Royal Astronomical Society, 539, 808, doi: 10.1093/mnras/staf524

Ness, N. F., Scearce, C., & Seek, J. B. 1964, Journal of Geophysical Research, 69, 3531

Oka, M., Makishima, K., & Terasawa, T. 2025, The Astrophysical Journal, 979, 161, doi: 10.3847/1538-4357/ad9916

Oka, M., Wilson III, L. B., Phan, T. D., et al. 2017, The Astrophysical Journal, 842, L11, doi: 10.3847/2041-8213/aa7759

P Crumley, Caprioli, D., Markoff, S., & Spitkovsky, A. 2019, Monthly Notices of the Royal Astronomical Society, 485, 5105, doi: 10.1093/mnras/stz232

Padovani, P., Resconi, E., Ajello, M., et al. 2024, High-Energy Neutrinos from the Vicinity of the Supermassive Black Hole in NGC 1068, arXiv. https://arxiv.org/abs/2405.20146

Park, J., Caprioli, D., & Spitkovsky, A. 2015, Physical Review Letters, 114, 085003, doi: 10.1103/PhysRevLett.114.085003

Park, J., Workman, J. C., Blackman, E. G., Ren, C., & Siller, R. 2012, Physics of Plasmas, 19, 062904, doi: 10.1063/1.4729913

Perego, M., Howell, P. D., Gunzburger, M. D., Ockendon, J. R., & Allen, J. E. 2013, Physics of Plasmas, 20, 052101, doi: 10.1063/1.4802933

Perri, S., Bykov, A., Fahr, H., Fichtner, H., & Giacalone, J. 2022, Space Science Reviews, 218, 26, doi: 10.1007/s11214-022-00892-5

Reville, B., Kirk, J. G., Duffy, P., & O'Sullivan, S. 2008, International Journal of Modern Physics D, 17, 1795, doi: 10.1142/S021827180801342X

Riquelme, M. A., & Spitkovsky, A. 2009, The Astrophysical Journal, 694, 626, doi: 10.1088/0004-637X/694/1/626

Russell, B. K., Campbell, P. T., Thomas, A. G. R., & Willingale, L. 2021, Plasma Physics and Controlled Fusion, 63, 095012, doi: 10.1088/1361-6587/ac1569

Sagdeev, R. Z. 1966, Reviews of Plasma Physics, 4, 23

Sakawa, Y., Ohira, Y., Kumar, R., et al. 2021, Physical Review E, 104, 055202, doi: 10.1103/PhysRevE.104.055202

Sarri, G., Dieckmann, M. E., Kourakis, I., & Borghesi, M. 2011a, Physical Review Letters, 107, 025003, doi: 10.1103/PhysRevLett.107.025003

Sarri, G., Murphy, G. C., Dieckmann, M. E., et al. 2011b, New Journal of Physics, 13, 073023, doi: 10.1088/1367-2630/13/7/073023

Sentoku, Y., & Kemp, A. J. 2008, Journal of Computational Physics, 227, 6846, doi: 10.1016/j.jcp.2008.03.043

Shablovinskaya, E., Ricci, C., Chang, C.-S., et al. 2024, Astronomy & Astrophysics, 690, A232, doi: 10.1051/0004-6361/202450133

Shakura, N. I., & Sunyaev, R. A. 1973, Astronomy and Astrophysics, 24, 337

Shalaby, M. 2024, The Astrophysical Journal Letters, 977, L43, doi: 10.3847/2041-8213/ad99d8

Skilling, J. 1971, The Astrophysical Journal, 170, 265, doi: 10.1086/151210

Sonett, C. P., & Abrams, I. J. 1963, J. Geophys. Res., 68, 1233

Sorasio, G., Marti, M., Fonseca, R., & Silva, L. O. 2006, Physical Review Letters, 96, 045005, doi: 10.1103/PhysRevLett.96.045005

Sotomayor, P., & Romero, G. E. 2022, Astronomy & Astrophysics, 664, A178, doi: 10.1051/0004-6361/202243682

Spitkovsky, A. 2008, The Astrophysical Journal, 682, L5, doi: 10.1086/590248

Stockem, A., Boella, E., Fiuza, F., & Silva, L. O. 2013, Physical Review E, 87, 043116, doi: 10.1103/PhysRevE.87.043116

Stockem Novo, A., Bret, A., Fonseca, R. A., & Silva, L. O. 2016, Plasma Physics and Controlled Fusion, 58, 014005, doi: 10.1088/0741-3335/58/1/014005

Sun, J., Vasko, I. Y., Bale, S. D., Wang, R., & Mozer, F. S. 2022, Geophysical Research Letters, 49, e2022GL101348, doi: 10.1029/2022GL101348

Tidman, D. A., & Krall, N. A. 1971, Shock Waves in Collisionless Plasmas (Wiley-Interscience)

Vink, J., & Yamazaki, R. 2014, The Astrophysical Journal, 780, 125, doi: 10.1088/0004-637X/780/2/125

Yuan, F., & Narayan, R. 2014, Annual Review of Astronomy and Astrophysics, 52, 529, doi: 10.1146/annurev-astro-082812-141003

Zacharegkas, G., Caprioli, D., Haggerty, C., Gupta, S., & Schroer, B. 2024, The Astrophysical Journal, 967, 71, doi: 10.3847/1538-4357/ad3960

Zeković, V., Spitkovsky, A., & Hemler, Z. 2025, The Astrophysical Journal, 988, 40, doi: 10.3847/1538-4357/ade05f

Zel'dovich, Y. B., & Raizer, Y. P. 2002, Physics of shock waves, Dover Books on Physics (Mineola, NY: Dover Publications)

Zweibel, E. G., & Everett, J. E. 2010, The Astrophysical Journal, 709, 1412, doi: 10.1088/0004-637X/709/2/1412